INSIGHTS ON THE REACTIVITY OF ENVIRONMENTAL IRON-CONTAINING NANOPARTICLES

A DISSERTATION

SUBMITTED TO THE FACULTY OF THE GRADUATE SCHOOL

OF THE UNIVERSITY OF MINNESOTA

BY

Jasmine Jade Erbs

IN PARTIAL FULFILLMENT OF THE REQUIREMENTS

FOR THE DEGREE OF

DOCTOR OF PHILOSOPHY

Dr. R. Lee Penn, Advisor
Dr. Subir K. Banerjee, Co-Advisor

May 2009

Acknowledgements

I would like to thank my colleagues, family, and friends for their support. This work would not be possible without the guidance and encouragement of my graduate research advisor, Dr. R. Lee Penn, and graduate research co-advisor, Dr. Subir K. Banerjee. I owe Lee many thanks for helping to cultivate my interests in research and teaching, and for the many opportunities to pursue those interests. I thank Subir for his interesting ideas and conversations about the magnetism of ferrihydrite materials. I thank the current and past Penn Group members for good discussions about research topics or otherwise. I also thank undergraduate students Djuna Gulliver, Kari Tanaka, and Jennifer Soltis for their work on the ferrihydrite-goethite growth projects.

My family has believed strongly in my success, which would not have been possible without their guidance and love. My pillar of strength has been my mom, Barbara, and I am grateful to have her as a wonderful friend and role model. And many thanks to my friends, Renee Cline, Elizabeth Lugert, Jacqueline Chivas, and Elaine Kellogg for the great memories and fun over the years.

This dissertation is dedicated to

my mom.

Abstract

Iron oxide minerals play an important role in natural processes including redox reactions and adsorption of trace species. Ferrihydrite ($Fe_5HO_8 \bullet 4H_2O$) is a metastable iron oxide that forms particles in the 3-10 nm size range and is believed to be a major player in the environment. The reactivity of ferrihydrite is influenced by the available surface area which is known to increase with decreasing particle size; however, size may also influence structural and/or thermodynamic properties. The size dependence of reductive dissolution was investigated for well-characterized ferrihydrite, with average lengths of 3.4 to 5.9 nm. Characterization and kinetics results revealed there was little or no dependence on size for nanoparticle structure, electronic structure, or redox reactivity of the ferrihydrite samples. In contrast, ferrihydrite nanoparticle size has a significant affect on the kinetics of growth by oriented aggregation to produce goethite nanorods, with rates increasing significantly with decreasing precursor size. First, we demonstrate that ferrihydrite nanoparticle size can be controlled by the hydrolysis temperature during nucleation from a homogeneous solution. Next, we show that the size of goethite nanocrystals formed by aging depends directly on the size of precursor ferrihydrite nanoparticles.

Inorganic arsenic species are carcinogenic and due to the affect on human health, high concentrations of arsenic in some groundwater systems have led to the study of arsenic's geochemical cycling. Arsenic has a high adsorption affinity for iron oxide and ferrihydrite materials and may influence the reactivity of such materials upon incorporation. The reductive dissolution kinetics of ferrihydrite prepared by coprecipitation with or adsorption of up to 10 wt% arsenate (AsO_4^{3-}) were quantified.

Arsenic adsorbed preferentially onto the most reactive surface sites substantially lowering the reductive dissolution rate. Coprecipitation led to structural defects, but the initial rate of reductive dissolution was similar to pure ferrihydrite.

Synthetic zero-valent iron (ZVI) materials have been studied for their application in remediation of contaminated sites with halogenated organic compounds that are resistant to degradation. Incorporation of up to 20 mol% copper into the ZVI materials increased the rates of carbon tetrachloride degradation but led to higher concentrations of chloroform during reaction. In addition, the solid-state products of ZVI oxidation varied substantially. In the end, copper is not an ideal ZVI additive because chloroform is not a preferred product. However, the use of metal additives is a promising method for the degradation of carbon tetrachloride if chloroform production can be minimized.

Table of Contents

Acknowledgements i

Dedication ii

Abstract iii

Table of Contents v

List of Tables ix

List of Figures xi

List of Abbreviations xv

Chapter 1 Introduction and Background 1

1.1 The Chemistry of Natural Systems 1

1.2 Iron Oxides 2

1.2.1 Ferrihydrite 3

1.2.2 Goethite 4

1.2.3 Magnetic Properties of Ferrihydrite and Goethite 5

1.3 Zero-Valent Iron 5

1.4 Scope of Dissertation 6

1.5 References 7

Chapter 2 Influence of Size on the Reductive Dissolution of Six-Line Ferrihydrite 11

2.1 Chapter Summary 11

2.2 Introduction 12

2.3 Experimental Methods 15

2.3.1 Synthesis of Materials 15

2.3.2 Materials Characterization 16
2.3.3 Kinetic Reactions 17
2.3.4 Analysis of Kinetic Data 20
2.4 Results and Discussion 21
2.4.1 Structural Analysis 21
2.4.2 Particle Size 23
2.4.3 Electronic Structure 24
2.4.4 Kinetic Reactions 26
2.5 Conclusions 34
2.6 Acknowledgments 34
2.7 References 35
Chapter 3 Kinetics of Goethite Nanocrystal Growth by Oriented Aggregation 40
3.1 Chapter Summary 40
3.2 Introduction 41
3.3 Experimental Methods 43
3.3.1 X-Ray Diffraction 44
3.3.2 Transmission Electron Microscopy 44
3.3.3 Particle Sizing and Particle Counting Methods 44
3.4 Results and Discussion 45
3.4.1 Size-Controlled Oriented Aggregation 45
3.4.2 Kinetics of Oriented Aggregation 51
3.5 Conclusions 59
3.6 Acknowledgments 59

3.7 References 60

Chapter 4 Reductive Dissolution of Arsenic-Bearing Ferrihydrite 65

4.1 Chapter Summary 65

4.2 Introduction 67

4.3 Experimental Methods 71

4.3.1 Synthesis of Materials 71

4.3.2 Materials Characterization 72

4.3.3 EXAFS 74

4.3.4 Magnetism 75

4.3.5 Potentiometric Titrations 76

4.3.6 Kinetic Reactions 77

4.4 Results and Discussion 79

4.4.1 Materials Characterization 79

4.4.2 EXAFS 83

4.4.3 Magnetism 85

4.4.4 Potentiometric Titrations 90

4.4.5 Kinetic Reaction 92

4.5 Conclusions 100

4.6 Acknowledgments 101

4.7 References 102

Chapter 5 Degradation of Carbon Tetrachloride by Zero-Valent Fe and Cu/Fe Particles 110

5.1 Chapter Summary 110

5.2 Introduction 111

5.3 Experimental Methods 114

5.3.1 Synthesis of Zero-Valent Iron Materials 114

5.3.2 Kinetic Reactions 116

5.3.3 Materials Characterization 118

5.4 Results and Discussion 119

5.4.1 Zero-Valent Iron Materials 119

5.4.2 Kinetic Reactions 123

5.4.3 Solid-State Products 126

5.5 Conclusions 133

5.6 Acknowledgments 133

5.7 References 134

Chapter 6 Conclusions 138

Bibliography 142

List of Tables

Table 2.1 Average particle length distributions (with standard deviations as error) and surface areas for ferrihydrite as determined using TEM 23

Table 2.2 Reaction orders of hydroquinone (*m*) and surface area (*n*) and average rate constants (*k*) of fresh and dried Fh 3.6 29

Table 2.3 Activation energies (E_a) and pre-exponential factors (*A*) results by Arrhenius analysis of fresh and dried ferrihydrite samples 33

Table 3.1 Summary of ferrihydrite and goethite particle size data 48

Table 3.2 Summary of ferrihydrite particle size data 51

Table 4.1 Elemental composition of ferrihydrite samples by ICP analysis. 79

Table 4.2 Average particle length and width distributions (with standard deviations as error) for ferrihydrite samples as determined using TEM and calculated specific surface areas. 82

Table 4.3 Fe k-edge EXAFS fitting results for As-ferrihydrite sorption and coprecipitated samples (see Figure 4.3 for EXAFS and Fourier transform spectra). CN = coordination number, R = interatomic distance, and σ^2 = Debye-Waller factor. 84

Table 4.4 Maximum hyperfine field (B_{HF}), quadrupole splitting (QS), and isomer shift (IS) of 0% As, 10% ADS, and 10% COP ferrihydrite samples at 4.2 K. 90

Table 4.5 Reaction orders of hydroquinone (*m*) and surface area (*n*) of 0% As, 10% ADS, and 10% COP samples. Initial rates for ferrihydrite reactions at room temperature with 0.2 mM hydroquinone and 2 g/L oxide loading. 94

Table 4.6 Rates of benzoquinone and Fe(II) formation for the reductive dissolution of 10% ADS and 10% COP ferrihydrites for reactions at room temperature with 0.05 mM hydroquinone and 2 g/L oxide loading. 98

Table 4.7 Percentages of dissolved Fe and As compared to the total amount contained in the ferrihydrite solids for equilibrium and filtrate samples of a long-term reductive dissolution reaction 100

Table 5.1 Copper content of the ZVI materials determined by ICP-AES 120

Table 5.2 Rate constants of CT reactions as determined by fitting data with the Scientist® program 124

Table 5.3 Percentage of total iron within each of the solid phases as calculated from the mass percent determined by Rietveld refinement of the powder XRD patterns. The top half of the table is results from blank reactions in buffer solution only, and the bottom half of the table is results from reactions with CT. 127

List of Figures

Figure 1.1. Crystal structures of ferrihydrite with octahedral and tetrahedral sites (left) and goethite with dioctahedral chains (right)[1] 4

Figure 2.1 XRD patterns of Fh 5.9, Fh 5.0, Fh 4.1, Fh 3.6, and Fh 3.4, all consistent with the six-line ferrihydrite (#29-713) PDF stick pattern 21

Figure 2.2 Representative TEM images of samples Fh 3.4 (top), Fh 4.1 (middle), and Fh 5.9 (bottom) 22

Figure 2.3 PDDF calculated from SAXS data. The particle size distributions extracted from the pair distance distribution function (PDDF) (a) Fh 3.4, (b) Fh 3.6, (c) Fh 4.1, (d), Fh 5.0, and (e) Fh 5.9 24

Figure 2.4 Oxygen K-edge x-ray absorption spectra of Fh 5.9, Fh 5.0, Fh 4.1, Fh 3.6, Fh 3.4 compared with a sample of bulk goethite ("Gt"). **Left** Comparison of spectra acquired in fluorescence yield (FY) mode. **Right** Comparison of absorption spectra acquired in FY (bulk sensitive) and total electron yield (TEY; surface sensitive) for selected samples 25

Figure 2.5 Plot of two kinetic trials at 21.0 ºC for the fresh suspension of Fh 5.0, including the slope and standard error of the linear trend (first six points from both trials). The solid line represents the linear regression using method of initial rates and the dashed line is an extension of linear data. 28

Figure 2.6 Benzoquinone concentration versus time (all samples have the same Fh mass loading, 1 g/L) for reactions of fresh suspensions and dried powders reacted at 25±1 ºC. The trendlines are extended beyond the linear data and represent Fh 5.9 (-·-·-), Fh 5.0 (-··-), Fh 4.1 (- - -), Fh 3.6 (·····), and Fh 3.4 (——). The slope and standard error (mM/hr) of each trendline are given to the right of each sample label. 30

Figure 2.7 Surface-area-normalized plots, determined by dividing [Q] by the appropriate value of $[S]^n$ (see text), for reactions of fresh suspensions and dried powders reacted at 25 ±1 ºC. The trendlines are extended beyond the linear data and represent Fh 5.9 (-·-·-), Fh 5.0 (-··-), Fh 4.1 (- - -), Fh 3.6 (·····), and Fh 3.4 (——). The slope and standard error (mM/hr) of each trendline are given to the right of each sample label. 31

Figure 2.8 Arrhenius plot of reactions with 1 g/L oxide loading for dried ferrihydrite samples, including the trendlines representing Fh 5.9 (-·-·-), Fh 5.0 (-··-), Fh 4.1 (- - -), Fh 3.6 (·····), and Fh 3.4 (——) 32

Figure 3.1 TEM images of ferrihydrite nanoparticles produced by hydrolysis of 5 ºC (upper) and 70 ºC (middle). The lower graph presents data from particle size measurements of ferrihydrite particle lengths obtained from calibrated TEM images 47

Figure 3.2 X-ray diffraction patterns for ferrihydrite nanoparticles synthesized by hydrolysis at 5 (lowest), 25, 50, and 70 (highest) ºC. For comparison, the powder diffraction file for six-line ferrihydrite is shown as a stick pattern at the bottom 48

Figure 3.3 TEM images of goethite nanoparticles prepared from the 5 ºC (upper) and 70 ºC (middle) ferrihydrite samples shown in Figure 3.1. The lower graph represents data from particle size measurements of goethite particle lengths obtained from calibrated TEM images..... 49

Figure 3.4 X-ray diffraction patterns for goethite nanoparticles prepared from the 5 (lowest), 25, 50, and 70 (highest) ºC ferrihydrite samples highlighted in Figure 3.2. For comparison, the powder diffraction file for goethite is shown as a stick pattern at the bottom..... 50

Figure 3.5 Two representative TEM micrographs of Fh 5 aged for 12 (upper) and 24 (lower) hours at 90 ºC..... 52

Figure 3.6 A representative TEM micrograph of Fh 85 aged for 120 h at 90 ºC 54

Figure 3.7 Plots showing the inverse number concentration of primary particles versus time (in h) for Fh 5 (upper), Fh 45 (middle), and Fh 85 (lower)..... 55

Figure 3.8 Plot of log(β_{ii}) versus nanoparticle diameter as a function of surface potential as calculated using eqs 5 and 6 in the text. Here, β_{ii} is the particle-particle coalescence rate constant for the coalescence of two identically sized and charged nanoparticles and has units of m^3/(#*s)..... 57

Figure 3.9 Plot of log(k) versus nanoparticle length as determined from the experimental data. Here, k has been calculated so that the units match those of β_{ii} (m^3/(#*s)) in Figure 3.8 57

Figure 4.1 XRD patterns 0% As, 1% ADS, 18-day 10% ADS, and 1% COP, and 10% COP. The PDF pattern for six-line ferrihydrite (#29-0712) is shown as a stick pattern 80

Figure 4.2 Representative TEM images of 0% As (upper), 18-day 10% ADS (middle), and 10% COP (lower) ferrihydrite samples. 81

Figure 4.3 Fe K-edge k^3-weighted EXAFS and corresponding Fourier transforms and fits (black = data, grey = fits) for 0%, 1-day 10% ADS, 18-day 10% ADS, and 10% COP ferrihydrite 83

Figure 4.4 ZFC/FC curves for 0% As, 18-day 10% ADS, and 10% COP samples 86

Figure 4.5 Hysteresis loops of 0% As, 18-day 10% ADS, and 10% COP ferrihydrites at 4.2 K demonstrate that the samples do not attain saturation 88

Figure 4.6 Mössbauer spectra at 4.2 K for 10% COP, 18-day 10% ADS, and 0% As ferrihydrite samples. Lines represent the best fit of experimental data (circles)..... 89

Figure 4.7 Potentiometric titrations results for 0% As (upper) and 10% COP (lower) ferrihydrite with surface charge density as a function of pH at different ionic strengths 91

Figure 4.8 Benzoquinone concentration versus time for reactions with 0.2 mM hydroquinone and 2 g/L ferrihydrite loading at 25 ±1 ºC. The trendlines are extended beyond the linear data and represent 0% As (——), 1% ADS (– – –), 1% COP (·····), 18-day 10% ADS (–···–), and 10% COP (–·–·–). The slope and standard error (mM/hr) of each trendline are given to the right of each sample label. 93

Figure 4.9 Arrhenius plot of reactions with 0.2 mM hydroquinone and 2 g/L ferrihydrite loading, including the trendlines representing 0% As (——), 18-day 10% ADS(·····), and 10% COP (– – –) ferrihydrites. 96

Figure 5.1 XRD patterns of ZVI materials with labeled peaks of Fe and Cu metal PDF reference patterns: (a) 0% Cu ZVI_{6LF}, (b) 0.08% Cu ZVI_{6LF}, (c) 0% Cu ZVI_{2LF}, (d) 0.5% Cu ZVI_{2LF}, (e) 3% Cu ZVI_{2LF}, (f) 10% Cu ZVI_{2LF}, and (g) 20% Cu ZVI_{2LF}. 121

Figure 5.2 TEM micrograph of representative ZVI materials prepared with copper. The high-resolution image (inset) includes lattice fringes of Fe and a thin corrosion layer 3-5 nm thick 122

Figure 5.3 HAADF brightfield (top left) and darkfield (bottom left) images and STEM-EDS elemental analysis of Cu, Fe, Ni, and O of 20% Cu ZVI_{2LF} 123

Figure 5.4 CT degradation for the reactions of (a) 0% Cu ZVI_{2LF} and (b) 20% Cu ZVI_{2LF}. (■) carbon tetrachloride; (▲) chloroform; solid lines are fit to carbon tetrachloride and chloroform data; the dashed line is fit to "unknown products." 125

Figure 5.5 Sample XRD pattern of 3% Cu ZVI_{2LF} post-reaction solids and Rietveld refinement composition results. Peaks were matched to the reference PDF patterns of iron metal (F), copper metal (C), magnetite (M), goethite (G), and lepidocrocite (L). 126

Figure 5.6 Image of post-reaction suspensions of (a) 0% Cu ZVI_{2LF}, (b) 0.5% Cu ZVI_{2LF}, (c) 3% Cu ZVI_{2LF}, and (d) 10% Cu ZVI_{2LF} samples that shows the formation of black products in (a) or light, yellowish-orange solid-state products in (b), (c), and (d). 128

Figure 5.7 TEM image of the post-reaction solids from the reaction of carbon tetrachloride and 0.5% Cu ZVI_{2LF}. 130

Figure 5.8 HAADF brightfield (top left) and darkfield (bottom left) images and the STEM elemental analysis of Fe, Cu, O, and Si of post-reaction materials of 20% Cu ZVI_{2LF}. 131

Figure 5.9 Small copper particles associated with needle-like iron oxide products from the reaction of 20% Cu ZVI_{2LF} particles. 132

List of Abbreviations

2LF	two-line ferrihydrite
6LF	six-line ferrihydrite
μC	microcoulomb
σ^2	Debye-Waller factor
Å	angstrom
A	Arrhenius pre-exponential factor
ADS	adsorbed
BET	Brunauer-Emmett-Tellor surface area analysis
B_{HF}	magnetic hyperfine field
CCD	charge coupled device
CF	chloroform
CN	coordination number
COP	coprecipitated
CT	carbon tetrachloride
E_a	activation energy
EDS	electron dispersive X-ray spectroscopy
eV	electron volts
EXAFS	extended X-ray absorption fine structure spectroscopy
FC	field-cooled
FY	fluorescence yield
HAADF	high angular annular dark field
ICP-AES	inductively coupled plasma-atomic emission spectrometry
ICP-MS	inductively coupled plasma-mass spectrometry
i.d.	inner diameter
IS	isomer shift
GC	gas chromatography
HPLC	high performance liquid chromatography
K	kelvin
k	rate constant

meq	milliequivalent
min	minute
MOPS	3-(N-morpholino)propanesulfonic acid
MWCO	molecular weight cut off
nm	nanometer
OA	oriented aggregation
PDF	powder diffraction file
PTFE	polytetrafluoroethylene
PZNPC	point of zero net proton charge
Q	benzoquinone
QH_2	hydroquinone
QS	quadrupole splitting
S_0^2	amplitude reduction factor
SAXS	small angle X-ray scattering
SQUID	superconducting quantum interference device
STEM	scanning transmission electron microscopy
T	Tesla
T_B	blocking temperature
T_N	Néel temperature
TEM	transmission electron microscopy
TEY	total electron yield
V	volts
V	volume
XAS	X-ray absorption spectroscopy
XRD	X-ray diffraction
Y_{CF}	chloroform yield
ZFC	zero-field-cooled
ZVI	zero-valent iron

Chapter 1

Introduction and Background

1.1 The Chemistry of Natural Systems

The chemistry of environmental systems is complex and includes a broad range of interfacial reactions and processes within the atmosphere, hydrosphere, biosphere, and lithosphere. Important natural chemical processes include the geochemical cycling of the elements and other species, and these processes can be strongly affected by anthropogenic activities. Long-lived pollutants and some naturally occurring species are concerns not only for the health of humans but also the ecosystems of our planet. Thus, the fate and transport of natural and anthropogenic species must be understood. Arsenic is an example of a naturally-occurring element found in some soil and groundwater systems, while carbon tetrachloride is an anthropogenic pollutant previously used as a refrigerant. Both arsenic and carbon tetrachloride are toxic and carcinogenic species, but their chemistry in natural systems differs greatly. Arsenic is often associated with natural iron oxide minerals which mediate its transport. Carbon tetrachloride is resistant to reaction by oxide materials in soils and sediments, but engineered zero-valent iron materials can facilitate its degradation in polluted soil sites. This document examines

the reactivity of redox-active, iron-containing particles in controlled, modeled systems in the laboratory. Specifically, results from experiments quantifying the reductive dissolution of ferrihydrite, the oxidation of carbon tetrachloride by engineered materials, and particle growth by oriented aggregation are used to enhance our understanding of how such interfacial reactions are important to the fate and transport of these species in natural systems.

1.2 Iron Oxides

Iron is the fifth most abundant element and the most important redox active metal in the Earth's crust. Iron oxides are a class of minerals that include iron oxide, iron hydroxide, and iron oxyhydroxide compounds composed of Fe, O, and/or OH species, with some also incorporating structural water. Most iron oxides incorporate Fe^{3+}, but some contain Fe^{2+}. The iron oxide structures are typically composed of close-packed arrays of anions with iron predominantly in octahedral sites and sometimes in tetrahedral sites, and polymorphs vary in their arrangement of these basic structural units.[1]

Iron oxides are ubiquitous in soils and sediments and may be the predominant reactive species in such mixtures.[1] These minerals are formed through several mechanisms, including weathering of primary minerals, redox reactions of Fe^{2+} and Fe^{3+}, and precipitation/hydrolysis reactions. Iron oxides may incorporate species such as aluminum, silicon, and arsenic into their structure.[1] Due to their natural abundance, redox reactivity, and surface adsorptivity, iron oxides play an important role in the transformation and transport of species such as heavy metals and anthropogenic contaminants.[2-4] Iron oxides may be reduced through biotic[5] or abiotic[6] electron transfer

reactions with organic compounds, including quinone species and humic substances.[7] Reductive dissolution can cause the release of adsorbed or incorporated species and can lead to growth and phase transformations.[8]

1.2.1 *Ferrihydrite*

One iron oxide mineral, ferrihydrite ($Fe_5HO_8 \cdot 4H_2O$), precipitates when iron-rich waters increase in pH and/or become oxidized.[1,9] Ferrihydrite is reddish-brown in color and typically ranges in size from 3-10 nanometers.[1] It is a poorly crystalline, metastable mineral and is a precursor to more stable iron oxides, such as goethite and hematite.[10] The high degree of structural disorder and high specific surface area of ferrihydrite make it one of the most reactive iron oxide minerals. Ferrihydrite is typically described as two- or six-line ferrihydrite based on the number of peaks observed in the powder X-ray diffraction pattern. Recently, Michel et al. proposed a single structure of ferrihydrite based on total X-ray scattering data and pair distribution function analysis (Figure 1.1). Samples of ferrihydrite with average sizes of 2, 3, and 6 nm were hypothesized to have the same structure (hexagonal space group $P6_3mc$). Although a size-dependent relaxation of the lattice parameters and small changes in occupancy were observed, they concluded that the underlying structure was not size-dependent.[11]

Ferrihydrite can incorporate ions, such as arsenate, from solution and, therefore, may influence the transport of such species in natural systems. The fundamental mechanisms and rates of precipitation, dissolution, and redox are affected by the presence of such species in solution, adsorbed onto mineral surfaces, or incorporated into the bulk of the iron oxide minerals.[12] In particular, arsenic is frequently associated with iron in sediment materials. Due to its high affinity for iron oxides, arsenic

concentrations in natural ferrihydrite samples have been documented with values up to 14 wt% As.[13] Arsenic may be released from or adsorb onto iron oxide surfaces depending on the groundwater solution properties, especially pH and redox conditions.[14] For example, reductive dissolution of arsenic-bearing ferrihydrites can cause the release of adsorbed or incorporated arsenic and can also lead to growth and phase transformations.[8]

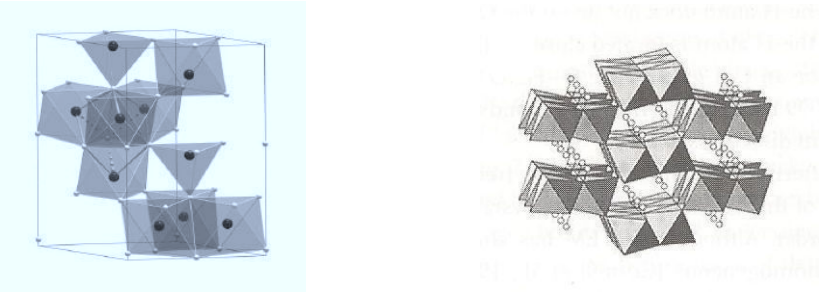

Figure 1.1. Crystal structures of ferrihydrite with octahedral and tetrahedral iron sites (left)[11] and goethite with dioctahedral chains (right).[1]

1.2.2 *Goethite*

Goethite, α-FeOOH, is yellow and responsible for the color of many rocks and soils. It is one of the most stable iron oxides at ambient temperatures and is typically the final product of iron oxide phase transformations. Goethite is isostructural with diaspore, and its crystal structure is composed of double chains of octahedra (Figure 1.1). Goethite crystals are typically acicular and range in length from tens of nanometers to several microns.[1] The {100} faces grow rapidly, so synthetic, acicular goethite crystals are elongated along the [100] direction. [1] Hydrothermal aging of ferrihydrite can lead to growth by oriented aggregation and transformation into goethite.[15]

1.2.3 *Magnetic Properties of Ferrihydrite and Goethite*

Ferrihydrite and goethite are both antiferromagnetic materials and exhibit superparamagnetic behavior at room temperature.[1,16] In antiferromagnetic materials, the electron spins of iron ions in the crystal lattice are of equal magnetic moment and have antiparallel alignment and, therefore, have no net magnetic moment. Superparamagnetism arises from magnetic anisotropy, which is the preferred alignment of electron spins along one or a few crystallographic axes. The magnetism along the preferred axes can be reversed if sufficient energy is supplied, and samples at room temperature have enough energy to rapidly exchange between the spin states. But below a certain temperature, referred to as the blocking temperature (T_B), superparamagnetic particles remain ordered. Furthermore, ferrihydrite has a magnetic moment attributed to uncompensated surface spins.[17]

1.3 Zero-Valent Iron

Zero-valent iron (ZVI) can serve as an electron donor in the reductive degradation and transformation of chlorinated organics, heavy metals, and inorganic species to reduce contaminant concentrations or minimize the mobility of such substances in subsurface environments.[18,19] ZVI particles typically have an Fe^0 core that can serve as an electron donor and active material for remediation of contaminated sites. Several sites have been remediated by the placement of permeable reactive barrier systems, in which groundwater flows through an engineered wall of ZVI materials.[18] The dissolved groundwater contaminants are transformed, precipitated, or adsorbed by contact with the reactive ZVI. In other cases, colloidal particles less than 1 μm, and particularly nano-sized, ZVI can be suspended and injected into contaminated soil,

sediment, or aquifer areas for treatment.[20,21] The incorporation or coating of ZVI particles with an additive a metal has been found to enhance the reactivity and may influence the distribution of reaction products. Noble metals like Pd on the ZVI surface oxidize less readily than Fe^0 and are preserved, but the mechanism of the enhanced reactivity has not been determined.[19] The identity, method of incorporation, and relative amount of the additive metal are expected to influence the degradation rate and products.[22-26]

1.4 Scope of Dissertation

This document is dedicated to the investigation of ferrihydrite and zero-valent iron reactivity. To draw insights between the chemical and physical properties of the model materials, ferrihydrite and ZVI model materials of were first prepared, then were well characterized, and finally, studied by kinetic investigations. Kinetic studies included the reductive dissolution of ferrihydrites by hydroquinone, the growth and transformation of ferrihydrite into goethite, and the reductive dechlorination of carbon tetrachloride by zero-valent iron materials. Chapter 2 highlights the effect of ferrihydrite particle size on the rates of reductive dissolution. The influence of ferrihydrite particle size on the kinetics of oriented aggregation to produce goethite is outlined in Chapter 3. Next, the kinetic investigation of ferrihydrites with adsorbed or coprecipitated arsenate is presented in Chapter 4. And Chapter 5 features the reductive dechlorination reactions of carbon tetrachloride and ZVI materials with copper additives.

1.5 References

1. Cornell, R. M.; Schwertmann, U., *The Iron Oxides: Structure, Properties, Reactions, Occurrences and Uses*. 2nd ed.; Wiley-VCH: Weinheim, 2003.

2. Ford, R. G.; Bertsch, P. M.; Farley, K. J. Changes in transition and heavy metal partitioning during hydrous iron oxide aging. *Environmental Science and Technology* **1997** 31, 2028.

3. Chun, C. L.; Penn, R. L.; Arnold, W. A. Kinetic and microscopic studies of reductive transformations of organic contaminants on goethite. *Environmental Science and Technology* **2006** 40, 3299.

4. Stipp, S. L. S.; Hansen, M.; Kiristensen, R.; Hochella, M. F., Jr.; Bennedsen, L.; Dideriksen, K.; Balic-Zunic, T.; Leonard, D.; Mathieu, H.-J. Behaviour of Fe-oxides relevant to contaminant uptake in the environment. *Chemical Geology* **2002** 190, 321.

5. Straub, K. L.; Benz, M.; Schink, B. Iron metabolsim in anoxic environments at near neutral pH. *FEMS Microbiology Ecology* **2001** 34, 181.

6. LaKind, J. S.; Stone, A. T. Reductive dissolution of goethite by phenolic reductants. *Geochimica et Cosmochimica Acta* **1989** 53 (5), 961.

7. Scott, D. T.; McKnight, D. M.; Blunt-Harris, E. L.; Kolesar, S. E.; Lovley, D. R. Quinone moieties act as electron acceptors in the reduction of humic substances by humics-reducing microorganisms. *Environmental Science and Technology* **1998** 32, 2984.

8. Pederson, H. D.; Postma, D.; Jakobsen, R. Release of arsenic associated with the reduction and transformation of iron oxides. *Geochimica et Cosmochimica Acta* **2006** 70, 4116.

9. Jambor, J. L.; Dutrizac, J. E. Occurrence and constitution of natural and synthetic ferrihydrite, a widespread iron oxyhydroxide. *Chemical Reviews* **1998** 98, 2549.

10. Penn, R. L.; Tanaka, K.; Erbs, J. J. Size dependent kinetics of oriented aggregation. *Journal of Crystal Growth* **2007** 309, 91.

11. Michel, F. M.; Ehm, L.; Antao, S. M.; Lee, P. L.; Chupas, P. J.; Liu, G.; Strongin, D. R.; Schoonen, M. A. A.; Phillips, B. L.; Parise, J. B. The structure of ferrihydrite, a nanocrystalline material. *Science* **2007** 316, 1726.

12. Stumm, W.; Morgan, J. J., *Aquatic Chemistry, Chemical Equilibria and Rates in Natural Waters*. 3rd ed.; John Wiley & Sons, Inc.: New York, 1996.

13. Rancourt, D. G.; Fortin, D.; Pichler, T.; Thibault, P.-J.; Lamarche, G.; Morris, R. V.; Mercier, P. H. J. Mineralogy of a natural As-rich hydrous ferric oxide coprecipitate formed by mixing of hydrothermal fluid and seawater: Implications regarding surface complexation and color banding in ferrihydrite deposits. *American Mineralogist* **2001** 86, 834.

14. Smedley, P. L.; Kinniburgh, D. G. A review of the source, behavior and distribution of arsenic in natural waters. *Applied Geochemistry* **2002** 17, 517.

15. Burleson, D. J.; Penn, R. L. Two-step growth of goethite from ferrihydrite. *Langmuir* **2006** 22, 402.

16. Guyodo, Y.; Banerjee, S. K.; Penn, R. L.; Burleson, D.; Berquó, T. S.; Seda, T.; Solheid, P. Magnetic properties of synthetic six-line ferrihydrite nanoparticles. *Physics of the Earth and Planetary Interior* **2006** 154, 222.

17. Berquó, T. S.; Erbs, J. J.; Lindquist, A.; Penn, R. L.; Banerjee, S. K. Effects of magnetic interactions in antiferromagnetic ferrihydrite particles. *Journal of Physics: Condensed Matter* **2009** 21, 176005.

18. Li, X.-q.; Elliot, D. W.; Zhang, W.-x. Zero-valent iron nanoparticles for abatement of environmental pollutants: materials and engineering aspects. *Critical Reviews in Solid State and Materials Sciences* **2006** 31, 111.

19. Li, L.; Fan, M.; Brown, R. C.; Van Leeuwen, J.; Wang, J.; Wang, W.; Song, Y.; Zhang, P. Synthesis, properties, and environmental applications of nanoscale iron-based materials: A review. *Critical Reviews in Environmental Science and Technology* **2006** 36, 405.

20. Zhang, W.-x. Nanoscale iron particles for environmental remediation: An overview. *Journal of Nanoparticle Research* **2003** 5, 323.

21. Lien, H.-L.; Zhang, W.-x. Transformation of chlorinated methanes by nanoscale iron particles. *Journal of Environmental Engineering* **1999** 125 (11), 1042.

22. Bransfield, S. J.; Cwiertny, D. M.; Roberts, A. L.; Fairbrother, D. H. Influence of copper loading and surface coverage on the reactivity of granular iron toward 1,1,1-trichloroethane. *Environmental Science and Technology* **2006** 40, 1485.

23. Cwiertny, D. M.; Bransfield, S. J.; Livi, K. J. T.; Fairbrother, D. H.; Roberts, A. L. Exploring the influence of granular iron additives on 1,1,1-trichloroethane reduction. *Environmental Science and Technology* **2006** 40, 6837.

24. Kim, Y.-H.; Carraway, E. R. Reductive dechlorination of TCE by zero valent bimetals. *Environmental Technology* **2003** 24 (1), 69.

25. Cwiertny, D. M.; Bransfield, S. J.; Roberts, A. L. Influence of the oxidizing species on the reactivity of iron-based bimetallic reductants. *Environmental Science and Technology* **2007** 41, 3734.

26. Xu, Y.; Zhang, W.-x. Subcolloidal Fe/Ag particles for reduction of chlorinated benzenes. *Industrial & Engineering Chemistry Research* **2000** 39 (7), 2238.

Chapter 2

Influence of Size on the Reductive Dissolution of Six-Line Ferrihydrite*

2.1 Chapter Summary

This work investigates size dependence of the kinetics of reductive dissolution of six-line ferrihydrite, ranging in average length from 3.4 to 5.9 nm. Empirical rate laws, activation energies, and pre-exponential factors were determined for freshly prepared aqueous suspensions and dried powders of each ferrihydrite sample. Mass normalized initial rates of reductive dissolution are substantially faster for the freshly prepared suspensions than for reactions using the dried powders, which is consistent with a drop in reactive surface area upon drying. In addition, results demonstrate substantial differences between the empirical rate laws for the freshly prepared and the dried six-line ferrihydrite. Comparing surface-area-normalized rates of reductive dissolution reveals a small dependence on size for the freshly prepared ferrihydrite, no

dependence on size for the dried ferrihydrite nanoparticles, and no statistically significant change in the activation energy for reaction in either case. In addition, X-ray diffraction and X-ray absorption studies revealed no size dependent changes in nanoparticle structure and electronic structure. However, the frequency of reagent-surface encounters, related to the pre-exponential factors increased significantly with decreasing particle size, consistent with the hypothesis that the ordering of water molecules at ferrihydrite nanoparticle surfaces mediates diffusion to the surface and is size dependent.

2.2 Introduction

Iron oxides, including iron oxide and (oxy)hydroxide minerals, are commonly found in the environment and range in size from a few to several hundred nanometers in soils. These minerals are formed through several mechanisms, including weathering of primary minerals, redox reactions of Fe^{II} and Fe^{III}, and precipitation/hydrolysis reactions.[1] Due to their natural abundance, redox reactivity, and surface adsorptivity, iron oxides play an important role in the transformation and mobility of such species as arsenic, heavy metals, and anthropogenic contaminants.[2-4] Iron oxides may be reductively dissolved through biotic[5] or abiotic[6] electron transfer reactions with organic compounds, including quinone species and humic substances.[7] Reductive dissolution can cause the release of adsorbed or incorporated species and can lead to mineral dissolution, growth, and phase transformations.[8]

One such iron oxide is ferrihydrite ($Fe_5HO_8 \cdot 4H_2O$),[1] a poorly crystalline, metastable mineral that is observed only as nanoparticles and is the precursor to the more stable iron oxides goethite and hematite.[1] It is typically described as two- or six-

line ferrihydrite based on the number of peaks observed in the powder X-ray diffraction pattern, and its structure is controversial. Recently, Michel et al. refined a single structure of ferrihydrite using total X-ray scattering data and pair distribution function analysis. Samples of ferrihydrite with average sizes of 2, 3, and 6 nm were found to possess the same structure (hexagonal space group $P6_3mc$). Although a size-dependent relaxation of the lattice parameters and small changes in occupancy were observed, the underlying structure was not size-dependent.[9] Previous work has shown that ferrihydrite is much more reactive compared to other iron oxides,[10] which is attributed to its high degree of structural disorder and high specific surface area. However, the precise relationships between the size, structure, and reactivity of ferrihydrite nanoparticles have not been established.

The physical, chemical, magnetic, and optical properties of nanoparticles are known in many cases to differ from larger crystallites,[11] and corresponding effects on chemical reactivity have also been observed.[12,13] In particular, size has been implicated as a major influence on iron oxide redox reactivity and adsorptivity.[14-18] For example, Madden et al. investigated the adsorption of copper onto hematite with average sizes of 7, 25, and 88 nm. The surface-area-normalized adsorption affinity of the 7-nm hematite was higher than for the 25- and 88-nm samples, for which similar surface-area-normalized affinities were observed. The result was attributed to iron's altered coordination environment near edges and a higher percentage of edge sites for the 7-nm sample than for the 25- and 88-nm samples.[16] Previous studies of adsorption onto goethite particles also observed size-dependent changes in surface-area-normalized

affinities that were attributed to variation in site density,[17] surface charge,[18] or structural disorder[13] with size.

Several investigators have studied how particle size, and hence surface area, affects the rates of interfacial reactions involving nanoparticles.[19,20] Liou et al. studied the influence of size on copper nanoparticle reactivity, quantifying the surface-area-normalized rate constants (k_{SA}) of reaction for degradation of carbon tetrachloride.[20] The experimental values of k_{SA} for experiments employing 10-nm and 20- to 50-nm copper nanoparticles were at least 100 times and 10 times, respectively, greater than the k_{SA} for a commercial powder of Cu. Because the rate constants were surface-area-normalized, the results suggest that the smaller samples have a higher density of active sites. Thus there are several indications that the effective reactivity of nanoscale materials is highly correlated with the presence, site density, and chemical reactivity of active surface sites such as defect sites.

The goal of this work was to determine the effect of size on the chemical reactivity of ferrihydrite measured by monitoring the kinetics of reductive dissolution by hydroquinone. Previous work by Penn et al. demonstrated that the average size of six-line ferrihydrite can be controlled by hydrolysis temperature.[21] This chapter examines the properties of five well characterized ferrihydrite samples prepared using a method similar to Penn et al. and hydrolysis temperatures ranging from 4 to 80 ºC (average sizes ranging from 3.4 to 5.9 nm). The samples were characterized using electron microscopy, X-ray diffraction, and X-ray absorption spectroscopy to investigate whether particle morphology, structure, or electronic properties were affected by size. The kinetics of reductive dissolution were quantified, for both fresh

suspensions and dried powder samples, using a model adapted from Johnson et al.[19] that is appropriate for interfacial reactions occurring preferentially at distinct sites, such as defects. The Arrhenius equation was applied to determine the influence of particle size and sample treatment on activation energy and pre-exponential factor.

2.3 Experimental Methods

2.3.1 *Synthesis of Materials*

Six-line ferrihydrite samples were prepared using the method of Penn et al.[21] All solutions were prepared using 18 MΩ•cm resistivity water (Milli-Q water, Millipore Corporation). All glassware and Nalgene bottles were acid washed with 4 M nitric acid and rinsed three times with Milli-Q water. Ferrihydrite suspensions were prepared by the controlled addition of a 0.48 M $NaHCO_3$ (Mallinckrodt) solution to an equal volume of 0.40 M $Fe(NO_3)_3$•$9H_2O$ (Fisher) with vigorous stirring. The ferric nitrate solution was equilibrated to 4, 23, 45, 66, or 80 ºC using an ice bath or heated water bath before hydrolysis, and the temperature was maintained during hydrolysis. The base solution was added over 12 ±1 minutes using a Fisher peristaltic pump, and twelve inches of tubing was submerged in the constant temperature bath to ensure a consistent temperature during hydrolysis. For heated samples, the bottle of suspension was immediately submerged in an ice bath and cooled to room temperature. Next, the ferrihydrite suspension was microwave-annealed (950 Watt oven) for 30-second intervals until it boiled. The bottle containing the suspension was immediately submerged into an ice bath until it was cooled to room temperature. Each resulting suspension was then transferred to Spectra-Por #7 dialysis bags (MWCO = 2000 g/mol). Dialysis against Milli-Q water was performed at 10 ºC for three days, changing

the water a total of at least nine times. One-quarter of each suspension was kept at 10 ºC for reaction without drying, and such samples are hereafter referred to as freshly prepared suspensions. The other portion was allowed to air-dry for five days, ground into a powder using an agate mortar and pestle, and stored in glass vials.

2.3.2 ***Materials Characterization***

Powder X-ray diffraction (XRD) was performed using a PANalytical X-Pert PRO MPD X-ray diffractometer equipped with a cobalt source and an X-Celerator detector. Data was collected over the range of 10-90º 2θ at a scan rate of 0.6º per minute. The diffraction patterns were compared to the reference powder diffraction files (PDF) for six-line ferrihydrite (#29-713), goethite (#29-712), and hematite (#33-664).

Each transmission electron microscopy (TEM) sample was prepared by diluting one drop of suspension into 3 mL of Milli-Q water. A drop of the resulting diluted suspension was placed onto a 3 mm 200 mesh holey carbon-coated copper grid (Structure Probe, Inc.) and then allowed to air-dry. Images were collected using an FEI Tecnai T12 microscope, operated at 120 kV, and a Gatan CCD camera. The size and morphology of the particles were analyzed from calibrated TEM images using Gatan Digital Micrograph 3.8.2, and the lengths of more than 500 particles were measured. The specific surface area was calculated using the surface area per volume and the density of ferrihydrite (3.96 g/cm^3).[1] The surface area of each sample was calculated by assuming an aspect ratio of 1.3, based on the results of Penn et al.[21] and verified for the 4 and 45 ºC samples, and modeling the particles as ellipsoids as in Jentzsch and Penn.[22]

Small angle X-ray scattering (SAXS) sample suspensions were prepared using fresh ferrihydrite suspensions and diluted 1:4 with 40 mM acetate buffer (pH 3.75), and

all measurements were made at room temperature. Samples were analyzed using the Anton-Par SAXSess instrument equipped with a Cu Kα slit-collimated radiation source. The instrumentation, data collection, and data analysis are described in detail in Kumar et al.[23] Slit collimation is beneficial because a larger volume of sample is illuminated at once and the data collection time is reduced without a reduction of measured intensity. The scattering profile from a line collimated beam is "smeared" due to the incident beam geometry but can be accounted for during data analysis using the software program GIFT. The scattering vector q was determined from the scattering angle θ through use of the relationship $q = 4\pi\lambda^{-1}\sin(\theta/2)$. The result of the SAXS data analysis is the pair distance distribution function (PDDF) from which the particle size distribution is extracted.

Oxygen K-edge X-ray absorption spectroscopy (XAS) was performed at beamline 7.0 at the Advanced Light Source with an X-ray energy resolution of approximately 0.3 eV. Portions of dried ferrihydrite samples were pressed into indium for analysis under vacuum. The X-ray absorption spectra were collected in fluorescence yield, and total electron yield signals were collected simultaneously and normalized to the incident intensity. The X-ray energy was calibrated with respect to literature data using a spectrum collected from powdered bulk hematite, applying a constant offset to set the inflection point of the hematite pre-edge absorption onset to 530.0 eV. The XAS intensities were normalized to unity edge jump at 550 eV.

2.3.3 *Kinetic Reactions*

The reactivity of iron oxides has been quantified previously by measuring the kinetics of reductive dissolution using hydroquinone, and monitoring the transformation

of hydroquinone to benzoquinone.[6,10,14,22] Here, reactions were performed using either the freshly prepared ferrihydrite suspensions, within ten days of synthesis, or the dried powders. The storage temperature (10 ºC) was controlled for the fresh suspensions. An aging study using fresh ferrihydrite suspensions provided evidence that the extent of spontaneous transformation to goethite was very small within a period of a few weeks and was slower than at room temperature. In addition, the reactivity of dried powders was investigated. Dried powders are generally much less susceptible to phase transformation, and this was confirmed for dried ferrihydrite by comparing XRD patterns of a fresh powder and the powder after several months of storage at room temperature in air. Furthermore, dried samples are commonly used in iron oxide reactivity studies, owing mainly to the ease of handling and quantifying masses of such materials. All experiments were performed in duplicate using acetate buffer (40 mM, pH 3.75, acetic acid (Mallinckrodt) and sodium hydroxide (Mallinckrodt) in Milli-Q water) and in an anaerobic chamber (Coy Laboratories). Amber glass vials (30 mL) served as the reaction vessels for the temperature dependence experiments, and 30 mL Nalgene bottles were used for room temperature experiments. The Nalgene bottles were wrapped in aluminum foil to prevent exposure to light, as benzoquinone is known to photodegrade.

Suspensions were diluted to achieve a specific mass of ferrihydrite per volume loading (0.2-1.0 g/L) in each experiment. Three milliliters of stock ferrihydrite suspension was added to each vial and diluted with 9.0 mL of 53.3 mM acetate buffer (final buffer concentration was 40 mM). The samples were kept at room temperature or placed in an ice bath or silicon oil bath (reaction temperature range: 2.0-38.0 ±0.5 ºC)

and allowed to equilibrate to the desired temperature. To initiate the reaction, 0.5 mL of 10 mM hydroquinone (Sigma, 99%) stock solution (prepared using 40 mM acetate buffer) was added. Each suspension was continuously stirred with a magnetic stir bar, and the temperature was monitored and recorded throughout the reaction period. For reaction order studies, the total volume of suspension was 25.0 mL, with 0.2-1.0 g/L ferrihydrite loading, 8-40 μM hydroquinone, and 40 mM acetate buffer (pH 3.75). Aliquots were removed at regular time intervals and analyzed immediately (<1 min) by high performance liquid chromatography (HPLC), as described below. Filtering the aliquots did not remove the ferrihydrite particles effectively and was not performed for kinetic studies of the fresh ferrihydrite suspensions.

Similar reaction conditions were used in the reactions of the dried ferrihydrite materials. The dried powder was weighed out and put into either the amber or Nalgene bottles. The bottles were placed in the anaerobic chamber and 5.0 mL of deoxygenated 40 mM acetate buffer was added. Samples were sonicated, vortexed, and stirred overnight to reduce particle aggregation. Magnetic stirring was employed. The following day, the appropriate volume of acetate buffer and then 10 mM hydroquinone stock solution (prepared with 40 mM acetate buffer) were added to the reaction vessel. The total volume of suspension was 25.0 or 12.5 mL, with 0.4-1.5 g/L ferrihydrite loading, 8-40 μM hydroquinone, and 40 mM acetate buffer (pH 3.75). At regular time intervals, 1-mL aliquots of the reaction mixture were filtered using 0.2 μm nylon Acrodisc filters into amber vials and analyzed by HPLC. The filtrate was clear, indicating that the solid was effectively removed from the reaction mixture, thus quenching the reaction.

Solutions were analyzed for hydroquinone and benzoquinone concentrations using an Agilent HPLC equipped with a Zorbax C_{18} column. The mobile phase was a 65:35 mixture of acetate buffer (40 mM, pH 3.75) and acetonitrile. The flow rate was 1.0 mL/min, and the injection volume was 10 μL. The absorbance at 235 nm was monitored, and hydroquinone eluted at 1.7 min and benzoquinone at 2.5 min. Eight-point calibration curves, ranging from 0.05 to 2.0 mM for hydroquinone and 2 to 150 μM for benzoquinone, were used to determine experimental concentrations.

2.3.4 ***Analysis of Kinetics Data***

Johnson et al. developed a pseudo-first-order kinetic model to describe the results of several iron metal and halocarbon pollutant reactivity studies. The reactions were first-order with respect to the contaminant concentration and with respect to the amount of metal available for reaction. The model expanded k_{obs} to consider surface area,[19]

$$-\frac{\mathrm{d[P]}}{\mathrm{d}t} = k_{SA} a_s \rho_m [\mathrm{P}] \qquad (1)$$

where k_{SA} is the specific reaction rate constant (L/hr/m^2), a_s is the specific surface area of solid (m^2/g), ρ_m is the mass loading of solid (g/L of solution), and P represents the pollutant molecule degraded. Still, k_{SA} may vary due to differences between the measured physical surface area and the reactive surface area that contributes directly to the degradation of the pollutant. Thus, Johnson et al. also developed an empirical kinetic model in terms of reactive surface sites to quantify the effect of variation in specific reactivity of the metal surface[19]

$$-\frac{\mathrm{d[P]}}{\mathrm{d}t} = k_2 \Gamma \rho_a [P] \quad (2)$$

where k_2 is the second-order rate constant for reduction at a particular type of site (L/hr/mol) and Γ is the surface concentration of reactive sites (mol/m^2 of solid). This model is appropriate for degradation that occurs preferentially at distinct sites, such as defects.

2.4 Results and Discussion

2.4.1 *Structural Analysis*

All five powder X-ray diffraction patterns (Figure 2.1) matched well with the six-line ferrihydrite reference pattern (PDF #29-713), and there was no evidence for the presence of other crystalline iron oxide phases. The six characteristic lines of six-line ferrihydrite narrow substantially as a function of increasing hydrolysis temperature, without the appearance of new peaks, which is consistent with an increase in particle size.

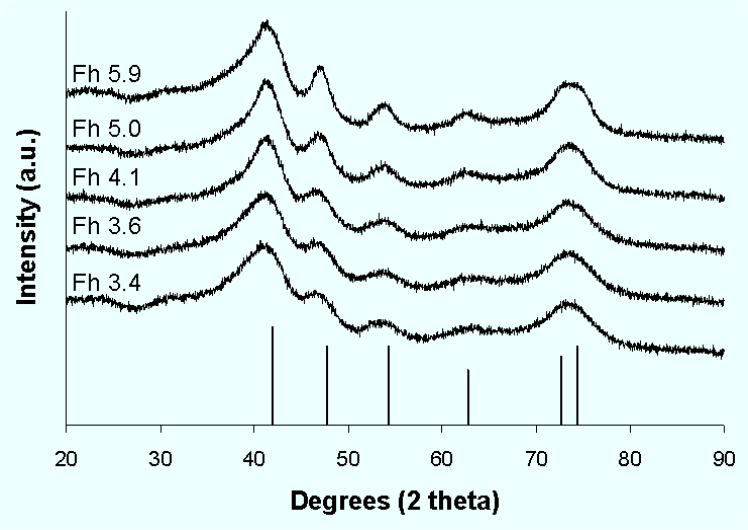

Figure 2.1 XRD patterns of Fh 5.9, Fh 5.0, Fh 4.1, Fh 3.6, and Fh 3.4, all consistent with the six-line ferrihydrite (#29-713) PDF stick pattern.

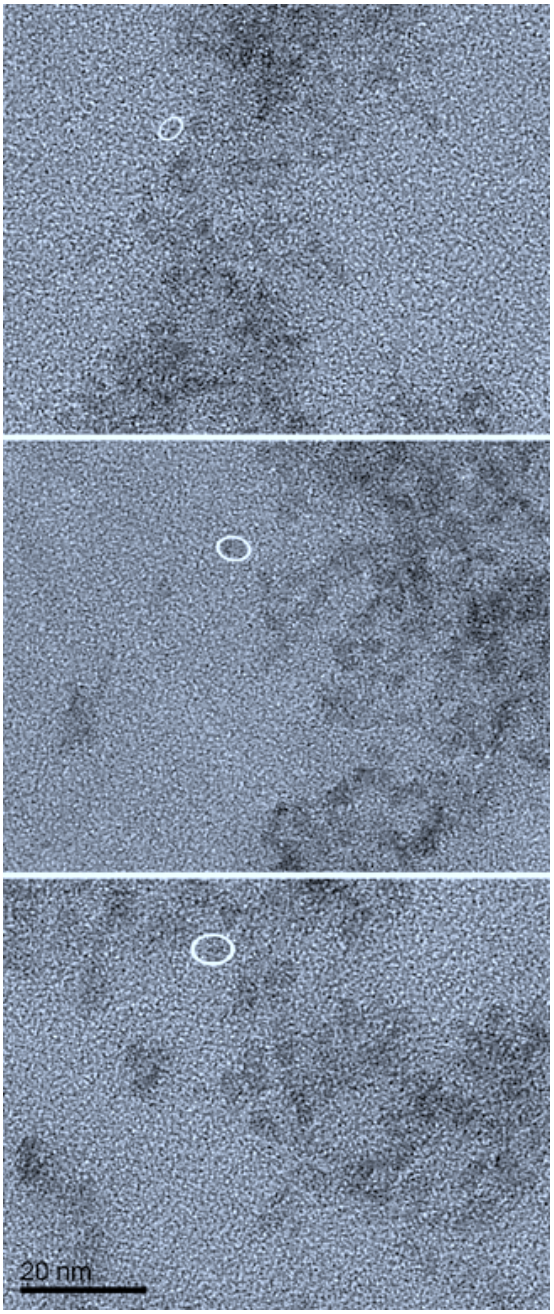

Figure 2.2 Representative TEM images of samples Fh 3.4 (top), Fh 4.1 (middle), and Fh 5.9 (bottom).

2.4.2 *Particle Size*

Representative TEM images of the 4, 45, and 80 ºC ferrihydrite samples are shown in Figure 2.2. Table 2.1 presents the average particle lengths with standard deviations and calculated surface areas (using the verified aspect ratio of 1.3) for each sample. Consistent with the results of Penn et al., the average particle length increased from 3.4 to 5.9 nm with increasing hydrolysis temperature from 4 to 80 ºC.[21] The calculated surface areas ranged from 510 to 290 m^2/g. The samples are hereafter labeled according to the average particle length as measured from the TEM images: Fh 3.4, Fh 3.6, Fh 4.1, Fh 5.0 and Fh 5.9. The SAXS data was analyzed to produce a pair distance distribution function (PDDF) that portrays the distribution of particle sizes in a suspension and from which the mean particle diameter can be estimated. The PDDF graph (Figure 2.3) confirmed the general trend of increasing average particle size with increasing synthetic temperature. Additionally, the absence of a significant secondary population in the PDDF graph verified that the particles were not aggregated in fresh suspensions, in agreement with Gilbert et al.[24]

Table 2.1 Average particle length distributions (with standard deviations as error) and surface areas for ferrihydrite as determined using TEM.

sample	hydrolysis temperature (ºC)	particle length (nm)	specific surface area* (m^2/g)
Fh 3.4	4 ± 1	3.4 ± 0.4	510
Fh 3.6	23 ± 1	3.6 ± 0.4	480
Fh 4.1	45 ± 1	4.1 ± 0.4	420
Fh 5.0	66 ± 2	5.0 ± 0.5	350
Fh 5.9	80 ± 3	5.9 ± 0.7	290

*Specific surface areas were calculated assuming an aspect ratio of 1.3 and an ellipsoidal shape.

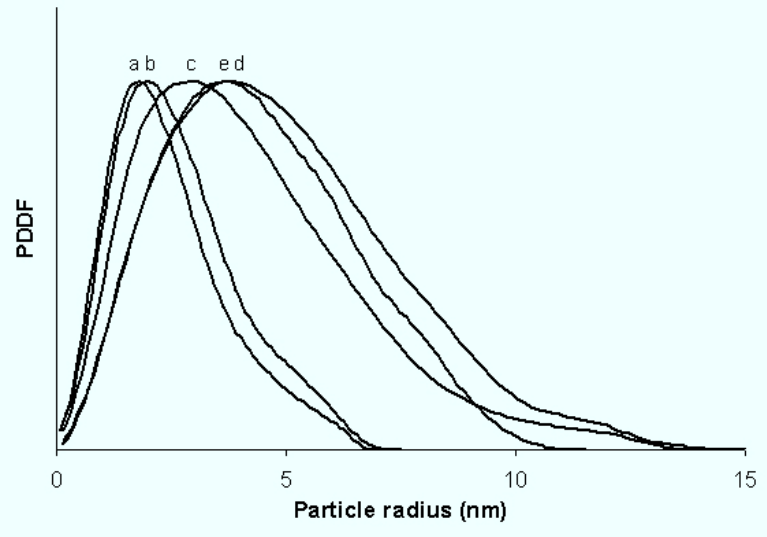

Figure 2.3 PDDF calculated from SAXS data. The particle size distributions extracted from the pair distance distribution function (PDDF) (a) Fh 3.4, (b) Fh 3.6, (c) Fh 4.1, (d), Fh 5.0, and (e) Fh 5.9.

2.4.3 *Electronic Structure*

Figure 2.4 reports the oxygen K-edge X-ray absorption spectra (XAS) acquired in the fluorescence yield mode from the ferrihydrite nanoparticles and one sample of bulk goethite. In O K-edge XAS of iron oxides and oxyhydroxides, X-ray photoexcitation of O *1s* electrons to unoccupied electronic states in the conduction band reveals the energy positions of unfilled Fe *3d* states in the pre-edge region.[25] For minerals containing ferric iron in approximately octahedral coordination with oxygen, such as hematite and goethite, unfilled Fe *3d* states with e_g and t_{2g} symmetry are split into two distinct energy positions. In iron oxyhydroxides such as goethite, the binding energy of O *1s* electrons in bridging oxygen and bridging hydroxide sites are also different. Hence the pre-edge oxygen XAS of goethite originates from transitions from

O *1s* states at two binding energies to Fe *3d* states also at two energy positions. Of the four expected peaks, only three are distinguishable due to overlap.

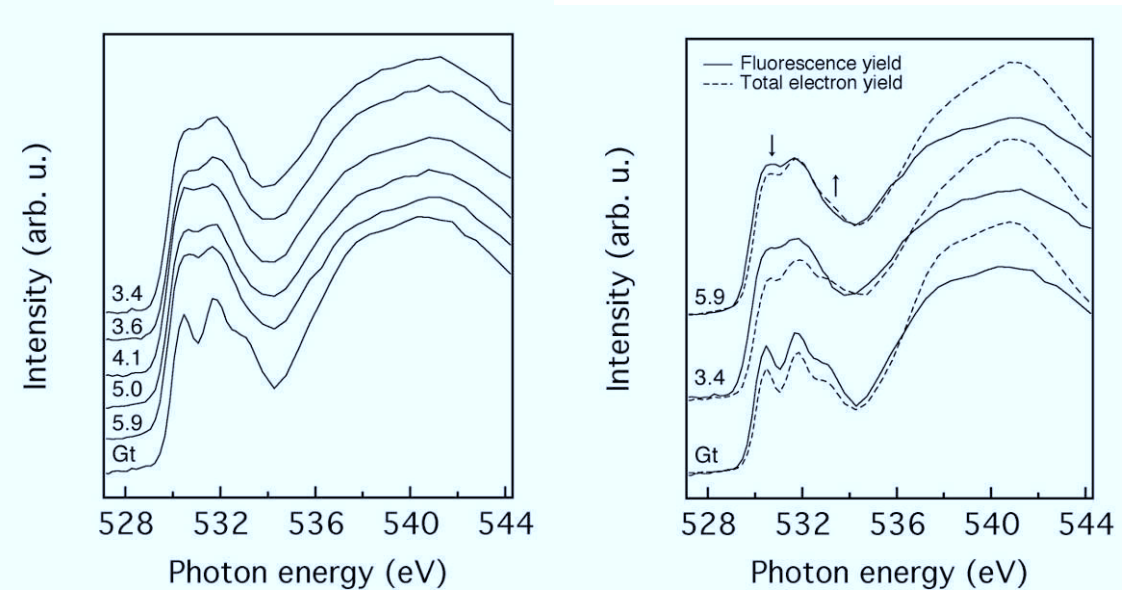

Figure 2.4 Oxygen K-edge x-ray absorption spectra of Fh 5.9, Fh 5.0, Fh 4.1, Fh 3.6, Fh 3.4 compared with a sample of bulk goethite ("Gt"). **Left** Comparison of spectra acquired in fluorescence yield (FY) mode. **Right** Comparison of absorption spectra acquired in FY (bulk sensitive) and total electron yield (TEY; surface sensitive) for selected samples.

The XAS of ferrihydrite cannot be confidently interpreted because its precise structure and stoichiometry remain uncertain. However, the XAS data are consistent with a low fraction of structural hydroxylated oxygen sites, in agreement with Michel et al., causing a narrower pre-edge feature dominated by the energy splitting of the Fe *3d* states. Figure 2.4 additionally compares the fluorescence yield (FY) *vs*. total electron yield (TEY) spectra of selected samples. Due to the greater penetration through solids of X-ray photons compared to the electrons that contribute to the TEY signal, the FY signal averages over entire nanoparticles while the TEY signal is more surface-

sensitive. The surface-sensitive signal evolves with decreasing particle size to approach more closely the spectra from the goethite reference. This does not indicate that smaller particles possess a surface goethite-like structure, since oxygen XAS of iron oxyhydroxide minerals are all quite similar.[25] Rather, the comparison indicates that oxygen sites at ferrihydrite surfaces are highly protonated, even under vacuum. It is not possible to use these data to investigate whether there are changes in surface protonation density as a function of size: the trend with particle size can be qualitatively explained simply as caused by the changing surface area to volume ratio.

The oxidation of reagents at the surface of semiconductor minerals requires electron transfer to the conduction band.[26] Consequently, the XAS experiments provide a way to test for the presence of size- or structure-dependent modifications in the ferrihydrite conduction band that could alter the thermodynamics of chemical or photoreduction. We determined the position of the absorption threshold by fits to the pre-edge region. The absorption onset is constant to within experimental error (<0.1 eV), showing that there is no size dependence of the electronic structure of ferrihydrite on particle size in the range studied.

2.4.4 *Kinetic Reactions*

The reaction mechanism between hydroquinone and iron oxides, as discussed in the literature,[6,10,26] involves the adsorption of hydroquinone at an Fe^{III} surface site, electron transfer to produce a semiquinone radical and Fe^{II}, desorption of the semiquinone, and dissolution of Fe^{II} to regenerate the Fe^{III} surface site. The process is repeated with the semiquinone radical rather than hydroquinone, and another Fe^{II} is produced along with benzoquinone. The expected half and overall reactions between

ferrihydrite and hydroquinone (QH_2) to produce benzoquinone (Q), aqueous Fe(II), and water can be written as[14,22]

$$2Fe_5HO_8{\bullet}4H_2O(s) + 10e^- + 30H^+(aq) \rightarrow 10Fe^{2+}(aq) + 24H_2O(l) \quad (3)$$

$$5QH_2(aq) \rightarrow 5Q(aq) + 10e^- + 10H^+(aq) \quad (4)$$

$$2Fe_5HO_8{\bullet}4H_2O(s) + 5QH_2(aq) + 20H^+(aq) \rightarrow 10Fe^{2+}(aq) + 5Q(aq) + 24H_2O(l) \quad (5)$$

The rate of reaction was quantified by monitoring the formation of benzoquinone over time. Using the method of initial rates,[27] the rate was determined using 3-10 data points from each trial (6-20 points for each sample; Figure 2.5). Rate constants were calculated using the measured rate of reaction and experimental orders with respect to hydroquinone and the particle surface area (S) concentrations according to the empirical rate law

$$\frac{d[Q]}{dt} = k[QH_2]^m[S]^n \quad (6)$$

where k is the rate constant, and m and n are the empirical orders with respect to hydroquinone and surface area, respectively. Because all reactions were completed at a buffered pH of 3.75, the proton concentration has been incorporated into the rate constant. In the reaction period studied, less than 0.5% of the total Fe^{III} was reduced, and hence there was no significant change on the particle surface area.

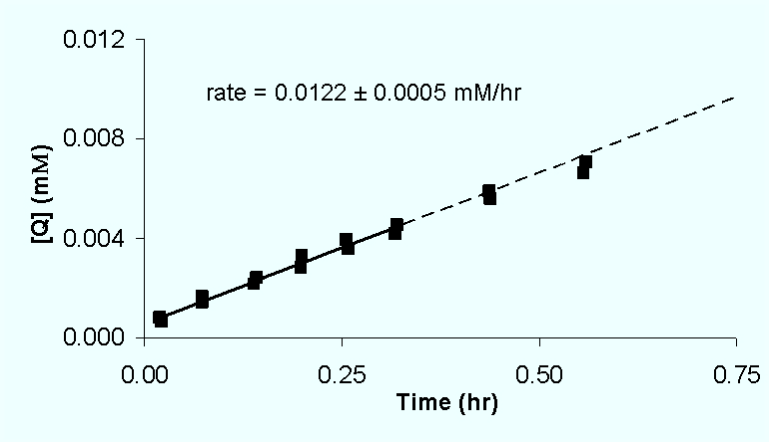

Figure 2.5 Plot of two kinetic trials at 21.0 ºC for the fresh suspension of Fh 5.0, including the slope and standard error of the linear trend (first six points from both trials). The solid line represents the linear regression using method of initial rates and the dashed line is an extension of linear data.

The reaction orders for both the fresh and dried Fh 3.6 samples were quantified and are reported in Table 2.2. Surprisingly, the empirical orders for the fresh suspensions were substantially different from those of the dried samples. With respect to hydroquinone, the rate law was first-order for the fresh suspensions and half-order for the dried samples. The order with respect to oxide surface was 0.33 for the fresh suspensions and 1.22 for the dried samples. These results suggest a change in the reaction mechanism, possibly due to aggregation upon drying.[28] The non-integer orders are difficult to interpret and are consistent with a reaction that is non-elementary. Because the ferrihydrite-hydroquinone reaction was found not to be first-order with respect to the hydroquinone and with respect to the ferrihydrite surface, the Johnson et al.[19] model was not applied.

Table 2.2 Reaction orders of hydroquinone (*m*) and surface area (*n*) and average rate constants (*k*) of fresh and dried Fh 3.6.

sample	*m*	*n*	*k*
fresh	1.04 ± 0.02	0.33 ± 0.01	9900 ± 200
dried	0.48 ± 0.06	1.22 ± 0.15	1500 ± 200

Both fresh and dried ferrihydrite samples showed an increase in mass-normalized reactivity with decreasing particle size (Figure 2.6). The reaction rates for reductive dissolution of the fresh samples ranged from 0.018 to 0.028 mM/hr and for the dried samples from 0.0078 to 0.016 mM/hr. Further treatment of the data used surface areas for comparison. Surface-area-normalized reactivity was calculated by dividing the benzoquinone concentration by the factor $[S]^n$, as in eq 6, using the appropriate calculated surface area (S) and experimental value of *n*. The resulting surface-area-normalized reactivity of the fresh suspensions and the dried powders are presented in Figure 2.7. The surface-area-normalized reaction rates of the fresh and dried samples range from 2.6 to 3.6 nM/hr and 7.7 to 8.4 nM/hr, respectively. Figure 2.7 demonstrates that when the surface area is considered, there is a modest size dependence for the fresh suspensions, while the reaction rates of the dried ferrihydrites are statistically indistinguishable. Taken together, these results imply that the reactivity simply scales with the specific surface area, which is consistent with the results of Michel et al., which show that the ferrihydrite structure varies little with size. Although the empirical rate law was not first-order with respect to the hydroquinone and surface area, the surface-area normalized reactivity concurs with the behavior described by Johnson et al.[19] As described by eq 1, the changes in reaction rates are closely

correlated to sample surface area and may be described using a surface-area-normalized rate constant.

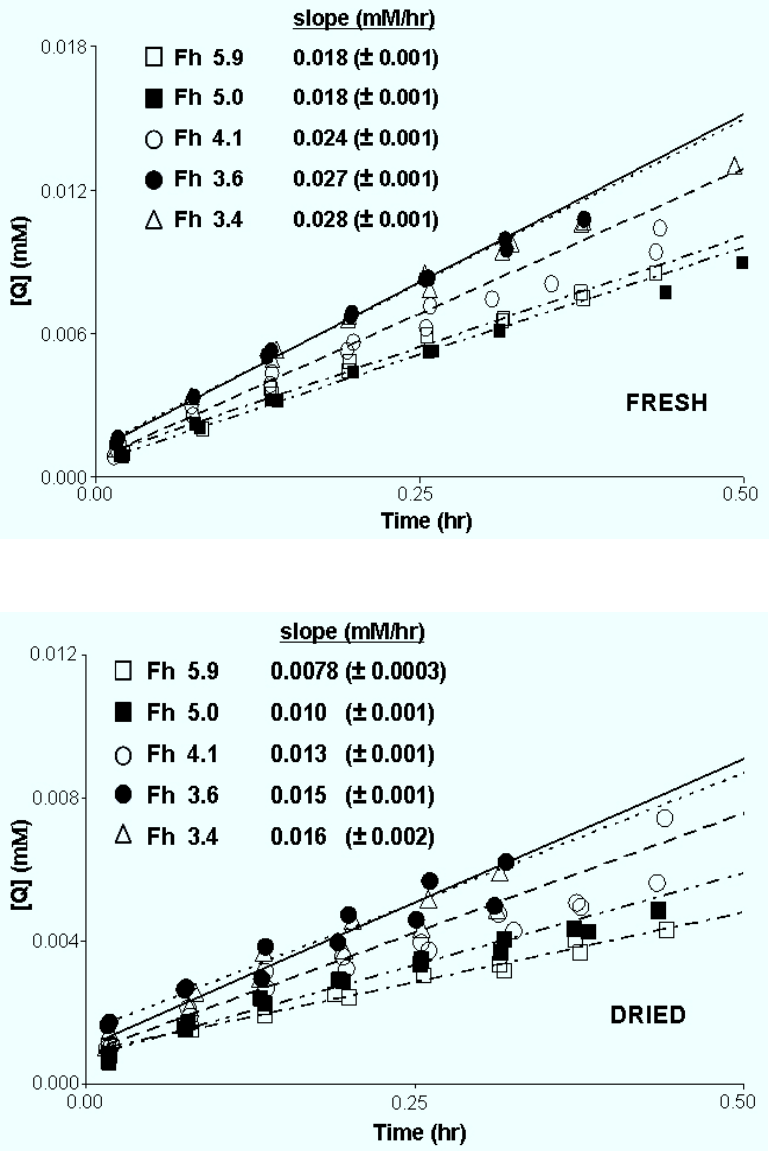

Figure 2.6 Benzoquinone concentration versus time (all samples have the same Fh mass loading, 1 g/L) for reactions of fresh suspensions and dried powders reacted at 25±1 ºC. The trendlines are extended beyond the linear data and represent Fh 5.9 (-·-·-), Fh 5.0 (-··-), Fh 4.1 (- - -), Fh 3.6 (·····), and Fh 3.4 (——). The slope and standard error (mM/hr) of each trendline are given to the right of each sample label.

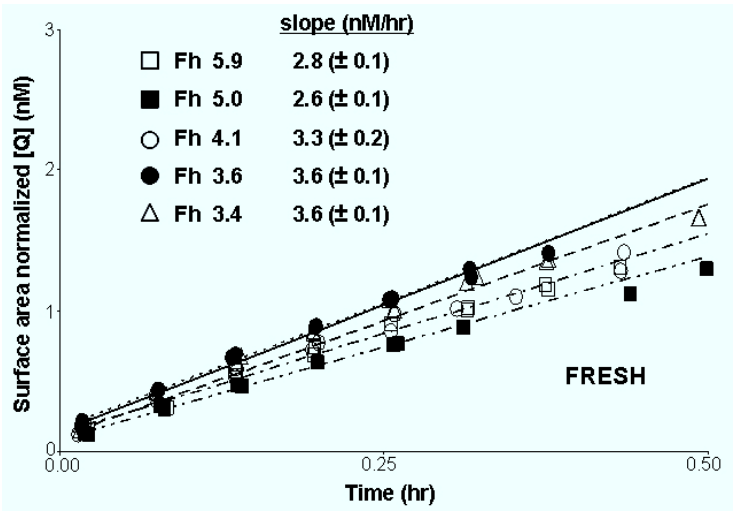

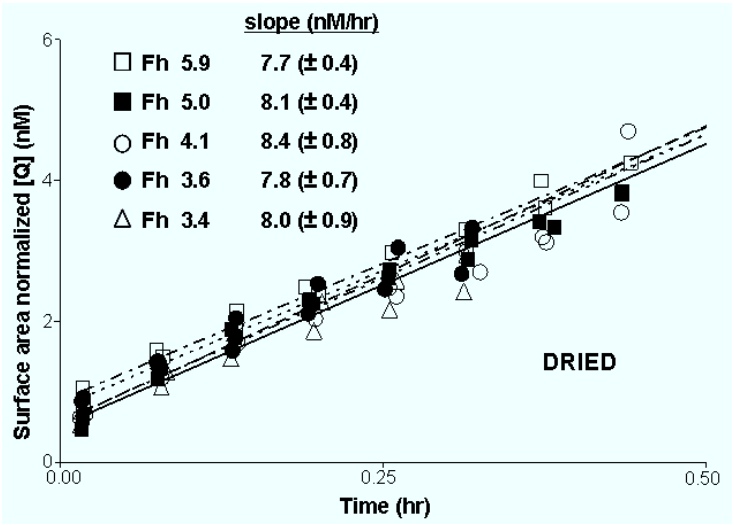

Figure 2.7 Surface-area-normalized plots, determined by dividing [Q] by the appropriate value of $[S]^n$ (see text), for reactions of fresh suspensions and dried powders reacted at 25 ±1 ºC. The trendlines are extended beyond the linear data and represent Fh 5.9 (-·-·-), Fh 5.0 (-···-), Fh 4.1 (- - -), Fh 3.6 (·····), and Fh 3.4 (——). The slope and standard error (mM/hr) of each trendline are given to the right of each sample label.

The kinetic data for each sample at five temperatures (2.0-38.0 ºC) was evaluated using the Arrhenius equation (eq 7).

$$\ln k = \ln A - \frac{E_a}{RT} \tag{7}$$

Plotting ln k against $1/T$ produced a linear trend, from which the pre-exponential factor (A) and the activation energy (E_a) were calculated.[27] To calculate rate constants, it was assumed that the reaction orders were independent of particle size and reaction temperature. Jentzsch and Penn demonstrated that there is no change in the mechanism of reductive dissolution with aluminum doping or size of ferrihydrite particles.[22] The five samples have consistent morphologies, and although benzoquinone degrades substantially above 60 ºC, there is no evidence to support a change in mechanism below that temperature.[29] Figure 2.8 shows Arrhenius plots for the dried samples. Arrhenius parameters calculated using linear regression analysis are reported with standard errors in Table 2.3. The calculated activation energies of the fresh samples, 58-62 kJ/mol, and dried samples, 49-56 kJ/mol, are similar but do not follow a size-dependent trend. The activation energies appear to decrease upon drying but can not be statistically differentiated from the fresh samples within the calculated errors.

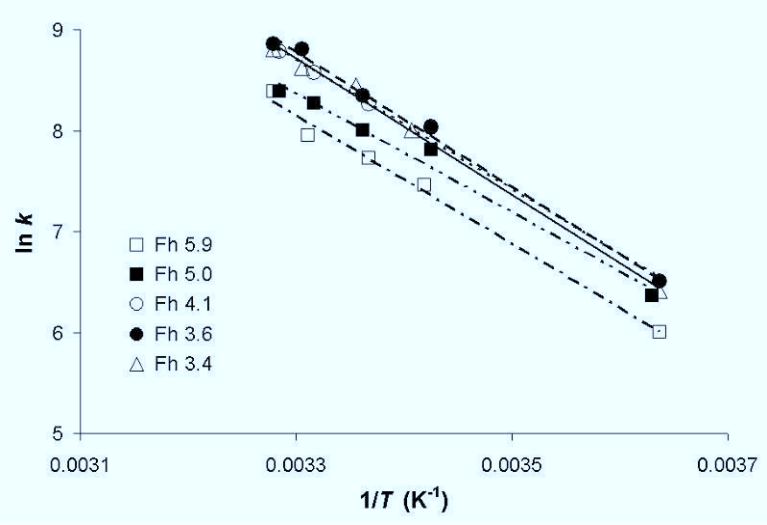

Figure 2.8 Arrhenius plot of reactions with 1 g/L oxide loading for dried ferrihydrite samples, including the trendlines representing Fh 5.9 (-·-·-), Fh 5.0 (-··-··-), Fh 4.1 (- - -), Fh 3.6 (·····), and Fh 3.4 (——).

Table 2.3 Activation energies (E_a) and pre-exponential factors (A) results by Arrhenius analysis of fresh and dried ferrihydrite samples.

	fresh		dried	
sample	E_a (kJ/mol)	A ($\bullet 10^{-14}$ hr^{-1})	E_a (kJ/mol)	A ($\bullet 10^{-14}$ hr^{-1})
Fh 3.4	61.1 ± 3.6	4.0 ± 0.2	56.2 ± 2.3	0.30 ± 0.01
Fh 3.6	57.8 ± 1.6	2.2 ± 0.1	55.8 ± 2.3	0.27 ± 0.01
Fh 4.1	58.7 ± 3.2	1.3 ± 0.5	53.5 ± 2.4	0.10 ± 0.01
Fh 5.0	61.8 ± 2.1	3.1 ± 0.1	49.2 ± 3.5	0.013 ± 0.001
Fh 5.9	57.6 ± 3.3	0.63 ± 0.03	53.0 ± 3.0	0.049 ± 0.002

The pre-exponential factor, A, significantly decreases upon drying, which is consistent with a loss of accessible surface area due to aggregation. More interesting, however, is the observation that A significantly increases with decreasing size. In fact, the six-fold increase in A, observed for both the fresh suspensions (0.63-4.0 $\cdot 10^{14}$) and dried powders (0.049-0.30 $\cdot 10^{14}$), substantially outpaces the increase in specific surface area, which doubles when comparing Fh 3.4 and Fh 5.9. Zhang et al. observed that the pre-exponential factor for the phase transformation of dried nanocrystalline TiO_2 increased substantially with decreasing particle size,[30] but we are not aware of studies of aqueous reactions of nanoparticles that have observed similar trends. The magnitude of the increase in A is similar for the fresh suspensions and dried samples, suggesting that a fundamental size effect—independent of aggregation—is observed. Because no significant size-dependent changes are observed in E_a or in the X-ray spectra, it is unlikely that this effect is related to intrinsic materials properties of the nanoparticles, such as distortions in surface structure. Instead, we propose that the change A is related to the ordering of water at the nanoparticle surface. Molecular simulations[31] and surface sensitive experiments[32] have demonstrated that interactions between metal oxide surfaces and water molecules lead to the development of structured hydration layers that

can impose a barrier for the diffusion of ions to the mineral surface. Moreover, simulations of water at the surface of bulk and nanoscale calcite indicate that the ordering effect, indicated by water residence times in the first hydration layer, decreases with decreasing particle size.[31] Thus, the hypothesis that the diffusion of species through surface water limits the rate of interfacial reaction is consistent with our observation of increased pre-exponential factor for smaller ferrihydrite nanoparticles.

2.5 Conclusions

Results of this work show that the rate of reductive dissolution of six-line ferrihydrite is closely proportional to specific surface area, with no discernable size dependence for the activation energy of the reductive dissolution or the electronic structure of ferrihydrite. Surprising differences in reaction orders with respect to the ferrihydrite loading and the reductant were observed for the dried samples as compared to the fresh suspensions. However the pre-exponential factor, which is related to the frequency of reagent-surface encounters, increased six-fold when comparing the 3.4 and 5.9 nm ferrihydrite samples, a result that was consistent for both dried powders and fresh suspensions. This substantially outpaces the two-fold increase in specific surface area for the same samples. One hypothesis to explain the changes in reaction order and pre-exponential factor is that the structure of water, and hence the rate of reagent diffusion to the nanoparticle surface, is size dependent.

2.6 Acknowledgement

This work was supported by the IGERT Program of the National Science Foundation under award Number DGE-0114372 (fellowship to J.J.E.), the University of Minnesota,

the National Science Foundation Career Grant 0346385, and the Department of Energy (DOE) Office of Basic Energy Sciences (BES). We thank Sandeep Kumar and Tracy Davis for SAXS data collection and analysis, and we thank David Sherman for insightful discussions. Oxygen X-ray absorption spectroscopy was performed at beamline 7.0 at the Advanced Light Source (ALS), and we thank Jinghua Guo. The ALS is supported by the DOE BES, Division of Materials Sciences under Contract No. DE-AC02-05CH11231. TEM characterization was carried out at the Characterization Facility, University of Minnesota, which receives support from NSF through the National Nanotechnology Infrastructure Network.

2.7 References

1. Cornell, R. M.; Schwertmann, U., *The Iron Oxides: Structure, Properties, Reactions, Occurrences and Uses*. 2nd ed.; Wiley-VCH: Weinheim, 2003.

2. Ford, R. G.; Bertsch, P. M.; Farley, K. J. Changes in transition and heavy metal partitioning during hydrous iron oxide aging. *Environmental Science and Technology* **1997** 31, 2028.

3. Chun, C. L.; Penn, R. L.; Arnold, W. A. Kinetic and microscopic studies of reductive transformations of organic contaminants on goethite. *Environmental Science and Technology* **2006** 40, 3299.

4. Stipp, S. L. S.; Hansen, M.; Kiristensen, R.; Hochella, M. F., Jr.; Bennedsen, L.; Dideriksen, K.; Balic-Zunic, T.; Leonard, D.; Mathieu, H.-J. Behaviour of Fe-oxides relevant to contaminant uptake in the environment. *Chemical Geology* **2002** 190, 321.

5. Straub, K. L.; Benz, M.; Schink, B. Iron metabolsim in anoxic environments at near neutral pH. *FEMS Microbiology Ecology* **2001** 34, 181.

6. LaKind, J. S.; Stone, A. T. Reductive dissolution of goethite by phenolic reductants. *Geochimica et Cosmochimica Acta* **1989** 53 (5), 961.

7. Scott, D. T.; McKnight, D. M.; Blunt-Harris, E. L.; Kolesar, S. E.; Lovley, D. R. Quinone moieties act as electron acceptors in the reduction of humic substances by humics-reducing microorganisms. *Environmental Science and Technology* **1998** 32, 2984.

8. Pederson, H. D.; Postma, D.; Jakobsen, R. Release of arsenic associated with the reduction and transformation of iron oxides. *Geochimica et Cosmochimica Acta* **2006** 70, 4116.

9. Michel, F. M.; Ehm, L.; Antao, S. M.; Lee, P. L.; Chupas, P. J.; Liu, G.; Strongin, D. R.; Schoonen, M. A. A.; Phillips, B. L.; Parise, J. B. The structure of ferrihydrite, a nanocrystalline material. *Science* **2007** 316, 1726.

10. Kung, K.-H.; McBride, M. B. Electron transfer processes between hydroquinone and iron oxides. *Clays and Clay Minerals* **1988** 36 (4), 303.

11. Banfield, J. F.; Zhang, H., Nanoparticles in the Environment. In *Nanoparticles and the Environment*, 1st ed.; Banfield, J. F.; Navrotsky, A., The Mineralogical Society of America: Washington, DC, 2001; 44.

12. Hochella, M. F., Jr. Nanoscience and technology: The next revolution in the Earth sciences. *Earth and Planetary Science Letters* **2002** 203, 593.

13. Waychunas, G. A.; Kim, C. S.; Banfield, J. F. Nanoparticulate iron oxide minerals in soils and sediments: unique properties and contaminant scavenging mechanisms. *Journal of Nanoparticle Research* **2005** 7, 409.

14. Anschutz, A. J.; Penn, R. L. Reduction of crystalline iron(III) oxyhydroxides using hydroquinone: Influence of phase and particle size. *Geochemical Transactions* **2005** 6 (3), 60.

15. Madden, A. S.; Hochella, M. F., Jr. A test of geochemical reactivity as a function of mineral size: Manganese oxidation promoted by hematite nanoparticles. *Geochimica et Cosmochimica Acta* **2005** 69 (2), 389.

16. Madden, A. S.; Hochella, M. F., Jr.; Luxton, T. P. Insights for size-dependent reactivity of hematite nanomineral surfaces through Cu^{2+} sorption. *Geochimica et Cosmochimica Acta* **2006** 70, 4095.

17. Villalobos, M.; Trotz, M. A.; Leckie, J. O. Variability in goethite surface site density: evidence from proton and carbonate sorption. *Journal of Colloid and Interface Science* **2003** 268, 273.

18. Boily, J.-F.; Persson, P.; Sjoberg, S. Benzenecarboxylate surface complexation at the goethite (α-FeOOH)/water interface. *Journal of Colloid and Interface Science* **2000** 227, 132.

19. Johnson, T. L.; Scherer, M. M.; Tratnyek, P. G. Kinetics of halogenated organic compound degradation by iron metal. *Environmental Science and Technology* **1996** 30, 2634.

20. Liou, Y. H.; Lo, S. L.; Lin, C. J. Size effect in reactivity of copper nanoparticles to carbon tetrachloride degradation. *Water Research* **2007** 41, 1705.

21. Penn, R. L.; Erbs, J. J.; Gulliver, D. M. Controlled growth of alpha-FeOOH nanorods by exploiting-oriented aggregation. *Journal of Crystal Growth* **2006** 293, 1.

22. Jentzsch, T. L.; Penn, R. L. Influence of aluminum doping on ferrihydrite nanoparticle reactivity. *Journal of Physical Chemistry B* **2006** 110, 11746.

23. Kumar, S.; Davis, T. M.; Ramanan, H.; Penn, R. L.; Tsapatsis, M. Aggregative growth of silicalite-1. *Journal of Physical Chemistry B* **2007** 111 (13), 3398.

24. Gilbert, B.; Lu, G.; Kim, C. S. Stable cluster formation in aqueous suspensions of iron oxyhydroxide nanoparticles. *Journal of Colloid and Interface Science* **2007** 313 (1), 152.

25. Sherman, D. M. Electronic structures of iron (III) and manganese(IV) (hyro)oxide minerals: Thermodynamics of photochemical reductive dissolution in aquatic environments. *Geochimica et Cosmochimica Acta* **2005** 69 (13), 3249.

26. Stack, A. G.; Eggleston, C. M.; Engelhard, M. H. Reaction of hydroquinone with hematite I. Study of adsorption by electrochemical-scanning tunneling microscopy and X-ray photoelectron spectroscopy. *Journal of Colloid and Interface Science* **2004** 274, 433.

27. Espenson, J. H., *Chemical Kinetics and Reaction Mechanisms*. 2nd ed.; McGraw-Hill: New York, 2002.

28. Hofmann, A.; Pelletier, M.; Michot, L.; Stradner, A.; Schurtenberger, P.; Kretzschmar, R. Characterization of the pores in hydrous ferric oxide aggregates

formed by freezing and thawing. *Journal of Colloid and Interface Science* **2004** 271, 163.

29. Anschutz, A. J. Reactivity of iron oxyhydroxide nanoparticles: Effects of physical variables. Doctor of Philosophy, University of Minnesota, Minneapolis, MN, 2006.

30. Zhang, H.; Banfield, J. F. Size dependence of the kinetic rate constant for phase transformation in TiO_2 nanoparticles. *Chemistry of Materials* **2005** 17 (13), 3421.

31. Kerisit, S.; Cooke, D. J.; Spagnoli, D.; Parker, S. C. Molecular dynamics simulations of the interactions between water and inorganic solids. *Journal of Materials Chemistry* **2005** 15, 1454.

32. Zhang, Z.; Fenter, P.; Cheng, L.; Sturchio, N. C.; Bedzyk, M. J.; Predota, M.; Bandura, A.; Kubicki, J. D.; Lvov, S. N.; Cummings, P. T.; Chialvo, A. A.; Ridley, M. K.; Benezeth, P.; Anovitz, L.; Palmer, D. A.; Machesky, M. L.; Wesolowski, D. J. Ion adsorption at the rutile--water interface: Linking molecular and macroscopic properties. *Langmuir* **2004** 20, 4954.

Chapter 3

Kinetics of Goethite Nanocrystal Growth by Oriented Aggregation*

* Reprinted from:
Journal of Crystal Growth 293, Penn, R. L.; Erbs, J. J.; Gulliver, D. M., "Controlled growth of alpha-FeOOH nanorods by exploiting-oriented aggregation," 1-4, Copyright 2006, with permission from Elsevier
Journal of Crystal Growth 309, Penn, R. L.; Tanaka, K.; Erbs, J., "Size dependent kinetics of oriented aggregation," 97-102, Copyright 2007, with permission from Elsevier

3.1 Chapter Summary

Oriented aggregation is an important, non-classical crystal growth mechanism by which nanocrystals grow, unique morphologies are produced, and defects are incorporated into initially defect-free nanocrystals. First, we demonstrate particle size control in the preparation of ferrihydrite nanoparticles by forced hydrolysis from solution. Then, we demonstrate particle size control in the growth of goethite nanorods by exploiting oriented aggregation using the size-controlled ferrihydrites as the precursor nanoparticles. Specifically, it is shown that the size of goethite nanocrystals formed depends directly on the size of the precursor ferrihydrite nanoparticles. Finally,

the kinetics of oriented aggregation as a function of precursor nanoparticle size were quantified. Results demonstrate a dramatic size effect with rate constants increasing with decreasing size.

3.2 Introduction

Growth by oriented aggregation is an important, non-classical nanocrystal growth mechanism in a wide range of natural and synthetic materials, including zeolites and iron oxides.[1-12] It has been shown that coarsening alone does not adequately describe the kinetics of particle growth for many systems[13,14] but the inclusion of an aggregative step leads to improved kinetic models.[2,14-16] Aggregation-based mechanisms of crystal growth may provide a sophisticated method of influencing and controlling particle size, morphology, and microstructure.[17-19] Oriented aggregation is a unique type of aggregation in which secondary crystals composed of oriented subunits are produced. After primary nanoparticles have nucleated, they may undergo structural and/or chemical evolution prior to growth by oriented aggregation.[2,20] Once nuclei have the capacity to grow by oriented aggregation, the primary particles form complexes analogous to outer-sphere complexes and can either dissociate or convert to secondary crystallites once a favorable orientation has been achieved.[17]

Goethite (α-FeOOH) is an antiferromagnetic iron oxyhydroxide that can be synthesized by aging ferrihydrite ($Fe_5HO_8 \bullet 4H_2O$) nanoparticles in aqueous suspension. Proposed mechanisms range from the dissolution of the precursor nanoparticles followed by reprecipitation[21] to oriented aggregation preceded by phase transformation.[18] Goethite and ferrihydrite are ubiquitous at and near the Earth's surface and may dominate the reactive, accessible surface area in soils and sediments.[22] Natural

goethite and ferrihydrite may form spherical particles with 3-10 nm.[23] Natural and synthetic goethite may also form acicular, submicron particles aggregated into bundles or rafts. Acicular magnetic particles suitable for magnetic recording media can be produced from the transformation from goethite nanoparticles iron oxide pseudomorph nanoparticles.[24,25] Ideally, precursor goethite nanoparticles for use in oriented magnetic recording tape should be unaggregated and monodisperse.

Here, we present results that indicate the average size of goethite crystals and the rate of growth by oriented aggregation depend directly on the average size of the precursor ferrihydrite particles. Control over both the size of ferrihydrite nanoparticles and goethite nanoparticles formed by oriented aggregation is demonstrated. The final nanoparticles are relatively monodisperse and unaggregated and may be ideal for preparation of acicular magnetic nanoparticles via chemical reduction. Then, for three samples of synthetic ferrihydrite of varying sizes, the rates of conversion of ferrihydrite nanoparticles to goethite nanoparticles were quantified. The molecular model presented by Penn[17] was employed to describe goethite growth from ferrihydrite precursor nanoparticles. The primary nanoparticles are treated as molecules,[26] designated as "P" in eq 1, in the three-step kinetic model. The particle-particle complex, P···P, can form, dissociate, or react (eqs 1-3) to form an oriented aggregate, P–P.

$$\mathrm{P} + \mathrm{P} \longrightarrow \mathrm{P}\cdots\mathrm{P} \quad k_1 \tag{1}$$

$$\mathrm{P}\cdots\mathrm{P} \longrightarrow \mathrm{P} + \mathrm{P} \quad k_{-1} \tag{2}$$

$$\mathrm{P}\cdots\mathrm{P} \xrightarrow{-x\mathrm{H_2O}} \mathrm{P}-\mathrm{P} \quad k_2 \tag{3}$$

P···P can be viewed as an outer-sphere complex, in which the primary particles are able to rotate into orientations that result in structural accord at the interface. Adsorbed solvent species (e.g., water molecules, hydroxyls, protons in the case of aqueous suspensions) and other species are irreversibly removed from the interface (denoted by -xH$_2$O in eq 3) or incorporated into the bulk to produce an oriented aggregate. Applying a rapid equilibrium assumption for the concentration of P···P complexes to the oriented aggregation mechanism (eqs 1-3) yields a rate law that is second order with respect to the primary nanoparticle concentration (eq 4):

$$\frac{d[\mathrm{P-P}]}{dt} = \frac{k_1 k_2}{k_{-1}}[\mathrm{P}]^2 \qquad (4)$$

Using transmission electron microscopy (TEM) images, the rate of conversion from primary nanoparticles to goethite nanorods was quantified in the early stages of growth (less than 1% goethite yield by number), and the rate constants demonstrate a dramatic increase in growth by oriented aggregation with decreasing precursor nanoparticle size.

3.3 Experimental Methods

Ferrihydrite suspensions were prepared by the controlled addition of a 0.48 M $NaHCO_3$ solution to an equal volume of 0.40 M $Fe(NO_3)_3$•$9H_2O$ with vigorous stirring via peristaltic pump (11 minute delivery) at a specified temperature ranging from 5 to 85 ºC. The suspension was immediately brought to room temperature, then microwave-annealed for 30-second intervals until just boiling, and finally plunged into an ice bath. Post-annealed suspensions were dialyzed against purified water (Millipore®) three days with 3-4 water changes per day. For the size-controlled oriented aggregation experiment, the dialyzed suspensions were adjusted to pH 12 using a sodium hydroxide

solution, and the resulting suspensions were aged at 90 ºC for 72 hours. Finally, the aged suspensions were dialyzed against purified water for three days with 3-4 water changes per day. For the oriented aggregation growth kinetics study, the pH of the dialyzed suspension was adjusted to 4, and the resulting suspensions were aged at 80 ºC with samples extracted periodically for characterization.

3.3.1 *X-Ray Diffraction*

Samples were characterized before aging by powder X-ray diffraction (XRD) in order to check for purity. Dried samples were characterized using a PANalytical X-Pert PRO MPD theta-theta diffractometer equipped with a cobalt anode and an X-Celerator detector. The diffraction patterns were compared to the reference powder diffraction files (PDF) for six-line ferrihydrite (#29-0713) and other iron oxides such as goethite (#29-0712) and hematite (#33-0664).

3.3.2 *Transmission Electron Microscopy*

Samples were prepared for TEM within 24 hours of sampling. A small amount of each sample was diluted in Milli-Q water (Millipore®). A single drop of the suspension was drop cast on a 3 mm copper TEM grid coated with holey carbon film (Structure Probe, Inc.). Images were collected using an FEI Tecnai T12 microscope or an FEI Technai F30 microscope equipped with a Gatan charge-coupled device (CCD) camera.

3.3.3 *Particle Sizing and Particle Counting Methods*

Particle sizes were measured using calibrated TEM images and Gatan Digital Micrograph (version 3.3.8) software. In the case of ferrihydrite particle sizes, the

number of particles measured is listed in Tables 3.1 and 3.2. In the case of goethite particles, all observed goethite particles were measured.

For the oriented aggregation growth study, particles were manually classified as primary particles (ferrihydrite dots) or as acicular oriented aggregates (goethite rods) based on size and aspect ratio in order to quantify the number of each type of particle as a function of aging time. In all cases, these measurements were performed using samples collected at the very early stage of goethite production with less than 1% conversion from dots to rods, by number. Unfortunately, automated particle analysis was not possible due to the relatively low contrast between the 4-7 nm ferrihydrite particles and the holey carbon film. In addition, the number of dots imaged typically numbered in the tens of thousands. To make data analysis manageable, each image was split into quandrants and the number of dots estimated based on a minimum of four manual quadrant-counts from images with varying particle densities. A quadrant-count was achieved by opening the image file in Adobe Photoshop®, creating a new layer, and manually drawing a dot or line for each particle observed using the paint tool within the new layer. The new layer was saved as a binary image and opened using NIH Image (a public domain image processing and analysis program for Macintosh), which automatically counted the dots and lines. Estimates were periodically tested for accuracy by comparing the estimated and actual dots in an image quadrant.

3.4 Results and Discussion

3.4.1 *Size-Controlled Oriented Aggregation*

For the first time, ferrihydrite size control has been demonstrated. The size control is achieved by controlling the temperature during the hydrolysis step. Figure 3.1

shows TEM images of two ferrihydrite samples (prepared at 5 and 70 ºC) and histograms of particle lengths for the four ferrihydrite samples (prepared at 5, 25, 50, and 70 ºC), and Table 3.1 presents a summary of the particle size data. Using a *t*-test to assess whether or not the means reported in Table 3.1 represent statistically different quantities yields a probability of less than 10^{-22} (using the Fh 25 and Fh 50 data sets) that these means represent statistically indistinguishable values. Other properties, like aspect ratio and phase, do not change with the increase in hydrolysis temperature. X-ray diffraction patterns (Figure 3.2) confirm the identification of these samples as six-line ferrihydrite, with no evidence for the formation of other iron oxides. High-resolution TEM images demonstrate that particles are not aggregated and uniform in shape.

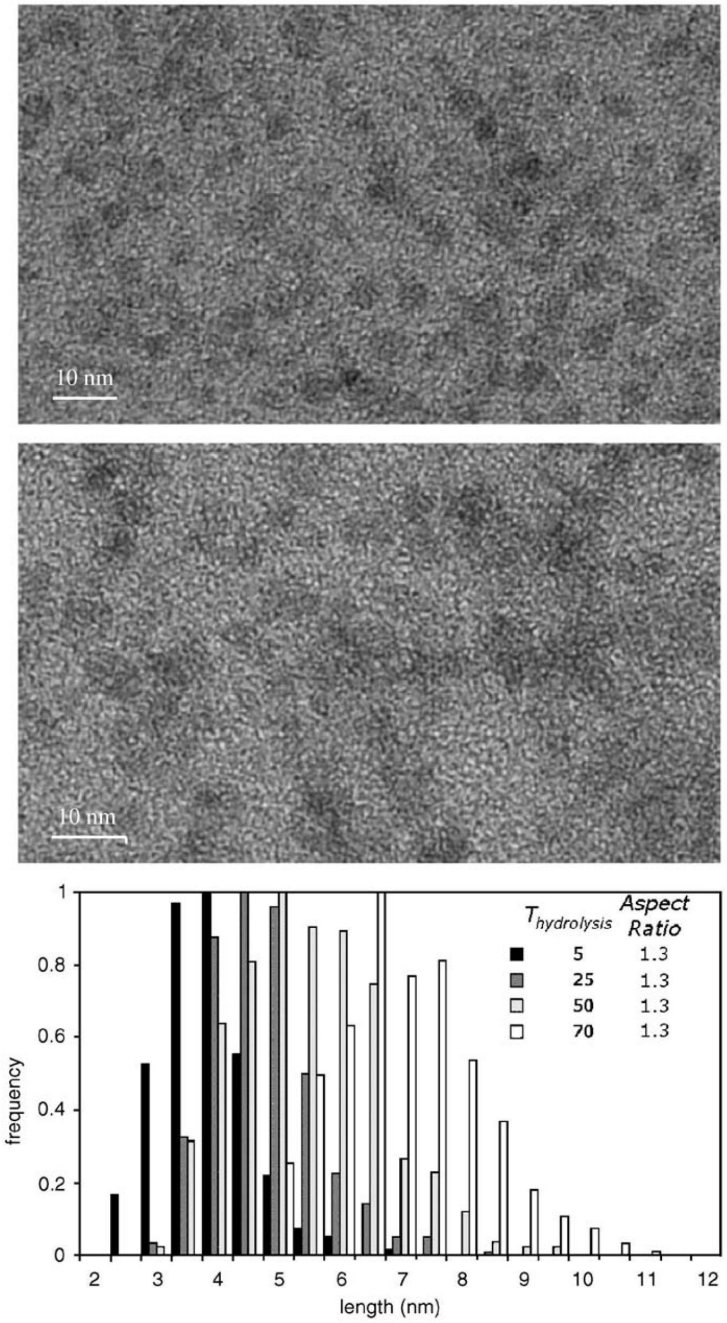

Figure 3.1 TEM images of ferrihydrite nanoparticles produced by hydrolysis of 5 ºC (upper) and 70 ºC (middle). The lower graph presents data from particle size measurements of ferrihydrite particle lengths obtained from calibrated TEM images.

Table 3.1 Summary of ferrihydrite and goethite particle size data.*

Sample	Avg. length (nm)	Avg. width (nm)	Aspect ratio	$V^{Gt}_{avg}/V^{Fh}_{avg}$
Fh 5 (496)	3.8	3.1	1.3	—
Fh 25 (519)	4.7	3.6	1.3	—
Fh 50 (511)	5.4	4.1	1.3	—
Fh 70 (542)	6.8	5.5	1.3	—
Gt 5 (564)	90	10	9.6	147
Gt 25 (500)	111	11	11	131
Gt 50 (390)	118	12	10	117
Gt 70 (372)	152	14	12	132

* Sample labels identify the phase (Fh = ferrihydrite; Gt = goethite) and hydrolysis temperature at which the precursor ferrihydrite particles were prepared. Numbers in parentheses indicate the number of particles measured from TEM images. Right-hand column is the average volume of the goethite crystals divided by the average volume of a single ferrihydrite particle as determined from particle size measurements obtained from TEM images.

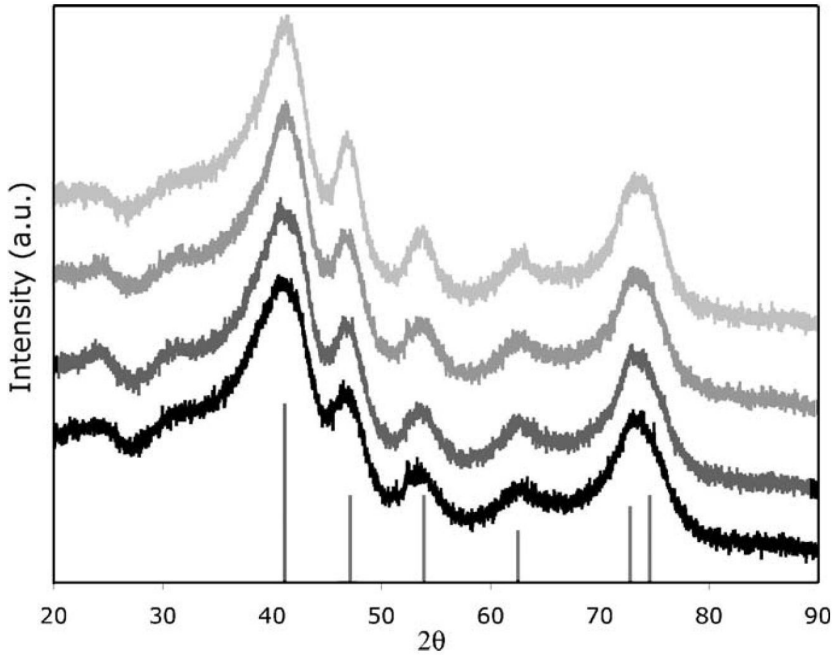

Figure 3.2 X-ray diffraction patterns for ferrihydrite nanoparticles synthesized by hydrolysis at 5 (lowest), 25, 50, and 70 (highest) ºC. For comparison, the powder diffraction file for six-line ferrihydrite is shown as a stick pattern at the bottom.

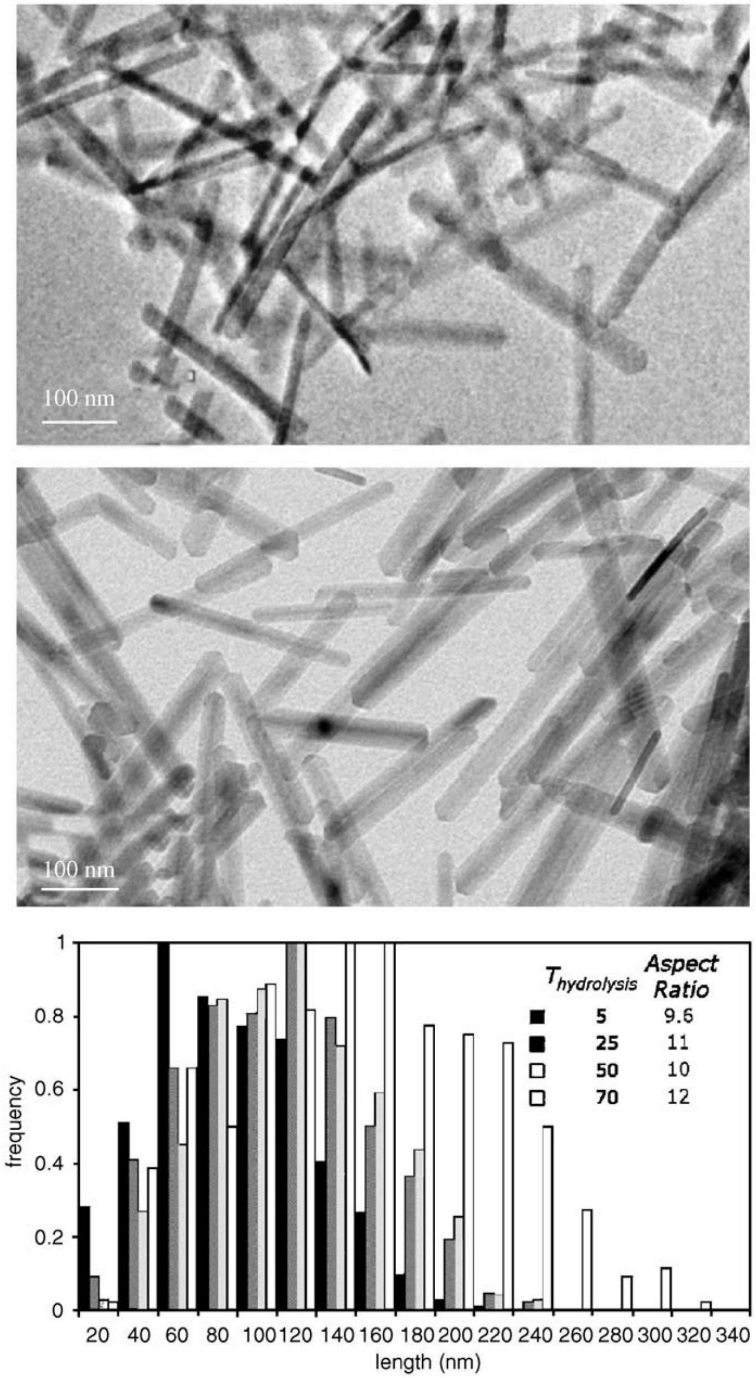

Figure 3.3 TEM images of goethite nanoparticles prepared from the 5 ºC (upper) and 70 ºC (middle) ferrihydrite samples shown in Figure 3.1. The lower graph represents data from particle size measurements of goethite particle lengths obtained from calibrated TEM images.

The size of goethite nanorods prepared by the aging of ferrihydrite suspensions depends directly on the precursor (ferrihydrite) particle size. Figure 3.3 shows two representative TEM images of goethite particles produced from ferrihydrite samples prepared at 5 ºC (upper) and 70 ºC (lower). XRD (Figure 3.4) and TEM characterization demonstrate complete conversion of ferrihydrite to goethite. Table 3.1 includes a summary of the goethite particle size data, and Figure 3.3 (bottom) shows the histograms of the 5, 25, 50, and 70 ºC goethite nanoparticle lengths.

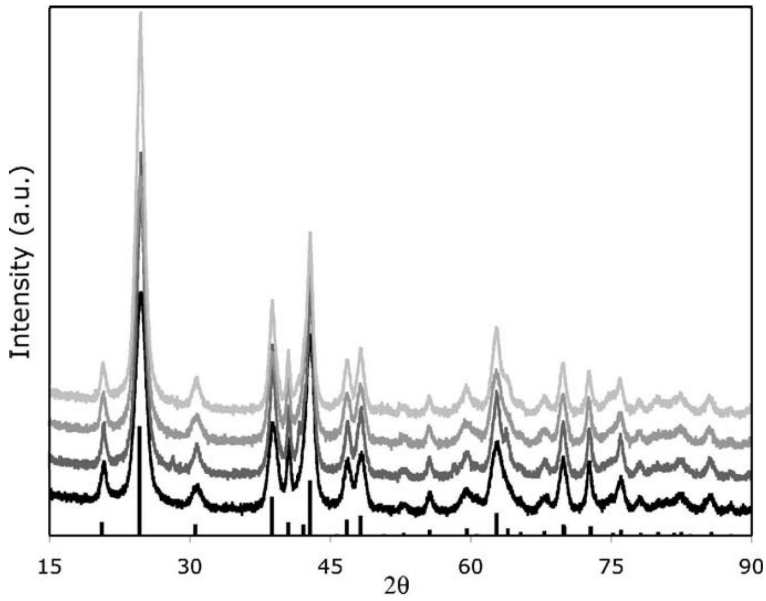

Figure 3.4 X-ray diffraction patterns for goethite nanoparticles prepared from the 5 (lowest), 25, 50, and 70 (highest) ºC ferrihydrite samples highlighted in Figure 3.2. For comparison, the powder diffraction file for goethite is shown as a stick pattern at the bottom.

Previous results have demonstrated that the goethite nanorods form by phase transformation of the ferrihydrite precursor nanoparticles to goethite followed by oriented aggregation to form the nanorods.[18] Interestingly, dividing the average volume of the goethite particles (using the particle size measurements from TEM images and

the known crystallography of goethite) by the average volume of a single ferrihydrite particle suggests that the number of primary particles per goethite crystallite is approximately constant and independent of primary particle size. This suggests that size control through oriented aggregation can be achieved by simply controlling primary particle size. However, a challenge remains in regards to controlling the number of precursor nanoparticles per product nanorod.

3.4.2 *Kinetics of Oriented Aggregation*

The rate of growth by oriented aggregation is strongly size dependent. As the size of primary particles increases, the rate of goethite nanorod production decreases dramatically. TEM images and histogram size plots for the ferrihydrite samples were similar to those presented in the size-controlled oriented aggregation results section above. Table 3.2 presents a summary of the particle size data for ferrihydrite nanoparticles prepared using hydrolysis temperatures of 5, 45, and 85 ºC. Using a *t*-test of the means reported in Table 3.2 yields a probability of less than 10^{-33} (comparing the Fh 5 and Fh 45 data sets) that these means represent statistically indistinguishable values.

Table 3.2 Summary of ferrihydrite particle size data.*

Sample	Average length (nm)	Average width (nm)	$(k_1/k_{-1})k_2$
Fh 5 (530)	4.9	3.7	2.4×10^{-18}
Fh 45 (515)	6.1	4.5	2.4×10^{-19}
Fh 85 (516)	7.3	5.3	9.0×10^{-21}

* Fh sample labels (Fh #) identify the hydrolysis temperature at which precursor Fh particles were prepared. Numbers in parentheses indicate the number of particles

measured from calibrated TEM images. Finally, $(k_1/k_{-1})k_2$ is the growth rate constant, in units of mL/(#P*h), as determined from the slope of the linear least squares line fit to the inverse number concentration of primary particles versus time data.

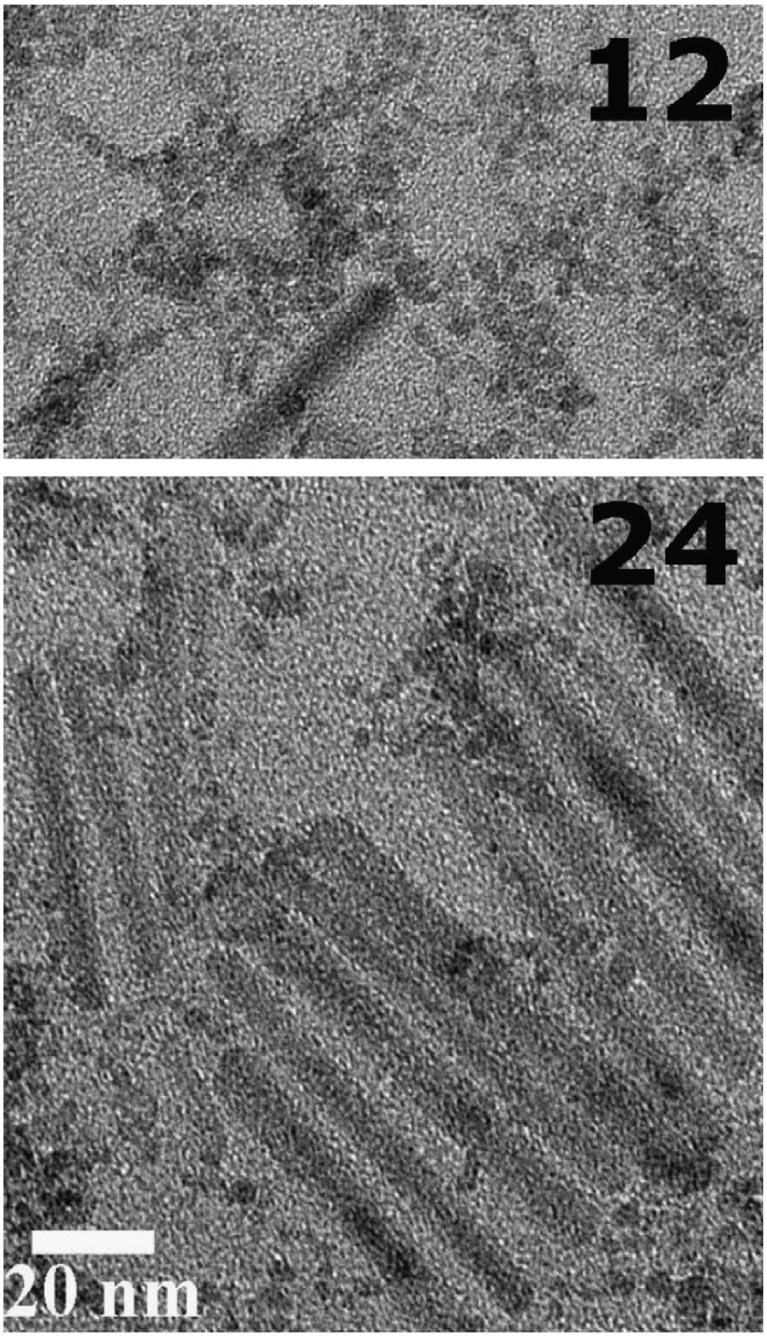

Figure 3.5 Two representative TEM micrographs of Fh 5 aged for 12 (upper) and 24 (lower) hours at 90 ºC.

The kinetics of growth by oriented aggregation is consistent with the second-order rate law discussed above in eq 4. Using the average particle volume of the as-prepared ferrihydrite nanoparticles and the concentration of the ferric ion source, a number concentration of ferrihydrite nanoparticles was calculated. Then, the drop in number concentration as a function of time was calculated by determining the number ratio of goethite nanorods to ferrihydrite nanoparticles from TEM images and using the average volume of the goethite nanorods. Figure 3.5 presents representative TEM images of Fh 5 aged for 12 hours (upper) and 24 hours (lower), and Figure 3.6 shows Fh 85 aged for 120 hours. Plotting the inverse of the number concentration of ferrihydrite nanoparticles (1/P) versus time gives a straight line with a slope equal to the rate constant for growth by oriented aggregation, $k_1 \cdot k_2 / k_{-1}$ from eq 4. Figure 3.7 presents plots of 1/P versus time for the Fh 5 (upper), Fh 45 (middle), and Fh 85 (lower) samples. These data clearly show that growth by oriented aggregation is strongly size dependent, with an order of magnitude increase in rate constant with each nanometer decrease in nanoparticle length.

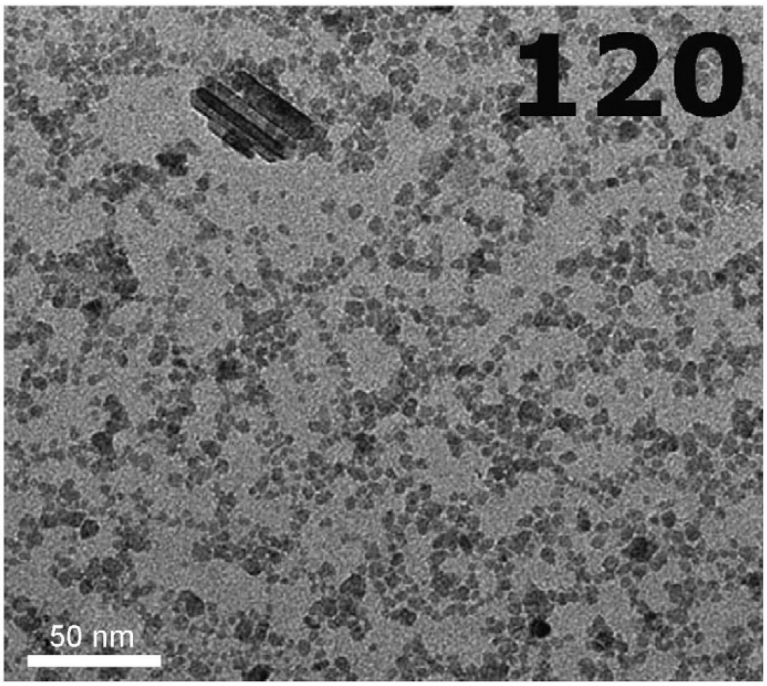

Figure 3.6 A representative TEM micrograph of Fh 85 aged for 120 h at 90 ºC.

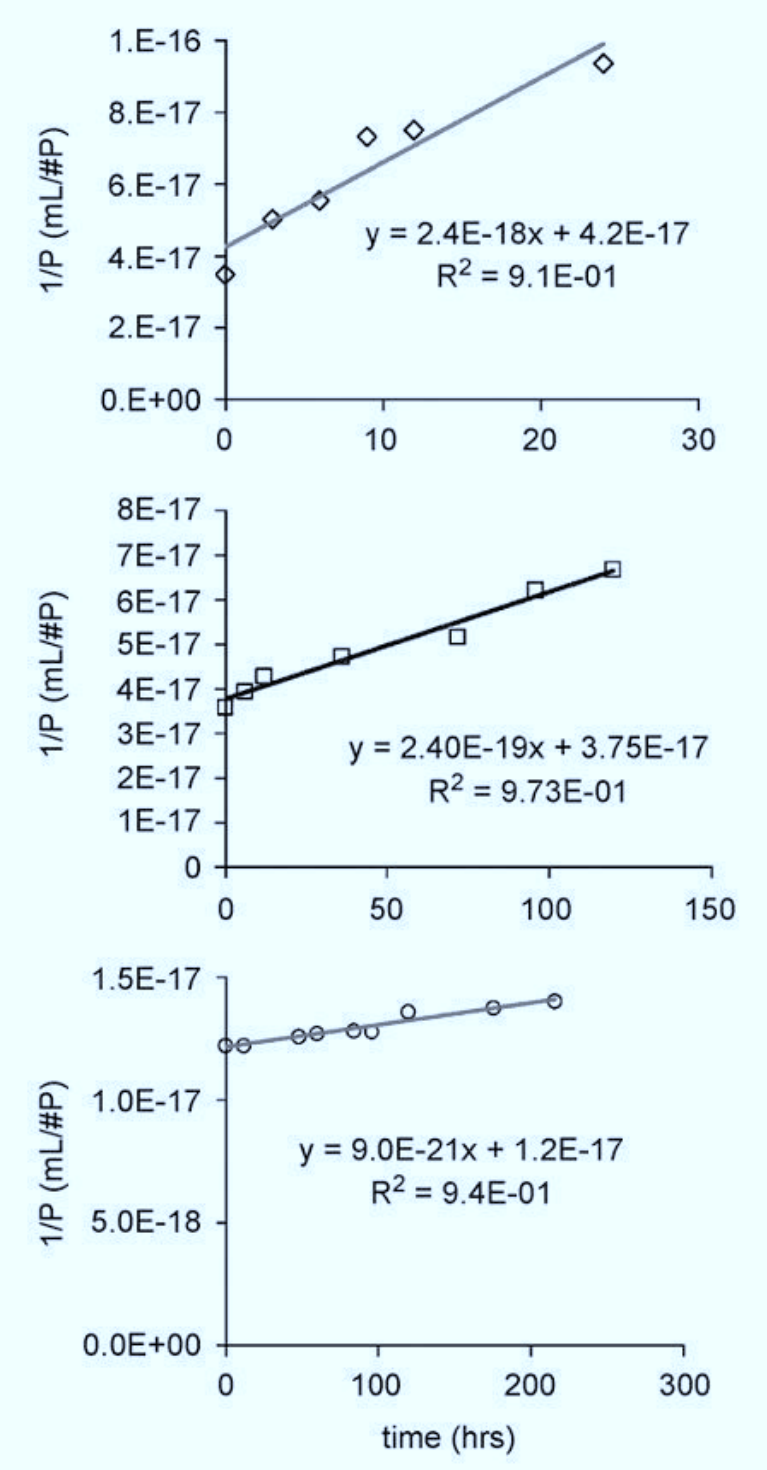

Figure 3.7 Plots showing the inverse number concentration of primary particles versus time (in h) for Fh 5 (upper), Fh 45 (middle), and Fh 85 (lower).

As a first approach to better understand the size dependence of growth by oriented aggregation, a particle-particle coalescence rate constant was calculated following the approach presented by Hyning et al.[27] This approach is based on DLVO (Derjaguin, Landau, Verwey, and Overbeek) interactions.[28-30] Equation 5 shows the expression for calculating the particle-particle coalescence rate constant rate constant (β_{ij}), in which W_{ij} (eq 6) is the stability ratio for a dimer of particle *i* and particle *j*.

$$\beta_{ij} = \frac{2kT}{3\mu}(r_i + r_j)\left(\frac{1}{r_i} + \frac{1}{r_j}\right)\frac{1}{W_{ij}} \tag{5}$$

$$W_{ij} = (r_i + r_j)\int_{(r_i+r_j)}^{\infty}\left(\frac{\exp(V_{ij}(R)/kT)}{R^2 G(R)}\right)dR \tag{6}$$

In this work, the particle-particle coalescence rate constant is calculated for two particles of the same size (β_{ii}). Using an ionic strength of 0.01 M, a separation distance of 0.5 nm, a Hamaker constant[31] of 5×10^{-20} J, a temperature of 80 ºC (mid-range for many oxide nanoparticle synthesis procedures and the aging temperature employed in this study), and a unitless dielectric constant (ε_r) for water[32] at 80 ºC of 60.86, the particle-particle coalescence rate constant was calculated as a function of both size and surface potential (Figure 3.8). As expected, as the surface potential increases, the coalescence rate (β_{ii}) decreases. This is consistent with experimental results showing that particles grow more slowly by oriented aggregation when suspension conditions are such that the particles are highly charged (i.e., several pH units away from the pH_{pzc}).[18,26] In addition, the trend of slower coalescence as a function of increasing particle size is consistent with the experimental results presented here. Figure 3.9 shows the experimental rate of growth by oriented aggregation, in units matching those of

Figure 3.8, as a function of size, and the linear trend is clear. However, the magnitude of the experimental rate constants is many orders of magnitude slower than those presented in Figure 3.8.

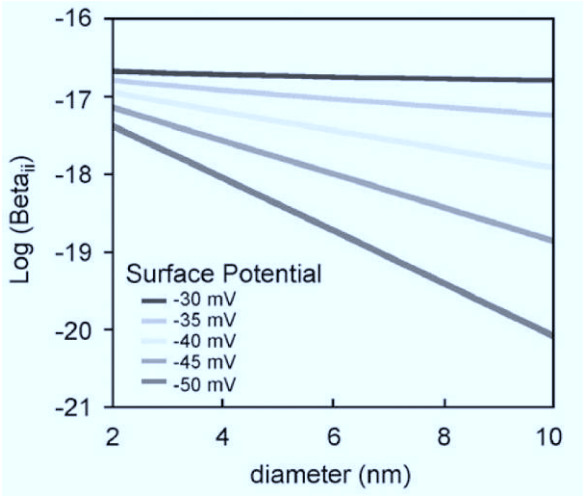

Figure 3.8 Plot of log(β_{ii}) versus nanoparticle diameter as a function of surface potential as calculated using eqs 5 and 6 in the text. Here, β_{ii} is the particle-particle coalescence rate constant for the coalescence of two identically sized and charged nanoparticles and has units of $m^3/(\#*s)$.

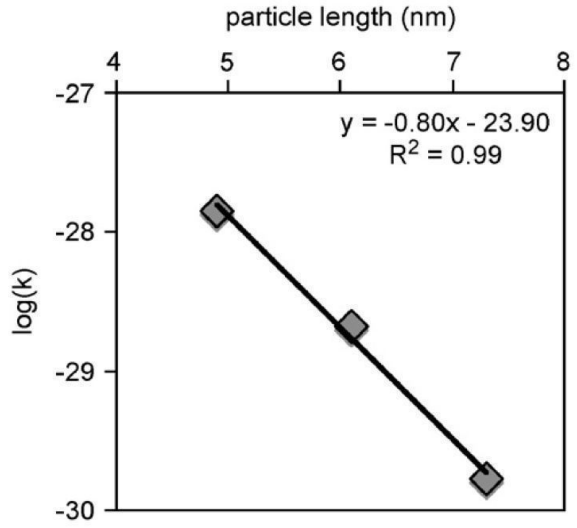

Figure 3.9 Plot of log(k) versus nanoparticle length as determined from the experimental data. Here, k has been calculated so that the units match those of β_{ii} ($m^3/(\#*s)$) in Figure 3.8.

This estimate of β_{ii} assumes a spherical particle shape, a homogeneous distribution of surface charge over the surface of the particle, a monodisperse particle size distribution, and smooth surfaces. The pH_{pzc} for individual crystal faces deviates from the average pH_{pzc} of the entire particle due to different coordination environments of surface and near-surface atoms at the various crystal surfaces (see, for example, Rustad[33]). Furthermore, at the nanometer length scale, a 4 nm particle is not smooth, and these primary particles are ellipsoidal in shape, although their aspect ratio is relatively small (~1.3). Finally, this approach overlooks both the phase transformation step in the growth of goethite oriented aggregates from ferrihydrite primary nanoparticles and the fact that the oriented aggregates themselves are not dimers but rather composed of many monomers. To date, models incorporating the phase transformation step have failed to produce reasonable fits of the experimental data and appear to be insensitive to the rate constant for the phase transformation step.

These results shed new light on how nanocrystals grow by oriented aggregation. In systems in which oriented aggregation clearly operates, a common observation is that the rate of growth by oriented aggregation during the early stages of crystallization is substantially faster than the rate of recrystallization or coarsening. At later stages of growth, coarsening and recrystallization appear to dominate crystal growth and morphology development. From images such as those described in this work and in work by Burleson and Penn,[18] one can conclude that early growth of goethite is dominated by oriented aggregation and later growth and morphology development includes coarsening and recrystallization. As the average size of the nanoparticles

increases, the contribution to overall growth and development by oriented aggregation decreases.

3.5 Conclusions

Previous results have demonstrated goethite growth by oriented aggregation.[11,18] Here, we demonstrate size control over the size of ferrihydrite nanoparticles produced from homogeneous solution and control over size of goethite crystals using the size-controlled ferrihydrite particles as precursors. Under growth conditions that favor oriented aggregation as opposed to other growth mechanisms (e.g., coarsening), control over secondary crystallite size can be achieved by controlling precursor particle size. These results are expected to broadly apply to nanocrystalline materials of any composition.

We have also shown that the rate of growth by oriented aggregation is strongly size dependent. As the size of the primary nanoparticles increases, the log of the rate of oriented aggregation decreases linearly. These results explain the common observation that oriented aggregation seems more important at early stages of nanocrystal growth in systems that both oriented aggregation and coarsening operate. As the average crystal size increases, the contribution to growth by oriented aggregation decreases.

3.6 Acknowledgements

This work was supported by the National Science Foundation (CAREER-0346385 and MIR-EAR-0320641) and the University of Minnesota. We thank T.M. Davis for insightful comments and assistance with the calculation of the particle-particle coalescence rate constant. TEM characterization was carried out at the Characterization

Facility, University of Minnesota, which receives support from NSF through the National Nanotechnology Infrastructure Network.

3.7 References

1. Niederberger, M.; Cölfen, H. Oriented attachment of mesocrystals: Non-classical crystallization mechanisms based on nanoparticle assembly. *Physical Chemistry Chemical Physics* **2006** 8, 3271.

2. Davis, T. M.; Drews, T. O.; Ramanan, H.; He, C.; Dong, J.; Schnablegger, H.; Katsoulakis, M. A.; Kokkoli, E.; McCormick, A. V.; Penn, R. L.; Tsapatsis, M. Mechanistic principles of nanoparticle evolution to zeolite crystals. *Nature Materials* **2006** 5, 400.

3. Shen, P.; Lee, W. H. (111)-Specific coalescence twinning and martensitic transformation of tetragonal ZrO_2 condensates. *Nano Letters* **2001** 1, 707.

4. Kumar, S.; Davis, T. M.; Ramanan, H.; Penn, R. L.; Tsapatsis, M. Aggregative growth of silicalite-1. *Journal of Physical Chemistry C* **2007** 111 (13), 3398.

5. Zhong, L.-S.; Hu, J.-S.; Liang, H.-P.; Cao, A.-M.; Song, W.-G.; Wan, L.-J. Self-assembled 3D flowerlike iron oxide nanostructures and their application in water treatment. *Advanced Materials* **2006** 18 (18), 2426.

6. Jia, C.; Cheng, Y.; Bao, F.; Chen, D.; Wang, Y. pH value-dependant growth of α-Fe_2O_3 hierarchical nanostructures. *Journal of Crystal Growth* **2006** 294, 353.

7. Frandsen, C.; Bahl, C. R. H.; Lebech, B.; Lefmann, K.; Theil Kuhn, L.; Keller, L.; Andersen, N. H.; Zimmermann, M. v.; Johnson, E.; Klausen, S. N.; Mørup, S. Oriented attachment and exchange coupling of α-Fe_2O_3 nanoparticles. *Physical Review B* **2005** 72, 214406.

8. Liang, X.; Wang, X.; Zhuang, J.; Chen, Y.; Wang, D.; Li, Y. Synthesis of nearly monodisperse iron oxide and oxyhydroxide nanocrystals. *Advanced Functional Materials* **2006** 16 (14), 1805.

9. Banfield, J. F.; Welch, S. A.; Zhang, H.; Ebert, T. T.; Penn, R. L. Aggregation-based crystal growth and microstructure development in natural iron oxyhydroxide biomineralization products. *Science* **2000** 289, 751.

10. Penn, R. L.; Oskam, G.; Strathmann, T. J.; Searson, P. C.; Stone, A. T.; Veblen, D. R. Epitaxial assembly in aged colloids. *J. Phys. Chem. B* **2001** 105, 2177.

11. Guyodo, Y.; Mostrom, A.; Penn, R. L.; Banerjee, S. K. From nanodots to nanorods: Oriented aggregation and magnetic evolution of nanocrystalline goethite. *Geophysical Research Letters* **2003** 30 (10), 1512.

12. Nesterova, M.; Moreau, J.; Banfield, J. F. Model biomimetic studies of templated growth and assembly of nanocrystalline FeOOH. *Geochimica et Cosmochimica Acta* **2003** 67 (6), 1185.

13. Penn, R. L.; Banfield, J. F. Morphology development and crystal growth in nanocrystalline aggregates under hydrothermal conditions: insights from titania. *Geochimica et Cosmochimica Acta* **1999** 63 (10), 1549.

14. Huang, F.; Zhang, H.; Banfield, J. F. Two-stage crystal-growth kinetics observed during hydrothermal coarsening of nanocrystalline ZnS. *Nano Letters* **2003** 3 (3), 373.

15. Huang, F.; Zhang, H.; Banfield, J. F. The role of oriented attachment crystal growth in hydrothermal coarsening of nanocrystalline ZnS. *J. Phys. Chem. B* **2003** 107, 10470.

16. Gilbert, B.; Zhang, H.; Huang, F.; Finnegan, M. P.; Waychunas, G. A.; Banfield, J. F. Special phase transformation and crystal growth pathways observed in nanoparticles. *Geochemical Transactions* **2003** 4, 20.

17. Penn, R. L. Kinetics of oriented aggregation. *J. Phys. Chem. B* **2004** 108 (34), 12707.

18. Burleson, D. J.; Penn, R. L. Two-step growth of goethite from ferrihydrite. *Langmuir* **2006** 22, 402.

19. Tang, Z.; Kotov, N. A.; Giersig, M. Spontaneous organization of single CdTe nanoparticles into luminescent nanowires. *Science* **2002** 297 (5579), 237.

20. Drews, T. O.; Tsapatsis, M. Model of the evolution of nanoparticles to crystals via an aggregative growth mechanism. *Microporous and Mesoporous Materials* **2007** 101 (1-2), 97.

21. Schwertmann, U.; Murad, E. Effect of pH on the formation of goethite and hematite from ferrihydrite. *Clays and Clay Minerals* **1983** 31 (4), 277.

22. Cornell, R. M.; Schwertmann, U., *The Iron Oxides: Structure, Properties, Reactions, Occurrences and Uses*. 2nd ed.; Wiley-VCH: Weinheim, 2003.

23. Penn, R. L.; Zhu, C.; Xu, H.; Veblen, D. R. "Iron oxide" coatings on sand grains from the Atlantic coastal plain: HRTEM characterization. *Geology* **2001** 29, 843.

24. Kurokawa, H.; Senna, M. Property control of acicular γ-Fe_2O_3 particles by synthesis conditions of starting goethite. *Funtai Kogaku Kaishi* **2000** 37, 788.

25. Varanda, L. C.; Morales, M. P.; M. Jafelicci, J.; Serna, C. J. Monodispersed spindle-type goethite nanoparticles from Fe^{III} solutions. *Journal of Materials Chemistry* **2002** 12 (12), 3649.

26. Penn, R. L.; Banfield, J. F. Imperfect oriented attachment: Dislocation generation in defect-free nanocrystals. *Science* **1998** 281 (5379), 969.

27. Hyning, D. L. V.; Klemperer, W. G.; Zukoski, C. F. Silver nanoparticle formation: Predictions and verification of the aggregative growth model. *Langmuir* **2001** 17 (11), 3128.

28. Verwey, E. J.; Overbeek, J. T. G., *Theory of the stability of lyophobic colloids*. ed.; Elsevier: Amsterdam, 1948.

29. Stokes, R. J.; Evans, D. F., *Fundamentals of Interfacial Engineering*. 1st ed.; CH Publishers: New York, NY, 1997.

30. Derjaguin, B. V.; Landau, L. Theory of the stability of strongly charged lyophobic solids and the adhesion of strongly charged particles in solution of electrolytes. *Acta Physicochimica URSS* **1941** 14, 633.

31. Penn, R. L.; Banfield, J. F. Formation of rutile nuclei at anatase {112} twin interfaces and the phase transformation mechanism in nanocrystalline titania. *American Mineralogist* **1999** 84 (5-6), 871.

32. Penn, R. L.; Banfield, J. F. Oriented attachment and growth, twinning, polytypism, and formation of metastable phases: Insights from nanocrystalline TiO_2. *American Mineralogist* **1998** 83 (9-10), 1077.

33. Rustad, J. R.; Felmy, A. R. The influence of edge sites on the development of surface charge on goethite nanoparticles: A molecular dynamics investigation. *Geochimica et Cosmochimica Acta* **2005** 69 (6), 1405.

Chapter 4

Reductive Dissolution of Arsenic-Bearing Ferrihydrite

4.1 Chapter Summary

High concentrations of arsenic, a toxic and carcinogenic element, in some aquifers have generated interest to gain a better understanding of the geochemical cycling of arsenic. Iron oxides play an important role in controlling the concentration of arsenic in solution through adsorption, coprecipitation, and dissolution. The reductive dissolution kinetics of ferrihydrites prepared with 1 or 10 wt.% arsenic by coprecipitation or adsorption have been quantified. Inductively coupled plasma-mass spectrometry (ICP-MS), inductively coupled plasma-atomic emission spectrometry (ICP-AES), transmission electron microscopy (TEM), powder X-ray diffraction (XRD), extended X-ray absorption fine structure spectroscopy (EXAFS), Mössbauer spectroscopy, and low temperature magnetic methods were used to characterize the arsenic content, particle size, and structure of the synthetic ferrihydrites. Kinetic studies monitoring the reductive dissolution of the synthetic ferrihydrites by hydroquinone yielded mass-normalized reaction rates, empirical rate laws, activation energies (E_a),

and pre-exponential factors (A), and demonstrated substantial differences between As-bearing ferrihydrites prepared by coprecipitation or by adsorption.

For ferrihydrite precipitated with or without added arsenate, the reaction rates, $E_{a,}$ and empirical rate laws for reductive dissolution were similar. Ferrihydrite equilibrated with an arsenate solution also had similar $E_{a,}$ but the empirical rate law and initial rate for reductive dissolution differed. Specifically, the initial rate of reductive dissolution of 10 wt.% As-ferrihydrite prepared by adsorption was approximately 20% of the initial rate of dissolution of the other ferrihydrite samples (e.g., 0% As-ferrihydrite and 10 wt.% As-ferrihydrite prepared by coprecipitation). It was estimated that arsenate occupies 20% of the reactive surface sites of 10 wt.% adsorbed-As; so the dramatically lower initial rate is attributed to arsenic preferentially adsorbing onto and inhibiting reductive dissolution at the most reactive surface sites, which also affects the rate law for reductive dissolution. Magnetic characterization results, which show substantially reduced particle-particle interactions for the 10 wt.% As-bearing ferrihydrites, and EXAFS and XRD demonstrate structural similarities between the 0 wt.% As and 10 wt.% adsorbed-As ferrihydrites and decreased crystallinity and potentially decreased crystallite size for the 10 wt.% coprecipitated-As ferrihydrite. High-yield reductive dissolution of the 10% adsorbed-As ferrihydrite showed a significantly higher fraction of arsenic release in comparison to the 10 wt.% coprecipitated-As ferrihydrite. Results presented here provide insight in regards to predictions of arsenic release from arsenic-bearing iron oxides in natural systems. Specifically, it is the nature of the arsenic loading, either predominantly at the surface or

incorporated into the bulk of the particles, that is expected to be the best predictor of large-scale release of arsenic from natural iron oxide particles.

4.2 Introduction

Inorganic arsenic species are carcinogenic, and arsenic in drinking water poses a threat to human health. Although arsenic occurs naturally in air, water, soil, and sediments, it is considered to be one of the leading environmental causes of cancer mortality in the world.[1] Recently, high concentrations of arsenic in groundwater around the world have generated interest in elucidating the mechanisms controlling the geochemical cycling of arsenic in groundwater systems.[2] Arsenic has a high adsorption affinity for iron oxide surfaces; however, the mechanisms of adsorption and release in aquifers are not well understood.[3] The development of strongly reducing conditions at near-neutral pH has been suggested as one mechanism that can result in the large-scale release of arsenic from aquifer materials.[4] Arsenic may be released by simple desorption or through concurrent release from dissolving arsenic-bearing metal oxides.[2]

Arsenic is a major component in many minerals, including arsenides, sulfides, oxides, arsenates, and arsenites. In sediments, arsenic is frequently associated with iron. Arsenopyrite (FeAsS), the most abundant As ore mineral, and arsenian or "As-rich" pyrite, $Fe(As,S)_2$, are not stable under aerobic conditions and oxidize, which can result in the release of Fe(II) and sulfuric acid, a process known as acid-mine drainage.[2] Dissolved arsenic or other species are rapidly removed from the solution upon the oxidation of Fe(II) and precipitation of iron oxides. Iron oxides play an important role in attenuating the concentration of arsenic in solution through adsorption and coprecipitation.[5] Due to its high affinity for iron oxides, arsenic concentrations in

natural ferrihydrite samples have been documented with values up to 14 wt.% As.[6] Arsenic may be released from or adsorb onto iron oxide surfaces depending on the groundwater solution properties, especially pH and redox conditions.[2]

Iron oxides, which includes both iron oxide and (oxy)hydroxide minerals, are ubiquitous at and near the Earth's surface. Due to their natural abundance, redox reactivity, and surface adsorptivity, iron oxides play an important role in the transformation and transport of species such as heavy metals and anthropogenic contaminants.[7-9] Dissolved iron species can be produced by weathering of primary minerals, such as FeS_2 and other iron-bearing minerals. Iron oxides may form through precipitation of aqueous iron species and are often found in and near surface water.[3] Iron oxides may be reduced through biotic[10] or abiotic[11] electron transfer reactions with organic compounds, including quinone species and humic substances.[12] Reductive dissolution can cause the release of adsorbed or incorporated species and can lead to growth and phase transformations.[13]

One iron oxide mineral, ferrihydrite ($Fe_5HO_8 \cdot 4H_2O$), precipitates when iron-rich waters increase in pH and/or become oxidized.[14,15] Ferrihydrite is a poorly crystalline, metastable mineral typically ranging in size from a 3-10 nanometers and is a precursor to goethite and hematite.[15,16] The high degree of structural disorder and high specific surface area of ferrihydrite make it one of the most reactive of the iron oxide minerals. It can incorporate ions, such as arsenate from solution and, therefore, may influence the transport of such species in natural systems. Furthermore, precipitation, dissolution, and redox reactivity are strongly affected by the presence of species like arsenate in

solution, adsorbed onto mineral surfaces, or incorporated into the bulk of the iron oxide minerals.[17]

X-ray absorption (XAS), infrared, and Raman spectroscopy studies have shown that, when arsenate is adsorbed on iron oxide surfaces, and specifically ferrihydrite, it typically forms inner-sphere complexes.[3] Extended X-ray absorption fine structure spectroscopy (EXAFS) results[18-21] from arsenic-bearing ferrihydrite samples indicate that arsenate adsorbs primarily as a corner-sharing bidentate complex on the apical oxygens of two adjacent edge-sharing iron octahedra or in a monodentate complex. Some debate has arisen over the presence and prevalence of edge-sharing bidentate complexes, because these arsenate complexes on iron oxide surfaces are higher in energy.

Magnetic properties are sensitive to structural and compositional differences; and ferrihydrite, in both doped and undoped forms, has been characterized using magnetic methods by many authors.[22-26] It is an antiferromagnetic material and exhibits superparamagnetic behavior at room temperature.[15,22] Fundamental questions include ferrihydrite's non-zero net magnetization, which was predicted by Néel for nanophase antiferromagnetic materials; magnetic super-exchange interactions within aggregates; and uncompensated magnetic moments. Above the blocking temperature, superparamagnetic effects suppress important intrinsic magnetic properties of ferrihydrite, such as the Néel temperature (T_N). Recently, T_N of ferrihydrite was estimated to be about 500 K using data from ferrihydrite with small particle sizes from 3.0-5.4 nm[22] and around 422 K using data extracted from a sample with unusually large particle size of 23 nm.[26] Ferritin, an iron-storage protein of mammals in which

ferrihydrite appears to be the protein core, is frequently used in magnetic studies.[27,28] Interparticle super-exchange interactions, a common phenomenon that complicates the interpretation of magnetic data from nanoparticles, are not observed in ferritin.

Magnetic studies of ferrihydrites prepared with a range of dopants (Ni, Mo, Ir, B, Al, As, Si) have been reported, although such studies lack conclusive data about lattice substitution. In fact, the main effects observed are decreased crystallinity or average particle size for doped versus undoped materials. For natural arsenic-bearing ferrihydrites formed from hydrothermal fluids, Rancourt et al.[6] observed that incorporation of arsenic prevented particle growth, led to smaller primary particles, and caused structural disorder by distorting the Fe octahedral environments. It was proposed that arsenic was adsorbed at the surface of ~1 nm diameter primary particles and hence did not enter the ferrihydrite lattice. Mössbauer spectroscopy has been used to investigate structural variations in doped ferrihydrite by quantifying magnetic hyperfine field (B_{HF}) variations and comparing to a standard, pure ferrihydrite but results to date have been inconclusive.[15,25,26]

Here, we present quantitative results of kinetic studies of the reductive dissolution and comprehensive characterization of six ferrihydrite samples to elucidate how the method of arsenic addition to iron oxide materials influences the reaction kinetics and the release of arsenic upon reduction. Samples were prepared by forced hydrolysis of ferric nitrate solutions. Two samples were prepared by coprecipitation with As, three samples were prepared by equilibration with a solution containing arsenate after precipitation, and one sample was prepared without added As. The composition, particle size, crystallite size, structural properties, magnetic properties, and

surface properties of ferrihydrite samples were characterized. Combined results lead to a prediction that the reductive dissolution of ferrihydrite with arsenate located primarily at the surface is more likely to lead to substantial release of arsenate from the solid surface to the solution phase.

4.3 Experimental Methods

4.3.1 *Synthesis of Materials*

Solutions were prepared with 18MΩ•cm resistivity water (Milli-Q water, Millipore Corporation). All glassware and Nalgene bottles were acid washed with 4 M nitric acid and rinsed three times with Milli-Q water. Ferrihydrite suspensions were prepared by addition of a 0.48 M $NaHCO_3$ (Mallinckrodt) solution to an equal volume of 0.40 M $Fe(NO_3)_3$•$9H_2O$ (Fisher) solution. The base solution was added over 12 ±1 min using a Fisher peristaltic pump, and the mixture was stirred constantly using a magnetic Teflon-coated stir bar. Over the course of the base addition, the orange color of the initial ferric nitrate solution changed to a dark red-brown color. Next, the suspension was microwave-annealed (950 Watt oven) at 30-second intervals until it boiled. The bottle containing the suspension was immediately submerged into an ice bath until it cooled to room temperature and then the suspension was transferred to Spectra-Por #7 dialysis bags (MWCO = 2000 g/mol). Dialysis against Milli-Q water was performed for three days at room temperature, changing the water at least nine times. The ferrihydrite suspensions were allowed to air dry for several days, ground into powders using an agate mortar and pestle, and then stored in dry glass vials.

Arsenic was added by way of coprecipitation or adsorption after precipitation. The source of arsenic was Na_2HAsO_4•$7H_2O$ (Fluka), which was added to obtain

approximately 1 or 10 wt.% of arsenic in the synthetic materials and was calculated using the Dzombak and Morel ferrihydrite formula weight of 89 g/mol Fe.[29] For samples with adsorbed arsenic, the ferrihydrite suspension was prepared and dialyzed as above. Then, the appropriate amount of arsenate solution, with the pH adjusted to match that of the ferrihydrite suspension, was added to the ferrihydrite suspension and the solution was equilibrated for one or eighteen days. Upon addition of the arsenate solution and after stirring for one hour the pH of the ferrihydrite suspension rose significantly (from 3.4 to 5.3). The resulting suspension was dialyzed against Milli-Q water over three days with a minimum of nine water changes. For samples with coprecipitated arsenic, the arsenate salt was added to the ferric nitrate solution before hydrolysis. Then, hydrolysis, microwave-anneal, dialysis, and drying steps were performed as described above for ferrihydrite prepared with no arsenic. The dialysis waste solutions from samples containing arsenic were treated using an iron slurry to remove dissolved arsenic and disposed of as hazardous waste. The adsorbed-As and coprecipitated-As ferrihydrite suspensions and powders were similar in color to the unmodified ferrihydrite. Hereafter, the samples are named according to their approximate, attempted arsenic content (1 or 10%) and the method of incorporation (COP for coprecipitation or ADS for equilibrium/adsorption), and the pure ferrihydrite sample is referred to as 0% As.

4.3.2 *Materials Characterization*

Ferrihydrite samples were characterized using inductively coupled plasma-mass spectrometry (ICP-MS) or inductively coupled plasma-atomic emission spectroscopy (ICP-AES), powder X-ray diffraction (XRD), transmission electron microscopy (TEM),

extended X-ray absorption fine structure spectroscopy (EXAFS), superconducting quantum interference device (SQUID) magnetometry, Mössbauer spectrometry, and potentiometric titrations.

Solid samples were prepared for ICP-MS by dissolving the solid particles in 3.2 M HNO_3 and then further diluted with 0.1 M HNO_3. For ICP-AES, solid samples were digested with aqua regia, diluted with Milli-Q water, and further diluted with 0.1 M HNO_3. The diluted solutions were analyzed for Fe, As, and Na content using a ThermoElemental PX ExCell quadrupole mass spectrometer for ICP-MS or a Perkin Elmer Optima 3000DV ICP in radial or axial mode for ICP-AES.

X-ray diffraction was performed using a PANalytical X-Pert PRO MPD X-ray diffractometer equipped with a cobalt source and an X-Celerator detector. All scans were collected from front-packed powder samples over the range of 10-90º 2θ at a scan rate of 0.6º per minute. The diffraction patterns were compared to the reference powder diffraction file (PDF) for six-line ferrihydrite (#29-0712), goethite (#29-0713), and hematite (#33-0664).

Attempts to obtain BET surface areas of ferrihydrite powders were unsuccessful, so surface areas were determined from TEM image measurements. Each TEM sample was prepared by drop casting a diluted suspension prepared by adding 1 drop of dialyzed suspension to 2 mL of Milli-Q water. A drop of the diluted suspension was placed onto a 3 mm 200 mesh holey carbon-coated copper grid (Structure Probe, Inc.) and allowed to air dry. Images were collected using an FEI Tecnai T12 TEM operated at 120 kV and equipped with a Gatan CCD camera. The size and morphology of the samples were analyzed using Gatan Digital Micrograph 3.8.2. The lengths and widths

of more than 500 particles were measured from the calibrated TEM images. The specific surface area of each sample was calculated using the density of ferrihydrite (3.96 g/cm^3),[15] the surface area per volume, and modeling of the particles as ellipsoids as in Jentzsch and Penn.[30]

4.3.3 *EXAFS*

EXAFS spectroscopy was conducted at Stanford Synchrotron Radiation Laboratory (SSRL) wiggler magnet beamline 10-2 under anaerobic conditions for the 0% As, 1-day 10% ADS, 18-day 10% ADS, and 10% COP ferrihydrites. A 1:10 mass dilution of dry powder sample to boron nitride powder was used to reduce self-absorption effects. The diluted samples were analyzed in 1.5 mm thick Teflon holders sealed with Kapton tape using a double Si 111 phi = 90° monochromator crystal with the beam detuned 30% from its maximum intensity to reduce harmonic contents. Fe K-edge (7112 eV) EXAFS spectra were collected at room temperature in transmission mode using a Fe^0 calibration foil over the energy range 6879-7986 eV.

Data were analyzed using SixPACK software version 0.60.[31] EXAFS scans were calibrated for changes in assigned monochromator energy to 7112 eV by using the first derivative of the Fe calibration standard and averaged together. These spectra were deglitched when needed. Background subtraction was performed using SixPACK with (E_0) defined as 7125 eV, the *k*-weight = 3, and the R-background = 1 Å. The resulting spectra were converted to frequency (*k*) space, weighted by k^3, and Fourier transformed to produce R-space EXAFS. Quantitative fitting of the background subtracted and k^3-weighted spectra was performed using model single scattering paths created in SixPACK using FEFF 6l.[32]

The shell-by-shell approach to fitting the EXAFS spectra was adapted from Kim et al.[33,34] Briefly, the amplitude reduction factor (S_0^2) was fixed at 0.9 for all samples. The Debye-Waller factor (σ^2) was set at optimum values of 0.007 for the first-shell atomic neighbors and 0.01 for the second- and third-shell atomic neighbors initially. Coordination number (CN) and σ^2 are highly correlated, and varying both simultaneously can produce unreasonable (nonphysical) uncertainty in the fit result.[35] Therefore, CN values were determined initially by restricting σ^2 to 0.007 for the first shell and 0.01 for subsequent shells and allowing SixPACK to vary all other parameters, except S_0^2, and then the CN values were held constant while σ^2 was allowed to vary with the other parameters. The Fe-Fe shell at ~3.45 Å was determined to be 0.001-0.004 and was restricted while the other parameters were allowed to vary.

4.3.4 ***Magnetism***

A commercial SQUID magnetometer (MPMS-XL, Quantum Design) was employed to obtain ZFC/FC magnetization curves and hysteresis loops on the 0% As, 18-day 10% ADS, and 10% COP ferrihydrites as a function of temperature. Zero-field-cooled (ZFC) magnetization curves were obtained by cooling the sample in zero field from a high temperature (300 K) to a low temperature (2 K) and then measuring the magnetization at stepwise increasing temperatures from 2 K to 300 K induced in a small applied field (H=5 mT). The sample was again cooled, in the same field, and field-cooled (FC) magnetization curves were obtained by measuring (in field) at stepwise increasing temperatures, from 2 K to 300 K. Hysteresis loops were obtained by using maximum applied fields up to 5 T at temperatures of 5 K. Mössbauer spectra were measured at room temperature and at 4.2 K. A conventional constant-acceleration

spectrometer was used in transmission geometry with a ^{57}Co/Rh source, using α-Fe at room temperature to calibrate isomer shifts and velocity scale.

4.3.5 *Potentiometric Titrations*

The 0% As, 10% COP, 1-day 10% ADS, and 18-day 10% ADS ferrihydrites were used in acid-base potentiometric titrations at three ionic strengths to determine the point of zero net proton charge (PZNPC). Freshly prepared ferrihydrite suspensions were dialyzed but not dried for titration experiments. Standard procedures[29] were followed for the titrations with the exception that CO_2 was not excluded from the ferrihydrite suspensions prior to titrations. The presence of CO_2 during acid-base titrations was discussed by Gilbert et al.[36] and was not expected to have a significant effect on the titration of ferrihydrite samples. The titrations were completed manually with 40 mL of suspension with a ferrihydrite solid concentration of 2.5 or 5.0 g/L using 9×10^{-3} M NaOH solutions (prepared with CO_2-free Milli-Q) at ionic strengths of 0.1, 0.01, and 0.001 M $NaNO_3$. The pH was recorded with a Thermo PerpHect Sure-Flow glass pH electrode calibrated with buffers at pH 4 and 10 and Logger Pro 3.6.1 software by Vernier. Titrations took 25-40 minutes to complete and measurements were recorded 25 seconds after the aliquot of base was added. Background titrations of pH 4 HNO_3 solutions at each ionic strength were performed. Total surface charge density, or the amount of protons adsorbed, was obtained from the resulting titration curve by subtraction of the blank titration curve data. Charge density was calculated using the adsorbed proton quantity, solids loading, and surface areas determined by TEM analysis. The PZNPC was identified as the common intersection point of the titration curves at different ionic strengths for each ferrihydrite suspension.

4.3.6 *Kinetic Reactions*

The reactivity of iron oxides has been quantified previously by measuring the kinetics of reductive dissolution using hydroquinone and monitoring the formation of benzoquinone.[11,30,37,38] Experiments were performed in duplicate or triplicate, the pH buffered using 40 mM acetate (pH 3.75, acetic acid (Mallinckrodt) and sodium hydroxide (Mallinckrodt) in Milli-Q water), and performed in an anaerobic chamber (Coy Laboratories, 5% H_2/95% N_2). To prevent exposure to light, 30-mL amber glass vials or 30-mL Nalgene bottles wrapped in aluminum foil were used.

For variable temperature studies, the total volume of suspension was 12.5 mL with 2.0 g/L ferrihydrite loading and 0.2 mM hydroquinone in acetate buffer (40 mM, pH 3.75). For reaction order studies, the total volume of suspension was 25.0 mL with 0.5-2.0 g/L ferrihydrite loading, 0.05-0.80 mM hydroquinone, and 40 mM acetate buffer. Dried powders were weighed into bottles and placed into the anaerobic chamber. Then, 5.0-mL of deoxygenated acetate buffer was added. Samples were sonicated for 20 minutes, vortexed, and stirred overnight to reduce aggregation of particles. The following day, an appropriate volume of acetate buffer and 10 mM hydroquinone stock solution (prepared with 40 mM acetate buffer) was added to the reaction vessel. At regular time intervals, 1-mL aliquots were removed and filtered using 0.2-μm nylon Acrodisc filters and analyzed within 2 minutes by high performance liquid chromatography (HPLC), as described below. The filtrate was clear, indicating that the solid was effectively removed from the suspension; thus, the reaction was quenched.

Solutions were analyzed with an Agilent HPLC equipped with a Zorbax C_{18} column. The mobile phase was a 65:35 mixture of acetate buffer (40 mM, pH 3.75) and

acetonitrile. The flow rate was 0.75 mL/min and the injection volume was 10 μL. The absorbance was monitored at 235 nm, and hydroquinone eluted at 2.3 min and benzoquinone at 3.4 min. Eight-point calibration curves, ranging from 0.05 to 2.0 mM for hydroquinone and 2 to 150 μM for benzoquinone, were used to determine experimental concentrations.

For a subset of kinetic experiments, [Fe(II)] (aq) was measured by a modified version of the Ferrozine assay.[39] A 0.4-mL aliquot of the filtrate solution was combined with 0.25 mL of Ferrozine solution (5 mg/mL in 40 mM acetate buffer, Acros, 99.9%) and 4.35 mL of 40 mM, pH 3.75 acetate buffer. Absorbance at 562 nm was measured using a Spectrophotometric 20D+ UV-visible spectrophotometer. A Ferrozine/acetate buffer solution was used as a blank, and a six-point calibration curve up to 10^{-4} M $FeCl_2 \cdot 4H_2O$ (Fisher, 99%) was employed. There is no evidence for interference by arsenic complexes with the Ferrozine assay.[39]

To gain insight into arsenic release from the 18-day 10% ADS and 10% COP samples, a similar procedure was followed as described above, but the initial hydroquinone concentration was 6.0 mM, the ferrihydrite loading was 0.5 g/L, and the reaction vessel was maintained at room temperature. At selected time intervals up to four days, sample suspensions were filtered through two Acrodisc filters and analyzed. Benzoquinone and Fe(II) concentrations were measured by methods described above. A subset of filtrates were acidified by adding a known volume of 1 M HCl to a known volume of filtrate and then stored at 10 ºC until analyzed by ICP-AES to measure the concentration of dissolved Fe and As. In addition, filtrate was collected from a blank suspension, which was equilibrated with the ferrihydrite solids overnight, for ICP

analysis. Attempts to detect and quantify arsenate and arsenite from filtrates using the molybdene-blue method[40] were unsuccessful.

4.4 Results and Discussion

4.4.1 *Materials Characterization*

The Fe, As, and Na content of the solids was determined by ICP-MS or ICP-AES of dissolved samples, and results are presented in Table 4.1. The arsenic-bearing samples had approximately 1 or 10 weight-percent of arsenic and the iron content dropped accordingly. For samples prepared with an intended 10 wt.% As by equilibration with an arsenate solution, the sample contained 8.5 wt.% As after one day of equilibration and 9.6 wt. % after 18 days of equilibration. These results are consistent with the high affinity of arsenic for iron oxide by adsorption from solution. The results also agree with those of Fuller et al. on the kinetics of arsenate adsorption, which showed that an initial, rapid arsenate adsorption was followed by arsenate adsorption at a slower rate for at least eight days.[41] Sodium was a minor impurity and was attributed to the starting material salts; however, the 1-day and 18-day 10% ADS samples had significantly higher sodium content, which can be explained by the co-adsorption of protons and sodium cations with the arsenate anion (AsO_4^{3-}) to maintain charge balance.

Table 4.1 Elemental composition of ferrihydrite samples by ICP analysis.

sample	iron (wt.%)	arsenic (wt.%)	sodium (wt. %)
0% As	55.0	<0.035	BDL
1% ADS	53.9	1.57	BDL
10% ADS (1-day)	42.8	8.48	0.546
10% ADS (18-day)	43.5	9.55	0.754
1% COP	50.8	1.25	BDL
10% COP	41.3	10.5	BDL

BDL: concentrations below the instrumental limit of detection

The powder X-ray diffraction patterns of the ferrihydrite samples, shown in Figure 4.1, were consistent with the six-line ferrihydrite powder diffraction file (#29-0712), and there was no evidence for the presence of other crystalline phases. The patterns of the 0% As, 1% ADS, and 1% COP samples were indistinguishable. The XRD pattern for the 10% ADS (18-day) is similar to the aforementioned samples, although a reduction in relative peak intensities of the second through sixth lines relative to the first line and possibly some broadening of the third and fourth lines can be discerned. This indicates that subtle structural changes result from the adsorption of arsenate, perhaps including some diffusion of arsenate into the bulk of the particles. The 10% COP diffraction pattern differed markedly from the other samples. The peaks were poorly defined and broad, indicating a significant difference in particle size and/or crystallinity of the 10% COP sample.

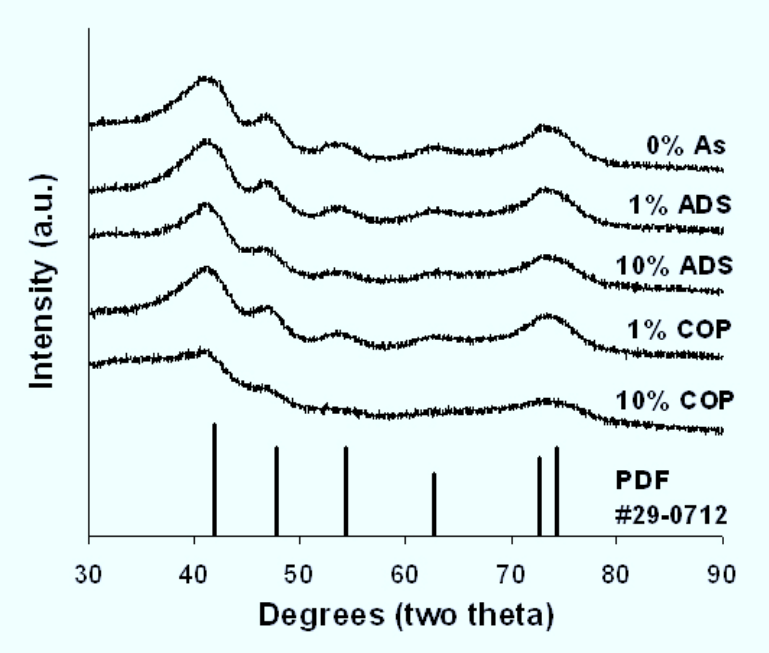

Figure 4.1 XRD patterns 0% As, 1% ADS, 18-day 10% ADS, and 1% COP, and 10% COP. The PDF pattern for six-line ferrihydrite (#29-0712) is shown as a stick pattern.

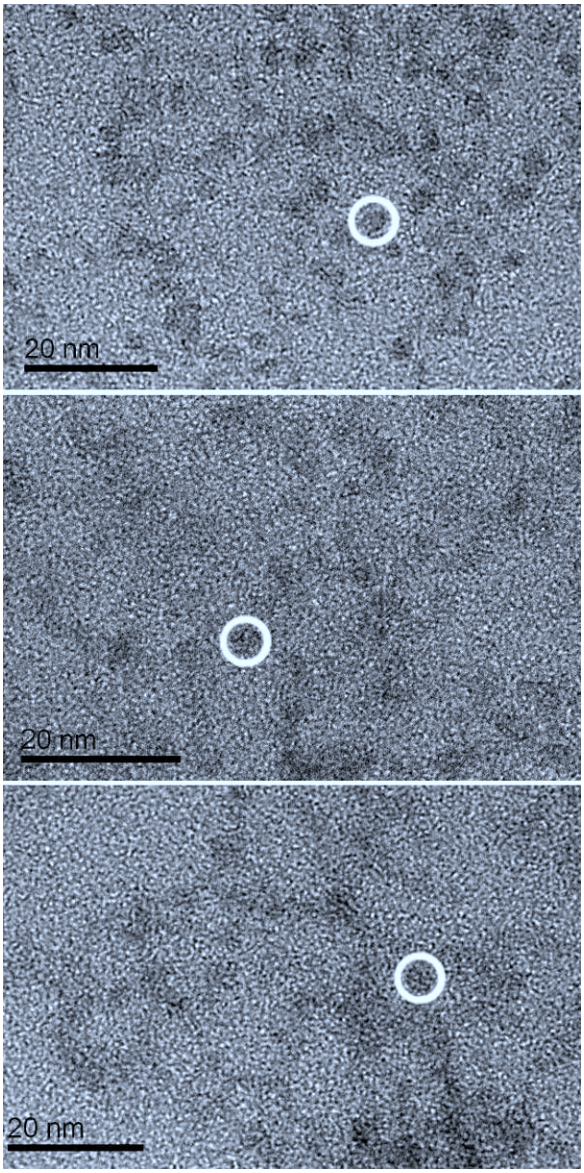

Figure 4.2 Representative TEM images of 0% As (upper), 18-day 10% ADS (middle), and 10% COP (lower) ferrihydrite samples.

Figure 4.2 shows representative TEM images of the 0% As, 10% ADS (18-day), and 10% COP samples. The ellipsoidal particle morphology was confirmed in the images, and the particle size distributions and calculated specific surface areas are reported in Table 4.2 for the three samples. No significant difference in size was observed, even when considering a 5% error in absolute size by TEM. Average lengths

ranged from 4.2 nm for the 10% COP sample to 4.4 nm for the 10% ADS sample, which yield calculated specific surface areas ranging from 420 to 450 m^2/g. Because there is only a small variation in size between the pure ferrihydrite and 10% As-ferrihydrites, it was assumed that the 1% As-bearing ferrihydrites have similar particle size distributions.

Table 4.2 Average particle length and width distributions (with standard deviations as error) for ferrihydrite samples as determined using TEM and calculated specific surface areas.

sample	particle length (nm)	particle width (nm)	specific surface area (m^2/g)
0% As	4.3 ± 0.3	3.1 ± 0.5	430
10% ADS (18-day)	4.4 ± 0.3	3.2 ± 0.3	420
10% COP	4.2 ± 0.3	2.9 ± 0.3	450

The similarity in TEM particle size of the samples suggests that the XRD peak broadening of 10% COP is likely the consequence of decreased crystallinity rather than smaller particle size. Fuller et al. reported that the presence of adsorbed ions may affect aggregation and crystallite growth,[41] and incorporation of arsenate tetrahedra into the predominantly octahedral crystal structure of ferrihydrite may result in the formation of defects within the particles. However, Waychunas et al. (1995)[20] concluded that coprecipitation of high arsenate content limits the size of ferrihydrite crystallites by poisoning iron octahedral chain corners and edges. Applying the Scherrer equation to wide angle X-ray scattering data, Waychunas et al. (1996)[42] estimated a considerably smaller crystallite size of coprecipitated, 33 wt.% As two-line ferrihydrite (5.8 Å) compared to the undoped two-line ferrihydrite (11.7 Å) and concluded that larger particle sizes determined by methods such as TEM could be attributed to agglomerates

of smaller individual crystallites. However, the consistent size and aspect ratio over the three samples argues against a fundamental difference in agglomeration state. Therefore, we conclude that the broadening of the XRD peaks for 10% COP is primarily due to decreased crystallinity.

4.4.2 *EXAFS*

The structural similarities seen in XRD data between the 0% As, 1-day 10% ADS, and 18-day 10% ADS samples, as well as the structural differences between those particles and the 10% COP particles are reinforced by the EXAFS data. There are marked reductions in Fe-Fe coordination number between the ADS and the COP samples. Table 4.3 shows the fitting results for Fe K-edge EXAFS shell-by-shell fitting and Figure 4.3 shows the raw data and fitting results.

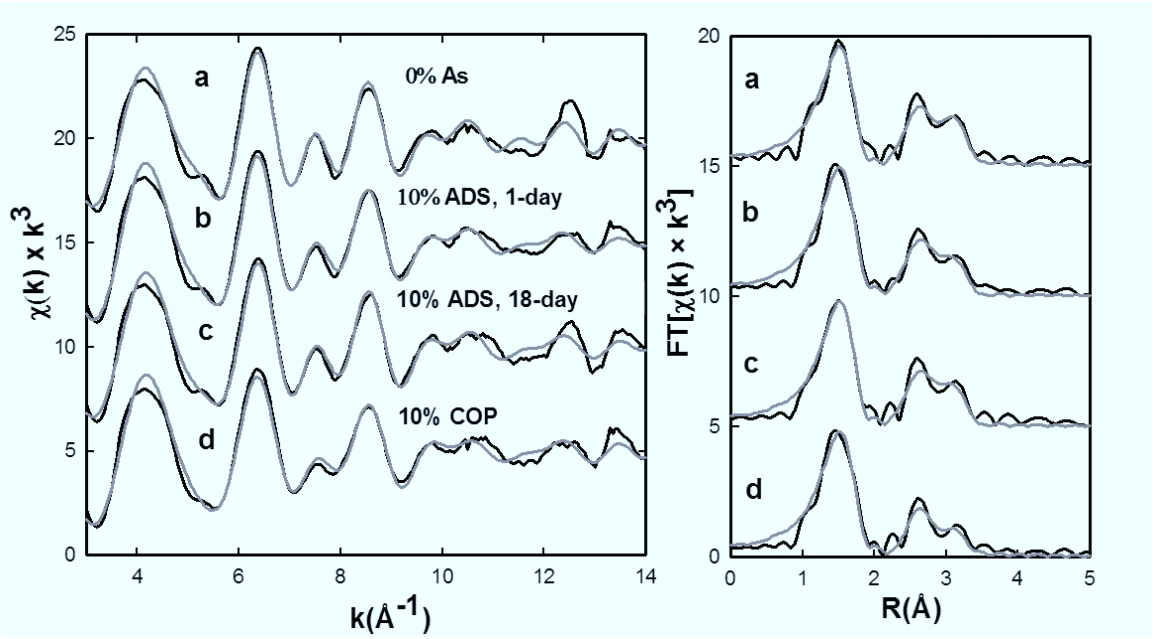

Figure 4.3 Fe K-edge k^3-weighted EXAFS and corresponding Fourier transforms and fits (black = data, grey = fits) for 0%, 1-day 10% ADS, 18-day 10% ADS, and 10% COP ferrihydrite.

Table 4.3 Fe k-edge EXAFS fitting results for As-ferrihydrite sorption and coprecipitated samples (see Figure 4.3 for EXAFS and Fourier transform spectra). CN = coordination number, R = interatomic distance, and σ^2 = Debye-Waller factor.

sample	Fe-O			Fe-Fe			Fe-Fe		
	CN	R(Å)	σ^2(Å^2)	CN	R(Å)	σ^2(Å^2)	CN	R(Å)	σ^2(Å^2)
0% As	3.2(5)	1.96(1)	0.009(1)	1.6(7)	3.02(2)	0.010(3)	0.5(1)	3.45(2)	0.003*
10% ADS (1-day)	3.7(4)	1.972(9)	0.009(1)	1.6(7)	3.03(2)	0.010(3)	0.5(2)	3.45(2)	0.004*
10% ADS (18-day)	3.3(4)	1.97(1)	0.008(1)	1.3(6)	3.03(2)	0.009(4)	0.5(2)	3.44(2)	0.004*
10% COP	3.5(4)	1.97(1)	0.009(1)	1.0(5)	3.03(1)	0.008(3)	0.21(9)	3.44(2)	0.001*

*Note: the Debye-Waller factor value for the second Fe-Fe shell (at 3.45 Å) was roughly determined as an isolated variable, and then subsequently held constant, thus there is no error indicated in the table.

There is no change in Fe coordination environment at 1 day of exposure when the addition of arsenate to the system was after particle formation (1-day 10% ADS), and the mode of association is likely adsorption. There is, however, a reduction in the 18-day 10% ADS sample in Fe-Fe coordination at distance of ~3.03 Å from 1.6 to 1.3. This reduction is likely the As replacing surface bound Fe and possibly incorporating into the bulk ferrihydrite structure. The most prominent effect on CN occurred when As was coprecipitated during the formation of ferrihydrite. For coprecipitation, the average CN of the Fe-Fe bonds at ~3.03 Å was reduced to 1.0; down from 1.6 for unexposed particles and those with only 1 day of exposure, and down from 1.3 for particles with 18 days of exposure. Fe-Fe bonds at a distance of ~3.45 were unaffected by exposure to As post formation, but experienced a reduction in CN from 0.5 to 0.21, for the coprecipitated case. The bond distances and coordination numbers, as well as the reduction in CN caused by coprecipitation, mimic those seen by Waychunas et al. (1993) for similar systems.[18] Waychunas et al. (1993) also showed that a variety of As

bonding geometries result in a bond distance near 3.45 Å, and it is likely that the spectral features that result in the peak at that distance in the Fourier transforms contain some contribution from Fe-As bonds, however attempts by Waychunas et al., (1993) to fit Fe-As shells at that distance often produced unreasonable fitting results, and in the end only three shells, one Fe-O and two Fe-Fe were accepted. Simultaneous with the decrease in Fe-Fe coordination at 3.45 Å was an improvement, or decrease, in the Debye-Waller factor (σ^2) in the co-precipitated sample. A greater σ^2-value is indicative of greater disorder in a particular bond parallel to the bond direction from its average length.[43] Arsenic incorporation or replacement of weakly bound Fe sites, resulting in more strongly bound Fe could explain the decrease in Fe-Fe coordination and the decrease in σ^2.

4.4.3 *Magnetism*

Figure 4.4 shows the ZFC/FC magnetization curves for the 0% As, 18-day 10% ADS, and 10% COP ferrihydrite samples. Superparamagnetic behavior was observed; i.e., the occurrence of the peak in each ZFC curve and the overlap of ZFC and FC curves above the temperature at which all particles are unblocked. The blocking temperatures (T_B), which were determined from the maximum magnetization of ZFC curves, were estimated to be 45 ±2 K, 33 ±2 K, 27 ±2 K for samples 0% As, 18-day 10% ADS, and 10% COP, respectively. Blocking temperature (T_B) is associated with volume (V) by the equation

$$V = \frac{25 k_B T_B}{K} \qquad (1)$$

where k_B is the Boltzmann constant and K is the anisotropy constant, which is material specific. As can be seen from the equation above, T_B is proportional to V, and when the average particle size becomes smaller, T_B is expected to decrease.[44] For 18-day 10% ADS and 10% COP, T_B decreased and the ZFC peak shape, representing the distribution of particle volume, narrowed as compared to 0% As.

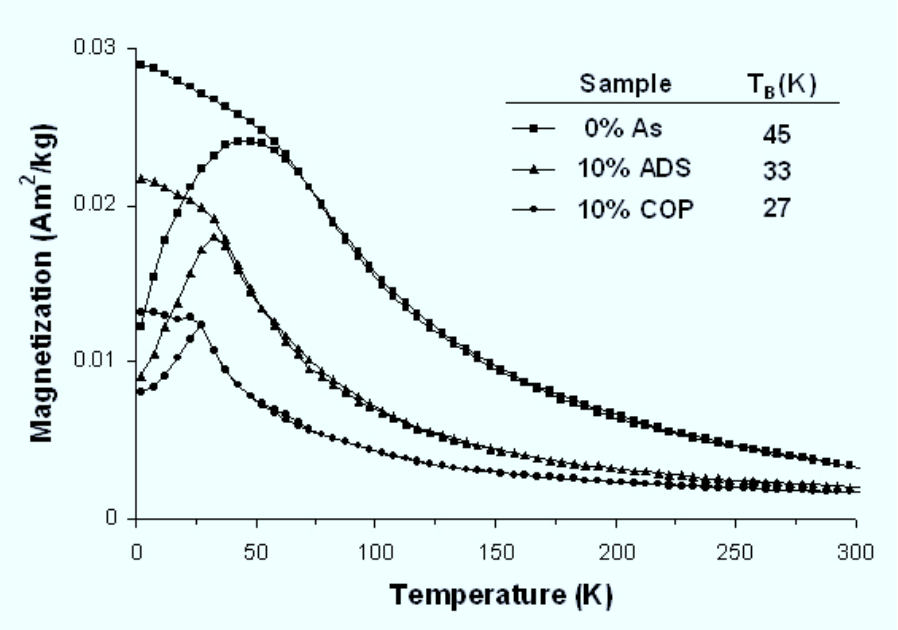

Figure 4.4 ZFC/FC curves for 0% As, 18-day 10% ADS, and 10% COP samples.

Two hypotheses can be associated with the observed decrease in T_B. The first one, observed by Rancourt et al.,[6] is related to the decrease in crystallite size. The presence of arsenate during precipitation may inhibit nucleation and growth, resulting in smaller crystallites. By TEM, the average particle size of 10% COP is indistinguishable from that of the other samples (Table 4.2 and Figure 4.2). However, the TEM particle sizes may reflect the size of aggregated crystallites, which may be smaller in the 10% COP ferrihydrite as discussed earlier. The hypothesis does not explain the decrease of

T_B for the 10% ADS ZFC curve since arsenic adsorbed after synthesis is not expected to affect the primary particle size, which was confirmed by TEM (Table 4.2).

The second hypothesis is related to effects of magnetic super-exchange interactions resulting from particle agglomeration. Magnetic interaction effects have been the focus of many studies since they have a strong influence on the magnetic properties of nanoparticles. It has been documented that T_B decreases when particles are well dispersed.[44] Frandsen and Mørup documented a marked decrease in T_B for coated hematite nanoparticles.[45] Additionally, a reduction of interaction effects has been demonstrated for ferrihydrite by coating with sugar or alginate, as evidenced by a drastically lowered T_B (12 K) and sharper ZFC peak for each coated sample as compared to the uncoated sample.[46] This second hypothesis suggests that arsenic likely forms a partial coating on the arsenic-bearing ferrihydrite particles, particularly for the 10% ADS, which could slightly increase interparticle separation within aggregates and consequently lower magnetic interactions and decrease T_B. The ZFC peak shape for 10% ADS is also substantially sharper than for 0% As, which suggests the presence of As at particle surfaces and interfaces, which narrows the volume distribution due to attenuated particle-particle interactions.

The magnetic hysteresis loops of the 0% As, 18-day 10% ADS, and 10% COP samples collected at 4.2 K for are presented in Figure 4.5. The behavior for all three samples was similar, and they did not achieve saturation even at 5 T, which is consistent with behavior usually observed for antiferromagnetic materials. Saturation magnetization and coercive force both decrease with arsenic adsorption and

coprecipitation. The 10% COP sample has the lowest saturation magnetization, consistent with arsenic substitution within the ferrihydrite lattice.[47]

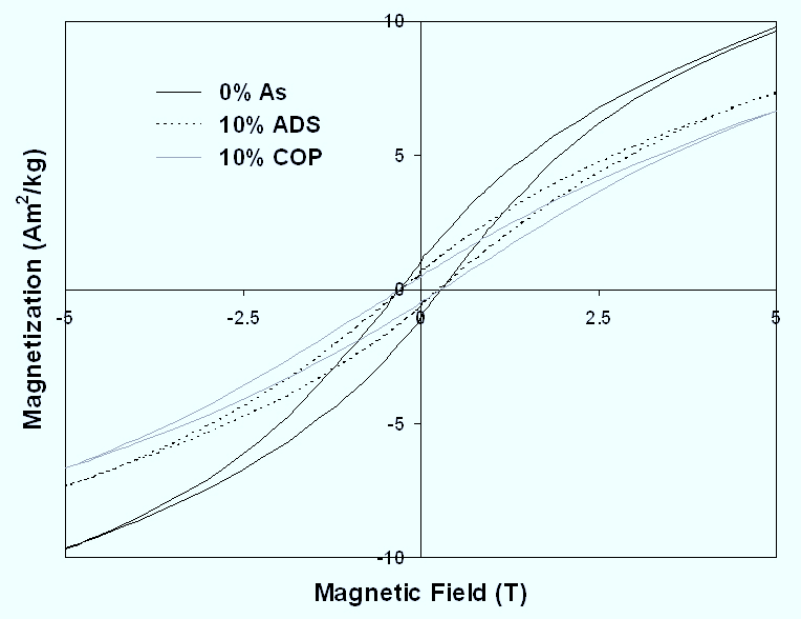

Figure 4.5 Hysteresis loops of 0% As, 18-day 10% ADS, and 10% COP ferrihydrites at 4.2 K demonstrate that the samples do not attain saturation.

Mössbauer spectra collected at 4.2 K of the 10% COP, 18-day 10% ADS, and 0% As samples (Figure 4.6) show sextets corresponding to magnetic ordering below the T_B and T_N. The Mössbauer spectra taken at room temperature (not shown) are represented only by doublets due to thermal fluctuations (superparamagnetism), indicating the particles were unblocked at this temperature. The magnetic hyperfine parameters at 4.2 K are presented in Table 4.4. The magnetic hyperfine field (B_{HF}) for the 0% sample, 49.6 T, was close to standard values available for ferrihydrite (B_{HF} =50.0 T).[48] The parameter B_{HF} was lower (48.5 T) for 18-day 10% ADS but even lower (47.9 T) for 10% COP. The decrease in B_{HF} relates to the crystallinity of the ferrihydrite samples and suggests that lattice defects, such as isomorphic substitutions and lattice

vacancies, are introduced with the incorporation of arsenic both by equilibration and coprecipitation.[48] These results compliment the XRD and EXAFS and support the conclusion that the incorporation of arsenate by coprecipitation causes structural changes and decreased crystallinity.

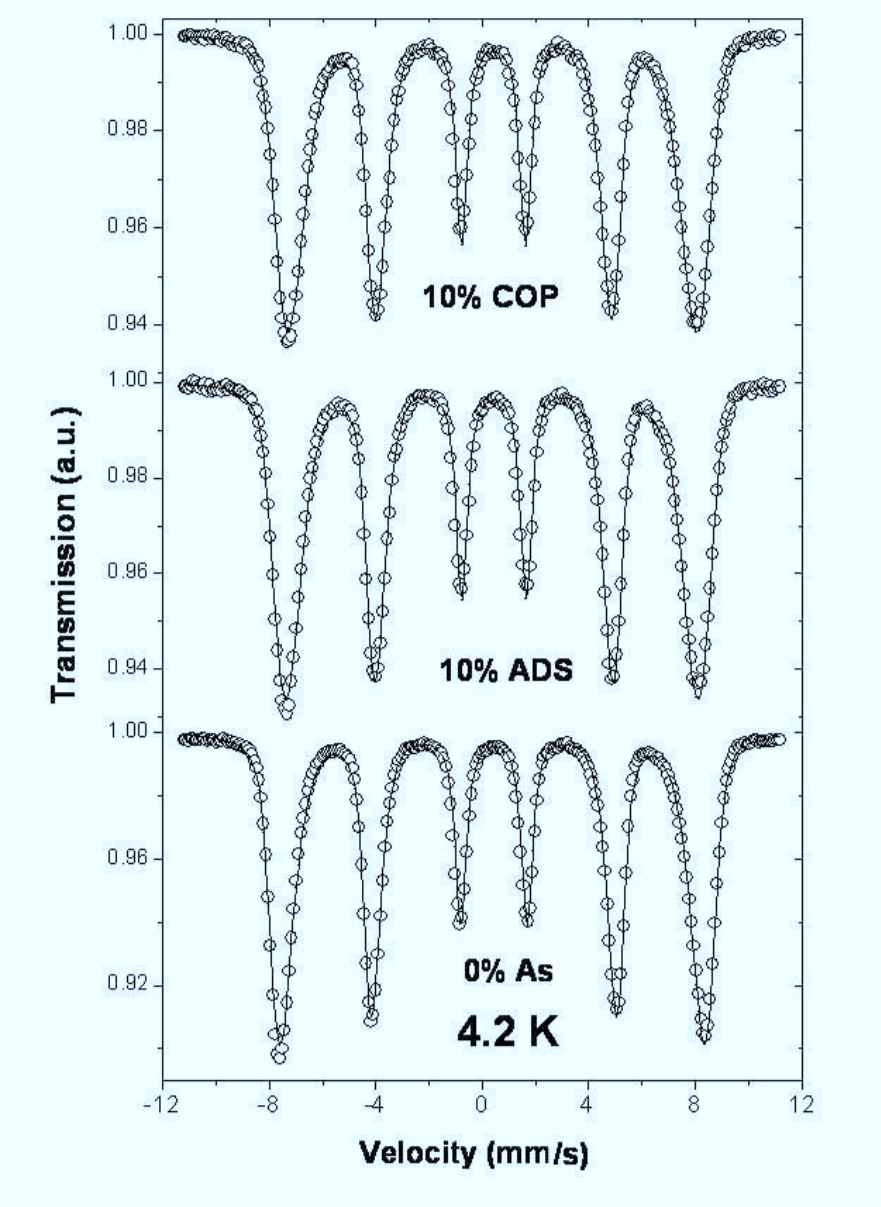

Figure 4.6 Mössbauer spectra at 4.2 K for 10% COP, 18-day 10% ADS, and 0% As ferrihydrite samples. Lines represent the best fit of experimental data (circles).

Table 4.4 Maximum hyperfine field (B_{HF}), quadrupole splitting (QS), and isomer shift (IS) of 0% As, 10% ADS, and 10% COP ferrihydrite samples at 4.2 K.

sample	B_{HF} (T)	QS (mm/s)	IS (mm/s)
0% As	49.6 ± 0.2	-0.07 ± 0.01	0.46 ± 0.01
10% ADS (18-day)	48.5 ± 0.2	-0.08 ± 0.01	0.53 ± 0.01
10% COP	47.9 ± 0.2	-0.03 ± 0.01	0.54 ± 0.02

4.4.4 *Potentiometric Titrations*

The data from potentiometric titrations of the 0% As and 10% COP suspensions are shown in Figure 4.7. The point of zero net proton charge (PZNPC) was pH 8.8 ±0.1 for the 0% As sample and pH 6.3 ±0.1 for the 10% COP sample. Experiments to determine the PZNPC of 1-day and 18-day 10% ADS ferrihydrite were complicated by the influence of CO_2 and desorption of arsenate with the increasing pH of the titration procedure. However, the semi-quantitative titration results clearly indicate a PZNPC greater than 10.5 for both samples (results not shown). This is consistent with the prediction of Dzombak and Morel[29] regarding an increase in the PZNPC due to co-adsorption of arsenate, protons, and sodium (as determined by ICP-AES analysis). The coprecipitation of arsenic had the opposite effect and shifted the PZNPC to a lower pH as compared to the 0% As sample. Few studies have considered the effect on PZNPC with coprecipitation of ions, but the shift to lower pH parallels the effect observed by Mikutta et al.,[49] in which acid polysaccharides were coprecipitated with ferrihydrite. Electrophoretic mobility experiments determined the isoelectric point of pure ferrihydrite to be near pH 7 and the isoelectric point of the coprecipitated-acid polysaccharide ferrihydrites was less than 2.

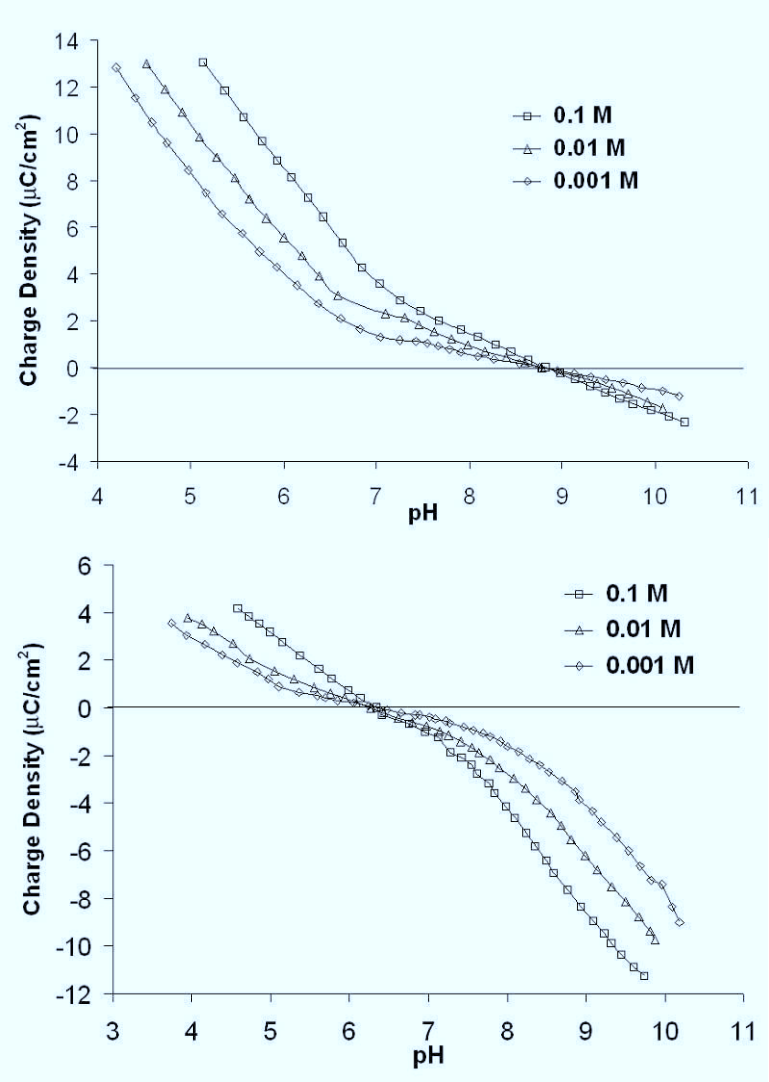

Figure 4.7 Potentiometric titrations results for 0% As (upper) and 10% COP (lower) ferrihydrite with surface charge density as a function of pH at different ionic strengths.

In summary, the six-line ferrihydrite samples all have similar average particle size, and their XRD patterns are consistent with six-line ferrihydrite. However, the 10% COP sample exhibits a lower degree of crystallinity, as evidenced by the results from XRD, magnetic characterization, and EXAFS. It is also possible that the 10% COP crystallite size may be smaller than for the other samples, which would be consistent with the conclusions of Waychunas.[20,42] However, the consistent aspect ratio and size

distribution over all samples makes this an unlikely possibility. Finally, the results from characterization of the 10% ADS samples suggest that arsenate initially adsorbs to ferrihydrite but that incorporation of arsenate into the ferrihydrite structure does occur.

4.4.5 *Kinetic Reactions*

The reductive dissolution was monitored for the arsenic-bearing and 0% As ferrihydrite powders. During the reaction, hydroquinone (QH_2) is oxidized and ferric iron reduced to produce benzoquinone (Q) and ferrous iron (eqs 2-4). The rate of reaction can be measured by monitoring the benzoquinone and Fe(II) concentrations as a function of time.

$$2Fe_5HO_8{\bullet}4H_2O(s) + 10e^- + 30H^+(aq) \rightarrow 10Fe^{2+}(aq) + 24H_2O(l) \quad (2)$$

$$5QH_2(aq) \rightarrow 5Q(aq) + 10e^- + 10H^+(aq) \quad (3)$$

$$2Fe_5HO_8{\bullet}4H_2O(s) + 5QH_2(aq) + 20H^+(aq) \rightarrow 10Fe^{2+}(aq) + 5Q(aq) + 24H_2O(l) \quad (4)$$

Using the method of initial rates,[50] the rate was determined using the first 3-7 data points from each trial (9-21 points for each sample). The concentration of benzoquinone versus reaction time is presented in Figure 4.8 for five ferrihydrite samples with 2.0 g/L ferrihydrite loading and 0.2 mM hydroquinone at 25 ±1 ºC. With the exception of the 18-day 10% ADS sample, the reductive dissolution rates are statistically indistinguishable. The significantly lower reaction rate of the 10% ADS sample, approximately one-fifth the rate of the other four samples, suggests that the high concentration of arsenic on the particle surface inhibits the redox reaction. Using the calculated surface area for the 10% ADS sample from Table 4.2 combined with the elemental analysis and a reactive surface site density of 17 μmol sites/g,[29] one can

estimate the fraction of sites occupied by arsenate. Assuming a 1:1 stoichiometry (i.e., one arsenic per reactive surface site) and that all of the arsenic is located on reactive surface sites yields an estimate that 20% of the reactive sites are bound to arsenate. However, the rate of reduction of 10% ADS is reduced by 80% as compared to the other four samples. One hypothesis for this dramatic drop in reactivity with such modest surface coverage is that arsenate preferentially adsorbs at the most reactive surface sites.

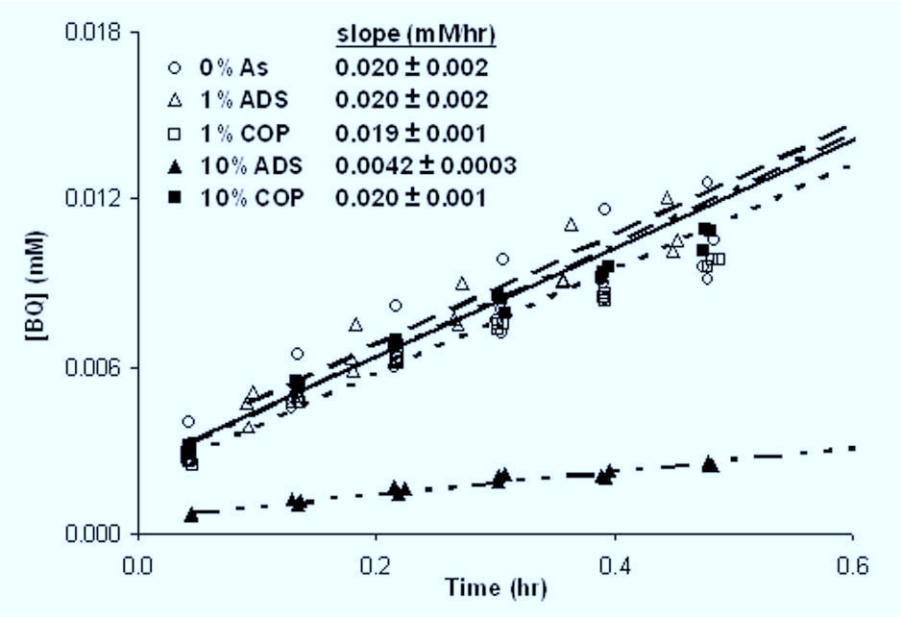

Figure 4.8 Benzoquinone concentration versus time for reactions with 0.2 mM hydroquinone and 2 g/L ferrihydrite loading at 25 ±1 ºC. The trendlines are extended beyond the linear data and represent 0% As (——), 1% ADS (– – –), 1% COP (·····), 18-day 10% ADS (–··–), and 10% COP (–·–·). The slope and standard error (mM/hr) of each trendline are given to the right of each sample label.

The distinct decrease in reactivity of 18-day 10% ADS warranted further kinetic experiments to investigate the empirical rate law and quantify the activation energy for the reductive dissolution of the 10% ADS ferrihydrite compared to the 10% COP and

0% As samples. Reaction orders were determined for the 0% As, 18-day 10% ADS, and 10% COP samples, and the results are reported in Table 4.5.

Table 4.5 Reaction orders of hydroquinone (*m*) and surface area (*n*) of 0% As, 10% ADS, and 10% COP samples. Initial rates for ferrihydrite reactions at room temperature with 0.2 mM hydroquinone and 2 g/L oxide loading.

sample	*m*	*n*	initial rate (mM hr^{-1})
0% As	0.26 ± 0.02	0.65 ± 0.08	0.020 ± 0.002
10% ADS (18-day)	0.62 ± 0.09	0.89 ± 0.07	0.0042 ± 0.0003
10% COP	0.37 ± 0.07	0.64 ± 0.15	0.020 ± 0.001

Rate constants were calculated using the measured rate of reaction and experimental orders with respect to hydroquinone and the particle surface area (S) concentrations according to the empirical rate law

$$\frac{d[\mathrm{Q}]}{dt} = k[\mathrm{QH_2}]^m[\mathrm{S}]^n \qquad (5)$$

where *k* is the rate constant, and *m* and *n* are the empirical orders with respect to hydroquinone and surface area, respectively. Because all experiments were performed at a buffered pH of 3.75, the proton concentration has been incorporated into the rate constant. Over the reaction period studied, less than 0.2% of the total Fe(III) was reduced; hence, there was no significant change in the particle surface area concentration. The reaction orders for 0% As and 10% COP are similar, although *m* is statistically larger for 10% COP than for 0% As. However, the reaction orders for 18-day 10% ADS are substantially different, suggesting a significant change in reaction mechanism as a consequence of the adsorption of arsenate. This could result from the preferential adsorption of arsenate onto one type of reactive surface site or simply indicate a change in the overall mechanism of reductive dissolution for the 18-day 10%

ADS ferrihydrite due to the presence of adsorbed arsenate. The very modest difference in *m* observed for 10% COP is maybe the result of a portion of the arsenate residing on the ferrihydrite surface.

To quantify the activation energy of reductive dissolution, the kinetic data for each sample were collected at four or five temperatures (2.0-50.0 ºC) and evaluated using the Arrhenius equation (eq 6).

$$\ln k = \ln A - \frac{E_a}{RT} \tag{6}$$

Plotting ln *k* against 1/*T* produced a linear trend, from which the pre-exponential factor (*A*) and the activation energy (E_a) were calculated.[50] To calculate rate constants, reaction orders were assumed to be independent of particle size and reaction temperature.[30,51] The Arrhenius plots for the 0% As, 10% COP, and 18-day 10% ADS, samples are shown in Figure 4.9. Arrhenius parameters calculated using linear regression analysis are reported with standard errors in the table embedded within Figure 4.9. The activation energies of the 0% As, 18-day 10% ADS, and 10% COP samples (40.7, 39.9, and 36.8 kJ/mol, respectively) are similar and statistically indistinguishable. Due to variation in *m* and *n* used to calculate rate constants for the three samples, the *A* values cannot be interpreted. Thus, comparison of initial rates for identical reaction conditions (Figure 4.8) provides the most elucidative comparison. These results reveal that although the XRD, EXAFS, and magnetism characterization results demonstrate that there are structural effects with the adsorption and coprecipitation of arsenate, the activation energy of the rate-determining step for reductive dissolution does not vary.

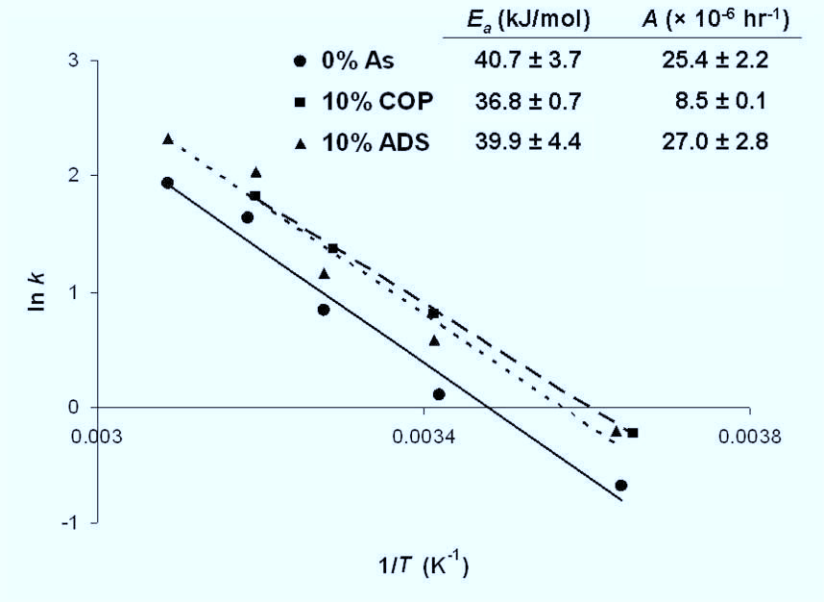

Figure 4.9 Arrhenius plot of reactions with 0.2 mM hydroquinone and 2 g/L ferrihydrite loading, including the trendlines representing 0% As (——), 18-day 10% ADS(·····), and 10% COP (– – –) ferrihydrites.

According to Zinder et al.,[52] the rate of proton-promoted reductive dissolution ($R_{e,H}$) for iron oxides is dependent on the surface concentration (E) of potentially detachable surface metal species per area as described by eq 7,

$$R_{e,H} = \frac{d[\mathrm{M(II)}]}{dt} = k\{E\} \tag{7}$$

and E is statistically related to the probability of finding a reduced, surface metal center with two protonated nearest-neighbor oxide or hydroxide sites. Real oxide surfaces have different kinds of surface sites, including surface defects, kinks, steps, and pits, with varying activation energies.[53] Dissolution occurs at the sites with the lowest activation energies, which are called active sites. The detachment of M(II) at active sites and less active sites are parallel reactions but reaction at the most active sites is dominant and rate determining.[52] The adsorption of arsenate leads to an increase in surface

protonation as indicated by the increase in PZNPC; however, the presence of arsenate at the surface decreases the sites available for protons to adsorb. Arsenate forms binuclear bridging surface complexes and essentially extends the cross-linking of the solid's lattice. For dissolution at binuclear arsenate adsorption sites, the activation energy is high because dissolution requires the simultaneous removal of two metal centers.[54] Paige et al. observed marked decreases in proton-promoted dissolution rates when arsenate (3-50 mol%) was coprecipitated into ferrihydrite solids.[55] And Rea et al. documented a 50% decrease in labile Fe sites for Fe^{59}-isotope exchange for ferrihydrite with arsenate adsorbed on 32% of the sites.[56] These published results demonstrate that not all surface sites—only active surface sites—must be blocked to have a pronounced effect on the kinetics of surface reactions. In this body of work, the adsorption of arsenate on one-fifth of the surface sites of 10% ADS produced an 80% drop in the reaction rate for reductive dissolution. The similarity of E_a for 0% As, 10% COP, and 10% ADS indicates that the rate determining step is unaffected by the structural defects within crystallites/particles or the presence of arsenate on the ferrihydrite surface. However, the reaction orders for the 10% ADS rate law differed from the other two samples, indicating a change in reaction mechanism or, more likely, a change in the relative importance of the parallel reactions at each type of reactive site. Arsenate at the most reactive sites would prevent those sites from participating in the reductive dissolution, and the reaction orders of 10% ADS may reflect that the reaction at less active sites dominates as a consequence of arsenate occupying the most active sites.

Arsenate is an important species to consider when studying the kinetics for reductive dissolution of the arsenic-bearing ferrihydrite samples; because, in addition to

iron, the arsenate ion (AsO_4^{3-}) is redox active (eq 8) and may be reduced to arsenite (AsO_3^{3-}) during reductive dissolution.

$$H_3AsO_4(aq) + 2H^+(aq) + 2e^- \rightarrow H_3AsO_3(aq) + H_2O(l) \quad E^o = 0.575\ V \qquad (8)$$

In this study, attempts to quantify arsenite and arsenate using the molybdene-blue method[40] were unsuccessful. As an alternative, kinetic experiments were conducted using the Ferrozine assay[39] to investigate the Fe(II):benzoquinone stoichiometry during reductive dissolution of arsenic-bearing ferrihydrites. The aqueous Fe(II) and benzoquinone concentrations of filtered solutions from reductive dissolution experiments using 18-day 10% ADS and 10% COP were measured. The method of initial rates was used to quantify the rate of Fe(II) and benzoquinone formation (Table 4.6). The slopes (in meq/L) cannot be differentiated for either sample and implies that no significant reduction of arsenate occurred during the reaction period. If arsenate reduction occurred and dominated the reaction, the expected rate of benzoquinone formation would be considerably higher than the stoichiometric rate of Fe(II) formation.

Table 4.6 Rates of benzoquinone and Fe(II) formation for the reductive dissolution of 10% ADS and 10% COP ferrihydrites for reactions at room temperature with 0.05 mM hydroquinone and 2 g/L oxide loading.

sample	benzoquinone slope (meq $L^{-1}hr^{-1}$)	Fe(II) slope (meq $L^{-1}hr^{-1}$)
10% ADS (18-day)	0.0049 ± 0.0020	0.0050 ± 0.0007
10% COP	0.030 ± 0.002	0.032 ± 0.003

To gain insight on arsenic release from the As-bearing materials, the samples were reacted for longer periods and with higher concentrations of hydroquinone. The release of iron and arsenic was monitored for four days during the reductive dissolution

of 10% COP and 18-day 10% ADS samples (Table 4.7). The most notable distinction is the almost one order of magnitude difference in the final amount of arsenic released from the two solids. In the case of 10% COP the release of Fe far outpaces that of As, but the opposite is true for 18-day 10% ADS. After 95 hours of reaction, approximately 12% of the total iron and less than 0.7% of the total arsenic were dissolved from the original 10% COP ferrihydrite solid. These results indicate that (1) arsenate remains incorporated in the ferrihydrite lattice and possibly (2) dissolved arsenate slowly readsorbs onto the ferrihydrite surface. In contrast, 5% of the total iron and about 4% of the total arsenic were dissolved from 10% ADS (18-day). About 2% of the arsenic was released just by resuspension and equilibration of the 10% ADS sample with the buffer solution overnight. The release of arsenate during equilibration was not expected because samples were resuspended at pH 3.75, which was similar to the 10% ADS suspension pH before drying. A modest drop in dissolved arsenate concentration was observed after 95 hours, which was attributed to the readsorption of some arsenate onto ferrihydrite. For these high-yield dissolution experiments, the concentrations of iron measured by ICP-AES were similar to concentrations measured using the Ferrozine method. The formation of Fe(II) closely matched the stoichiometic formation of benzoquinone (2:1 as can be seen in eq 4) for the 10% COP reactions but was slightly lower for the 18-day 10% ADS reactions. Therefore, a small fraction of the arsenate (<2% of total) from the 10% ADS samples may have reduced during the reaction period.

Table 4.7 Percentages of dissolved Fe and As compared to the total amount contained in the ferrihydrite solids for equilibrium and filtrate samples of a long-term reductive dissolution reaction.

aliquot	10% ADS (18-day)		10% COP	
	Fe dissolved (wt.%)	As dissolved (wt.%)	Fe dissolved (wt.%)	As dissolved (wt.%)
blank	0.020	1.92	0.039	<0.145
1.5 hr	0.714	3.07	1.37	0.117
19 hr	3.25	4.33	7.53	0.567
95 hr	5.18	3.70	12.4	0.667

These results demonstrate that arsenic can be released from arsenic-bearing ferrihydrite prepared both by coprecipitation and adsorption, but the release from the ferrihydrite with adsorbed arsenate is substantially greater than from ferrihydrite with coprecipitated arsenate. These results suggest that understanding the mode of arsenic incorporation- either by coprecipitation or adsorption- could lead to improved predictions regarding arsenic release from naturally occurring arsenic-bearing iron oxides under reducing conditions.

4.5 Conclusions

Structural results indicate that the incorporation of arsenic by coprecipitation leads to decreased crystallinity. The results from reductive dissolution experiments show similar reaction rates, reaction mechanism, and activation energy for ferrihydrite precipitated with or without added arsenate. However, a marked decrease in reaction rate was observed ferrihydrite after equilibrium with an arsenate solution. The decrease is not attributed to differences in activation energy but rather the preferential blocking of active sites on the ferrihydrite surface, which also affects the rate law for reductive dissolution.

This body of work demonstrates that indeed strongly reducing conditions in groundwater systems may be linked to the large-scale release of arsenic by reductive dissolution of arsenic-bearing ferrihydrite and likely of other arsenic- bearing iron oxide aquifer materials. Arsenic may be released by ferrihydrite materials prepared by either coprecipitation or adsorption of arsenate. However, under these reaction conditions, release from materials with adsorbed arsenate greatly exceeds that from materials with coprecipitated arsenate. In fact, a considerable amount of arsenic was released from 10% ADS ferrihydrite before the initiation of reductive dissolution. Therefore, characterization of arsenate-bearing iron oxides to determine the mode of arsenate incorporation—perhaps by quantification of Fe-Fe coordination with EXAFS spectroscopy—may lead to improved predictions of the large-scale release of arsenic within aquifer systems under reducing conditions.

4.6 Acknowledgements

This work was supported by the National Science Foundation EAR-0311869 (S.K. Banerjee, PI; R.L. Penn, Co-PI), the National Science Foundation Career Grant 0346385 (R.L Penn), the IGERT Program of the National Science Foundation under Award Number DGE-0114372 (fellowship to J.J.E.), and the University of Minnesota. The Institute for Rock Magnetism (IRM) is funded by NSF and the W. M. Keck Foundation, the Earth Science Division of the US National Science Foundation, and the University of Minnesota. This is IRM publication # 0803. TEM characterization was completed at the Characterization Facility, University of Minnesota, which receives support from NSF through the National Nanotechnology Infrastructure Network. This research was funded in part by the National Science Foundation, (BES-0608646 and

EF-0830093), and the U.S. EPA R833326. Portions of this research were carried out at the Stanford Synchrotron Radiation Laboratory, a national user facility operated by Stanford University on behalf of the U.S. Department of Energy, Office of Basic Energy Sciences. We thank Dr. Chris Kim, James Dale, and John Stegemeier of Chapman University for sample preparation and analysis support, as well as the staff and beamline scientists at SSRL.

4.7 References

1. Bennett, B.; Dudas, M. J. Release of arsenic and molybdenum by reductive dissolution of iron oxides in a soil with enriched levels of native arsenic. *Journal of Environmental Engineering and Science* **2003** 2, 265.

2. Smedley, P. L.; Kinniburgh, D. G. A review of the source, behavior and distribution of arsenic in natural waters. *Applied Geochemistry* **2002** 17, 517.

3. Sparks, D. L., *Environmental Soil Chemistry*. 2nd ed.; Academic Press: Amsterdam, 2003.

4. Appello, C. A. J.; van der Weiden, M. J. J.; Tournassat, C.; Charlet, L. Surface complexation of ferrous iron and carbonate on ferrihydrite and the mobilization of arsenic. *Environmental Science and Technology* **2002** 36, 3096.

5. Pichler, T.; Veizer, J.; Hall, G. E. M. Natural input of arsenic into a coral-reef ecosystem by hydrothermal fluids and its removal by Fe(II) Oxyhydroxides. *Environmental Science and Technology* **1999** 33, 1373.

6. Rancourt, D. G.; Fortin, D.; Pichler, T.; Thibault, P.-J.; Lamarche, G.; Morris, R. V.; Mercier, P. H. J. Mineralogy of a natural As-rich hydrous ferric oxide coprecipitate formed by mixing of hydrothermal fluid and seawater:

Implications regarding surface complexation and color banding in ferrihydrite deposits. *American Mineralogist* **2001** 86, 834.

7. Ford, R. G.; Bertsch, P. M.; Farley, K. J. Changes in transition and heavy metal partitioning during hydrous iron oxide aging. *Environmental Science and Technology* **1997** 31, 2028.

8. Chun, C. L.; Penn, R. L.; Arnold, W. A. Kinetic and microscopic studies of reductive transformations of organic contaminants on goethite. *Environmental Science and Technology* **2006** 40, 3299.

9. Stipp, S. L. S.; Hansen, M.; Kiristensen, R.; Hochella, M. F., Jr.; Bennedsen, L.; Dideriksen, K.; Balic-Zunic, T.; Leonard, D.; Mathieu, H.-J. Behaviour of Fe-oxides relevant to contaminant uptake in the environment. *Chemical Geology* **2002** 190, 321.

10. Straub, K. L.; Benz, M.; Schink, B. Iron metabolsim in anoxic environments at near neutral pH. *FEMS Microbiology Ecology* **2001** 34, 181.

11. LaKind, J. S.; Stone, A. T. Reductive dissolution of goethite by phenolic reductants. *Geochimica et Cosmochimica Acta* **1989** 53 (5), 961.

12. Scott, D. T.; McKnight, D. M.; Blunt-Harris, E. L.; Kolesar, S. E.; Lovley, D. R. Quinone moieties act as electron acceptors in the reduction of humic substances by humics-reducing microorganisms. *Environmental Science and Technology* **1998** 32, 2984.

13. Pederson, H. D.; Postma, D.; Jakobsen, R. Release of arsenic associated with the reduction and transformation of iron oxides. *Geochimica et Cosmochimica Acta* **2006** 70, 4116.

14. Jambor, J. L.; Dutrizac, J. E. Occurrence and constitution of natural and synthetic ferrihydrite, a widespread iron oxyhydroxide. *Chemical Reviews* **1998** 98, 2549.

15. Cornell, R. M.; Schwertmann, U., *The Iron Oxides: Structure, Properties, Reactions, Occurrences and Uses*. 2nd ed.; Wiley-VCH: Weinheim, 2003.

16. Penn, R. L.; Tanaka, K.; Erbs, J. J. Size dependent kinetics of oriented aggregation. *Journal of Crystal Growth* **2007** 309, 91.

17. Stumm, W.; Morgan, J. J., *Aquatic Chemistry, Chemical Equilibria and Rates in Natural Waters*. 3rd ed.; John Wiley & Sons, Inc.: New York, 1996.

18. Waychunas, G. A.; Rea, B. A.; Fuller, C. C.; Davis, J. A. Surface chemistry of ferrihydrite: Part 1. EXAFS studies of the geometry of coprecipitated and adsorbed arsenate. *Geochimica et Cosmochimica Acta* **1993** 57, 2251.

19. Manceau, A. The mechanism of anion adsorption on iron oxides: Evidence for the bonding of arsenate tetrahedra on free Fe(O,OH)6 edges. *Geochimica et Cosmochimica Acta* **1995** 59, 3647.

20. Waychunas, G. A.; Davis, J. A.; Fuller, C. C. Geometry of sorbed arsenate on ferrihydrite and crystalline FeOOH: Revaluation of EXAFS results and topological factors in prediction sorbate geometry and evidence for monodentate complexes. *Geochimica et Cosmochimica Acta* **1995** 59, 3655.

21. Sherman, D. M.; Randall, S. R. Surface complexation of arsenic(V) to iron(III) (hydro)oxides: Structural mechanism from ab initio molecular geometries and EXAFS spectroscopy. *Geochimica et Cosmochimica Acta* **2003** 67 (22), 4223.

22. Guyodo, Y.; Banerjee, S. K.; Penn, R. L.; Burleson, D.; Berquó, T. S.; Seda, T.; Solheid, P. Magnetic properties of synthetic six-line ferrihydrite nanoparticles. *Physics of the Earth and Planetary Interior* **2006** 154, 222.

23. Duarte, E. L.; Itri, R.; Lima, E.; Baptista, M. S.; Berquó, T. S.; Goya, G. F. Large magnetic anisotropy in ferrihydrite nanoparticles synthesized from reverse micelles. *Nanotechnology* **2006** 17, 5549.

24. Punnoose, A.; Phanthavady, T.; Seehra, M. S.; Shah, N.; Huffman, G. P. Magnetic properties of ferrihydrite nanoparticles doped with Ni, Mo, and Ir. *Physical Review B* **2004** 69, 054425.

25. Stevens, J. G.; Khasanov, A. M.; White, M. S. G. Ferrihydrite Modification by Boron Doping. *Hyperfine Interactions* **2003** 151/152, 283.

26. Berquó, T. S.; Banerjee, S. K.; Ford, R.; Penn, R. L.; Pichler, T. High crystallinity Si-ferrihydrite: An insight into its Néel temperature and size dependence of magnetic properties. *Journal of Geophysical Research B: Solid Earth* **2007** 112, B02102.

27. Gilles, C.; Bonville, P.; Wong, K. K. W.; Mann, S. Non-Langevin behaviour of the uncompensated magnetization in nanoparticles of artificial ferritin. *European Physical Journal B* **2000** 17, 417.

28. Kim, B. J.; Lee, H. I.; Cho, S.-B.; Yoon, S.; Suh, B. J.; Jang, Z. H.; St. Pierre, T. G.; Kim, S.-W. Magnetic properties of artificially synthesized ferritins. *Journal of Applied Physics* **2005** 97, 10M524.

29. Dzombak, D. A.; Morel, F. M. M., *Surface Complexation Modeling: Hydrous Ferric Oxide*. 1st ed.; Wiley-Interscience: New York, 1990.

30. Jentzsch, T. L.; Penn, R. L. Influence of aluminum doping on ferrihydrite nanoparticle reactivity. *Journal of Physical Chemistry B* **2006** 110, 11746.

31. Webb, S. M. *Sam's Interface for XAS Analysis Package* 0.60.

32. Zabinsky, S. I.; Rehr, J. J.; Ankudinov, A.; Albers, R. C.; Eller, M. J. Multiple-scattering calculations of X-ray-absorption spectra. *Physical Review B* **1995** 52 (4), 2995.

33. Kim, C. S.; Lentini, C. J.; Waychunas, G. A., Synchrotron-based studies of metal adsorption and structural incorporation with iron oxyhydroxide nanoparticles. In *Adsorption of Metals by Geomedia II: Variables, Mechanisms, and Model Applications*, 1st ed.; Barnett, M., Elsevier Academic Press: 2008.

34. Kim, C. S.; Rytuba, J. J.; Brown, G. E. EXAFS study of mercury(II) sorption to Fe- and Al-(hydr)oxides: I. Effects of pH. *Journal of Colloid and Interface Science* **2004** 271, 1.

35. Waychunas, G. A.; Brown, G. E.; Apted, M. J. X-ray K-edge absorption-spectra of Fe minerals and model compounds. 2. EXAFS. *Physics and Chemistry of Minerals* **1986** 13 (1), 31.

36. Gilbert, B.; Lu, G.; Kim, C. S. Stable cluster formation in aqueous suspensions of iron oxyhydroxide nanoparticles. *Journal of Colloid and Interface Science* **2007** 313 (1), 152.

37. Kung, K.-H.; McBride, M. B. Electron transfer processes between hydroquinone and iron oxides. *Clays and Clay Minerals* **1988** 36 (4), 303.

38. Anschutz, A. J.; Penn, R. L. Reduction of crystalline iron(III) oxyhydroxides using hydroquinone: Influence of phase and particle size. *Geochemical Transactions* **2005** 6 (3), 60.

39. Stookey, L. L. Ferrozine-A New Spectrophotometric Reagent for Iron. *Analytical Chemistry* **1970** 42 (7), 779.

40. Lenoble, V.; Deluchat, V.; Serpaud, B.; Bollinger, J.-C. Arsenite oxidation and arsenate determination by the molybdene blue method. *Talanta* **2003** 61, 267.

41. Fuller, C. C.; Davis, J. A.; Waychunas, G. A. Surface chemistry of ferrihydrite: Part 2. Kinetics of arsenate adsorption and coprecipitation. *Geochimica et Cosmochimica Acta* **1993** 57, 2271.

42. Waychunas, G. A.; Fuller, C. C.; Rea, B. A.; Davis, J. A. Wide angle X-ray scattering (WAXS) study of "two-line" ferrihydrite structure: Effect of arsenate sorption and counterion variation and comparison with EXAFS results. *Geochimica et Cosmochimica Acta* **1996** 60 (10), 1765.

43. Brown, G. E.; Calas, G.; Waychunas, G. A.; Petiau, J. X-ray absorption spectroscopy and its applications in mineralogy and geochemistry. *Reviews in Mineralogy* **1988** 18, 431.

44. Dormann, J. L.; Fiorani, D.; Tronc, E., Magnetic Relaxation in fine-particle systems. In *Advances in Chemical Physics*, 1st ed.; Prigogine, I.; Rice, S. A., John Wiley & Sons, Inc.: 1997; 98.

45. Frandsen, C.; Mørup, S. Inter-particle interactions in composites of antiferromagnetic nanoparticles. *Journal of Magnetism and Magnetic Materials* **2003** 266, 36.

46. Berquó, T. S.; Erbs, J. J.; Lindquist, A.; Penn, R. L.; Banerjee, S. K. Effects of magnetic interactions in antiferromagnetic ferrihydrite particles. *Journal of Physics: Condensed Matter* **2009** 21, 176005.

47. O'Reilly, W., *Rock and Mineral Magnetism*. 1st ed.; Blackie: Glasgow, 1984.

48. Murad, E.; Cashion, J., *Mössbauer spectroscopy of environmental materials and their industrial utilization*. 1st ed.; Kluwer Academic Publishers: Boston, 2004.

49. Mikutta, C.; Mikutta, R.; Bonneville, S.; Wagner, F.; Voegelin, A.; Christl, I.; Kretzschmar, R. Synthetic coprecipitates of exopolysaccharides and ferrihydrite. Part I: Characterization. *Geochimica et Cosmochimica Acta* **2008** 72, 1111.

50. Espenson, J. H., *Chemical Kinetics and Reaction Mechanisms*. 2nd ed.; McGraw-Hill: New York, 2002.

51. Anschutz, A. J. Reactivity of iron oxyhydroxide nanoparticles: Effects of physical variables. Doctor of Philosophy, University of Minnesota, Minneapolis, MN, 2006.

52. Zinder, B.; Furrer, G.; Stumm, W. The coordination chemistry of weathering: II. Dissolution of Fe(III) oxides. *Geochimica et Cosmochimica Acta* **1986** 50, 1861.

53. Wieland, E.; Wehrli, B.; Stumm, W. The coordination chemistry of weathering: III. A generalization on the dissolution rates of minerals. *Geochimica et Cosmochimica Acta* **1988** 52, 1969.

54. Biber, M. V.; dos Santos Afonso, M.; Stumm, W. The coordination chemistry of weathering: IV. Inhibition of the dissolution of oxide minerals. *Geochimica et Cosmochimica Acta* **1994** 58 (9), 1999.

55. Paige, C. R.; Snodgrass, W. J.; Nicholson, R. V.; Sharer, J. M. An arsenate effect on ferrihydrite dissolution kinetics under acidic oxic conditions. *Water Research* **1997** 31 (9), 2370.

56. Rea, B. A.; Davis, J. A.; Waychunas, G. A. Studies of the reactivity of the ferrihydrite surface by iron isotopic exchange and Mössbauer spectroscopy. *Clays and Clay Minerals* **1994** 42 (1), 23.

Chapter 5

Degradation of Carbon Tetrachloride by Zero-Valent Fe and Cu/Fe Particles

5.1 Chapter Summary

The kinetics of reductive degradation of carbon tetrachloride (CT), a model chlorinated organic contaminant, with zero-valent Fe and Cu/Fe particles were quantified. Pre- and post-reaction solids were characterized by inductively coupled plasma-atomic emission spectrometry (ICP-AES), powder X-ray diffraction (XRD), transmission electron microscopy (TEM), and scanning TEM with electron dispersive X-ray spectroscopy (EDS). Rietveld refinement of XRD data was used so as to enable quantitative comparison of solid-state products before and after reaction. The rates of CT degradation increased with the presence of copper, but concentrations of chloroform also increased, which is undesirable. Solid-state products formed during reduction of CT included magnetite, lepidocrocite, and goethite; and the presence of copper affected the distribution of solid-state products. The main solid-state product was magnetite for particles with little or no copper. Substantial goethite and lepidocrocite were produced from particles containing higher amounts of copper.

5.2 Introduction

Zero-valent iron (ZVI) has been found to be an effective reducing agent for reductive transformation of highly oxidized organic (e.g., chlorinated hydrocarbons) and inorganic (e.g., heavy metals) species. ZVI can reduce the concentrations and mobility of such substances in subsurface environments.[1,2] ZVI particles have an Fe^0 core that serves as the electron donor and active material for remediation of contaminated areas. Ideally, ZVI materials will increase the rate of contaminant degradation, influence the branching ratio to kinetically favor the less harmful degradation products, and allow for the complete oxidation of the Fe^0. Several sites have been remediated by the placement of permeable reactive barrier systems, where groundwater flows through an engineered wall of ZVI materials.[1] The dissolved groundwater contaminants are transformed, precipitated, or adsorbed by contact with the reactive ZVI. In other cases, colloidal particles less than 1 μm in diameter, and particularly nano-sized, ZVI can be suspended and injected into contaminated soil, sediment, or aquifer areas for treatment.[3,4]

Chlorinated hydrocarbons undergo reductive dechlorination in the presence of electron donors such as Fe^0 (eq 1), and the net reaction is often thermodynamically favorable.[5] Under anaerobic conditions, Fe^0 can corrode with water serving as an oxidant (eq 2).

$$Fe^0 + RCl + H^+ \rightarrow Fe^{2+} + RH + Cl^- \quad (1)$$

$$Fe^0 + H_2O \leftrightarrow Fe^{2+} + H_2 + 2OH^- \quad (2)$$

Therefore, the three major reducing species in Fe^0-H_2O systems are iron metal, Fe^{2+}, and hydrogen. The presence of these reductants suggests three pathways for dehalogenation of chlorinated organics.[5] The first employs the iron metal directly, with electron transfer from the Fe^0 surface to the adsorbed alkyl halide as described above. The second involves the water corrosion intermediate product Fe^{2+}, in solution or adsorbed on solids (eq 3). And the third employs hydrogen, the water corrosion product, in the presence of a catalyst (eq 4).

$$2Fe^{2+} + RX + H^+ \rightarrow 2Fe^{3+} + RH + X^- \quad (3)$$

$$H_2 + RX \rightarrow RH + H^+ + X^- \quad (4)$$

Chlorinated hydrocarbons are among the most prevalent contaminants in soils and groundwater.[6] Carbon tetrachloride (CT) is a toxic and carcinogenic compound, and as such, it is regulated under the Safe Water Drinking Act with a maximum contaminant level (MCL) of 5 ppb.[7] CT can be transformed by two main pathways under reducing conditions: hydrogenolysis and dichloroelimination.[7] Hydrogenolysis replaces the chlorine with hydrogen to produce chloroform, which can further degrade to dichloromethane. Dichloroelimination leads to completely dechlorinated products like carbon monoxide and formate through rapid hydrolysis of a dichlorocarbene intermediate. The branching ratio of the degradation reaction is important, and the formation of fully dechlorinated products is preferred because compounds such as chloroform and dichloromethane are toxic and carcinogenic contaminants in their own right.

ZVI prepared with metal additives have been found to enhance reactivity. In addition, the added metals could result in modified reaction mechanisms, which could in turn provide a route by which more desirable branching ratios could be controlled.[8-12] Noble metals like Pd on the ZVI surface oxidize less readily than Fe^0 and are preserved during redox reactions, but the mechanism of enhanced reactivity has not been determined.[2] Three hypotheses for the enhanced reactivity of bimetals are (1) the formation of a galvanic cell between iron and the metal additive, thereby inducing electron flow from iron to the more noble metal where reduction occurs, (2) the adsorption of atomic hydrogen on the additive surface where reaction predominantly occurs, and (3) the absorption of atomic hydrogen within the metal additive's lattice structure.[11] Metals such as Pd, Pt, Ni, and Ag have been the focus of many studies,[4,11-14] but the incorporation of Cu has piqued the interest of a few.[8,15-17] Copper is a noble metal and influences the rates and product ratios in Cu/Fe bimetal materials.[9] Although Cu as an additive does not enhance reactivity as well as Pd or Ni,[9,10] it may be more cost-effective to incorporate Cu rather than Pd. The presence of copper ions in systems with Fe^{II} associated with iron oxide surfaces has been shown to enhance the remediation of CT.[6,18] Furthermore, pure Cu metal is capable of reducing multiply-chlorinated hydrocarbons and CT.[19,20]

ZVI prepared with metal additives may have several different possible structures with the additive homogeneously or heterogeneously distributed throughout the particles or predominantly at the surface with homogenous or heterogeneous coverage. Galvanic deposition is the common method of incorporating the additive onto Fe^0 surfaces by exposure to a solution of the additive's sulfate or chloride salt, causing

metal deposition to form a coating.[3] The incorporation of the additive by coprecipitation in the ZVI starting material is not common but is expected to influence reactivity. Increases in Cu coverage up to a monolayer and monolayer thickness of Cu on granular iron have been shown to increase the reaction rates of bimetals in Bransfield et al.[8] The relative amount of additive on or within ZVI particles has been shown to affect reaction rates and the yield of fully dechlorinated products.[9]

In this study, ZVI samples prepared with various amounts of copper additive were systematically studied. ZVI samples were prepared by hydrogen reduction of ferrihydrites with up to 20 mol% of coprecipitated copper. Reaction rates and chloroform product yield were investigated using batch reactions with CT as the chlorinated hydrocarbon model compound. Fe and Cu/Fe zero-valent particles and post-reaction solids were characterized using inductively coupled plasma-atomic emission spectrometry (ICP-AES), powder X-ray diffraction (XRD), transmission electron microscopy (TEM), and scanning transmission electron microscopy with electron dispersive X-ray spectroscopy (STEM-EDS). Characterization results compliment the kinetic experiments to elucidate the effects of copper and its relative content on the reactivity of the ZVI bimetallic particles.

5.3 Experimental Methods

5.3.1 *Synthesis of Zero-Valent Iron Materials*

Solutions were prepared with 18MΩ•cm resistivity water (Milli-Q water, Millipore Corporation). All glassware and Nalgene bottles were acid washed with 4 M nitric acid and rinsed three times with Milli-Q water. Cu/Fe bimetals were prepared by the reduction of ferrihydrite precipitated from ferric nitrate solutions containing no or

specified concentrations of copper nitrate. Two-line ferrihydrite (2LF) was synthesized by a modified method from Schwertmann and Cornell.[21] The 2LF was prepared by dissolving 0.0495 mol of $Fe(NO_3)_3 \cdot 9H_2O$ in 250 mL of Milli-Q water. The solution was stirred vigorously with a Teflon-coated stir bar while 150 mL of 1.0 M KOH was added rapidly. Additional 1.0 M KOH solution was added dropwise to increase the pH to between 7 and 8. In a similar fashion, copper-doped 2LF samples prepared from solutions prepared with $Cu(NO_3)_2 \cdot 3H_2O$ and $Fe(NO_3)_3 \cdot 9H_2O$ salts, with 0.5, 3, 10, or 20 mol% of copper and maintaining 0.0495 mol of metal (Fe^{3+} and Cu^{2+}) overall. The two-line ferrihydrites were centrifuged (6000 rcf using an Eppendorf Centrifuge 5804) for 10 minutes, rinsed with Milli-Q water, and resuspended, a process repeated three times. The 2LF samples were transferred to Spectra-Por #7 dialysis bags (MWCO = 2000 g/mol) and dialyzed against Milli-Q water for two days at 10 ºC, changing the water at least six times.

Undoped six-line ferrihydrite (6LF) was prepared by addition of a 0.48 M $NaHCO_3$ solution to an equal volume of 0.40 M $Fe(NO_3)_3 \bullet 9H_2O$ solution. The copper-doped 6LF was prepared using a solution of $Cu(NO_3)_2 \cdot 3H_2O$ and $Fe(NO_3)_3 \cdot 9H_2O$ salts with a total metal concentration of 0.40 M. The base solution was added over 12 ±1 minutes using a Fisher peristaltic pump, and the mixture was stirred constantly using a Teflon-coated stir bar. Next, the suspension was microwave-annealed (950 Watt oven) at 30-second intervals until it boiled. The bottle containing the suspension was submerged into an ice bath until it cooled to room temperature, and the suspension was transferred to Spectra-Por #7 dialysis bags (MWCO = 2000 g/mol). Dialysis against

Milli-Q water was performed for three days at room temperature, changing the water at least nine times.

All 2LF and 6LF materials were air-dried for several days and then ground into powders using an agate mortar and pestle. Ferrihydrite powders were reduced in a quartz tube furnace under $H_2(g)$ flowing at 0.1 L min^{-1} at a temperature ramped from room temperature to 450 ºC at a rate of 5 ºC min^{-1} and a dwell time of 4 hr at the maximum temperature. After reduction, the materials were transferred to and stored in an anaerobic chamber (Coy Laboratories, 5% H_2/95% N_2). After preparation of the zero-valent materials and before completing any kinetic experiments, the anaerobic environment of the chamber was compromised. The materials were retreated in the quartz tube furnace under $H_2(g)$ following the same procedure as described.

5.3.2 *Kinetic Reactions*

The kinetics of carbon tetrachloride (CT) degradation were monitored by batch reaction in 123-mL serum bottles without headspace. In an anaerobic chamber, 150 mg of solid zero-valent sample was measured directly into the bottle. The reactions were initiated by adding a 150 μM CT solution prepared with pH 7.0 50 mM MOPS buffer. Bottles were capped with a PTFE-lined septum and an aluminum crimp cap and were covered with aluminum foil. After initial preparation, the reactors were removed from the anaerobic chamber and were mixed around their longitudinal axes on a Glas-Col rotator at a speed of 40 rpm at 22 ±2 ºC. Aliquots of the suspension were withdrawn at desired time intervals by parallel injection of deoxygenated buffer into the reactor, thereby preventing the introduction of headspace. The 0.5-mL samples were filtered using 0.2-μm nylon Acrodisc filters into 2.5-mL gas chromatography (GC) vials and

capped with PTFE-lined septa and aluminum crimp caps. For each zero-valent iron sample, a blank trial, which consisted of all components except the CT, was completed. For a subset of post-reaction and blank solutions, filtered aliquots were acidified and stored at 10 ºC until ICP-AES analysis of the dissolved Cu and Fe concentrations.

CT and chloroform (CF) were analyzed using headspace GC with flame ionization detection (Trace GC 2000, Thermoquest). After incubation at 40 ºC for 25 minutes, a 250 µL headspace sample was injected (splitless, 150 ºC) by an HS 2000 headspace autosampler (ThermoQuest) onto a GS-GasPro Column (30 m × 0.32 mm i.d., J&W Scientific) using He carrier gas at 60 kPa. The oven temperature was initially held at 40 ºC for 1 minute, increased to 130 ºC at a rate of 20 ºC/minute, increased to 210 ºC at a rate of 5 ºC/minute, increased to 240 ºC at a rate of 25 ºC/minute, and finally held for 1 minute at 240 ºC. The flame detector operated with a constant flow of 35 mL/min of hydrogen and 350 mL/min of air. The kinetic data of each trial were fit using the Scientist® Software Program (version 2.01) to determine the rate constants for the reactions of CT and CF.

Six-point calibration curves were used to determine experimental concentrations of CT and CF. Stock solutions were prepared by dilution of neat CT or CF (1 mL) into a 100-mL methanol solution. Standard solutions were prepared in serum bottles by dilution of an appropriate volume of methanol stock solution into 20 or 40 mL of 50 mM MOPS buffer (pH 7). The standard solutions were immediately capped with PTFE-lined septa and aluminum crimp caps. After 24 hours, 0.5-mL aliquots were transferred to 2.5-mL GC vials and capped with PTFE-lined septa and aluminum crimp caps. Standards were analyzed on the GC using the method described above.

5.3.3 *Materials Characterization*

ZVI (Fe and Cu/Fe) samples were characterized using inductively coupled plasma-atomic emission spectrometry (ICP-AES), powder X-ray diffraction (XRD), transmission electron microscopy (TEM), and scanning transmission electron microscopy with energy dispersive X-ray spectroscopy (STEM-EDS).

ICP-AES was employed to determine the concentration of copper in the ZVI materials. The solid samples (~30 mg) were digested with 2.0 mL of freshly prepared aqua regia, then diluted with 8.0 mL of Milli-Q water, and then further diluted with 0.1 M HNO_3. Analysis of Cu and Fe was completed using a Perkin Elmer Optima 3000DV ICP in radial or axial mode.

The phase compositions of ZVI materials and post-reaction materials were determined using powder XRD and Rietveld refinement of the diffraction patterns. XRD data were collected using a PANalytical X-Pert PRO MPD X-ray diffractometer equipped with a cobalt source and an X-Celerator detector over the range of 10-120º 2θ at a scan rate of 0.35º per minute. Each sample was protected from air exposure by using an air-tight sample holder. The diffraction patterns were compared to the reference powder diffraction files (PDF) for iron (#6-0696), copper (#1-1241), magnetite (#19-0629), goethite (#29-0713), and lepidocrocite (#1-0136). Data were plotted as the square root of the intensity to improve sensitivity for identification of the minor phase components. Quantitative phase composition of samples were determined by the Rietveld method[22] using X-Pert High Score Plus (version 2.0.1) software and the known crystal structure data[23-26] for the systematic refinement of all structures. The weighted profile residual factor (R_{wp}) values for refinement fits to experimental XRD

data were typically between 2.1 and 2.8, with only a few refinements with somewhat higher values that did not exceed 4.0, indicating a good fit to the experimental data.

High-resolution TEM was performed using an FEI Technai G^2 F30 at 300 kV. Dry powders were electrostatically mounted onto a 3 mm 200-mesh holey carbon-coated nickel grid (Structure Probe, Inc.). The TEM grids were prepared in an anaerobic chamber and stored in an air-tight container until mounted onto the TEM sample holder. All TEM images were collected using a Gatan charge-coupled device camera and analyzed using Gatan Digital Micrograph 3.8.2. Spectral images were collected by operating the microscope in scanning TEM (STEM) mode with EDS to map the distribution of Cu, Fe, and O in the particles. The microscope was operated at 300 kV with an extraction voltage of 4500 eV.

5.4 Results and Discussion

5.4.1 *Zero-Valent Iron Materials*

The copper content of the ZVI materials, hereafter referred to as ZVI_{2LF} or ZVI_{6LF} relative to the ferrihydrite synthesis method, as determined by ICP-AES is shown in Table 5.1. The 2LF coprecipitation synthesis method was effective for the incorporation of copper, as indicated by the good match between the metal ratio as measured and the mol% of copper in the ZVI materials matched well with the metal ratio in the initial aqueous the solution. The 6LF synthesis method was not as effective. The initial solution had 10 mol% Cu, but the solid product had only 0.08 mol% Cu. The higher final pH during the hydrolysis step of the 2LF synthesis (pH 7-8 as compared to pH 3 for 6LF synthesis) likely hydrolyzes and coprecipitates copper more effectively.

Table 5.1 Copper content of the ZVI materials determined by ICP-AES.

Sample	**Cu (mol %)**
0% Cu ZVI_{6LF}	BDL*
0.08% Cu ZVI_{6LF}	0.0787
0% Cu ZVI_{2LF}	BDL*
0.5% Cu ZVI_{2LF}	0.510
3% Cu ZVI_{2LF}	3.05
10% Cu ZVI_{2LF}	10.2
20% Cu ZVI_{2LF}	19.5

* BDL below the detection limit (near 10^{-2} mol%)

The XRD patterns of the ZVI materials are shown in Figure 5.1 with labels indicating the peak location of PDF reference patterns for Fe and Cu metals. All peaks within the patterns were matched to Fe and Cu. The presence of crystalline copper metal was detected in the 3 mol%, 10 mol% and 20 mol% ZVI 2LF with increasing peak intensity for higher copper content.

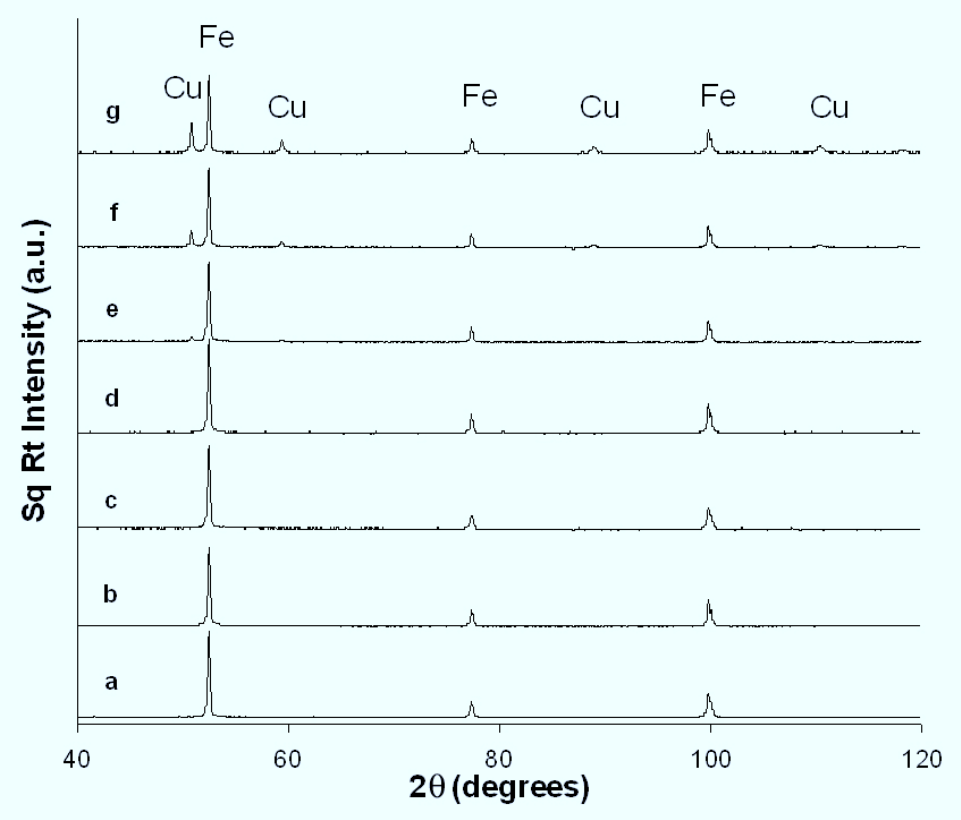

Figure 5.1 XRD patterns of ZVI materials with labeled peaks of Fe and Cu metal PDF reference patterns: (a) 0% Cu ZVI_{6LF}, (b) 0.08% Cu ZVI_{6LF}, (c) 0% Cu ZVI_{2LF}, (d) 0.5% Cu ZVI_{2LF}, (e) 3% Cu ZVI_{2LF}, (f) 10% Cu ZVI_{2LF}, and (g) 20% Cu ZVI_{2LF}.

Imaging with TEM revealed that the iron particles are somewhat spherical and range in size from several tens to a few hundred nanometers. In general, the particles are agglomerated. The copper metal occurred as small (ca. few to tens of nm) nanoparticles on the surface of the particles or as grains within the polycrystalline particles (Figures 5.2 and 5.3). In addition, the particles had a thin oxidation layer (ca. 3-5 nm thick) on the iron metal (Figure 5.2). No such corrosion layer was observed on the copper. This corrosion layer had the same thickness and appearance regardless of whether prevention of exposure to atmospheric oxygen was attempted.

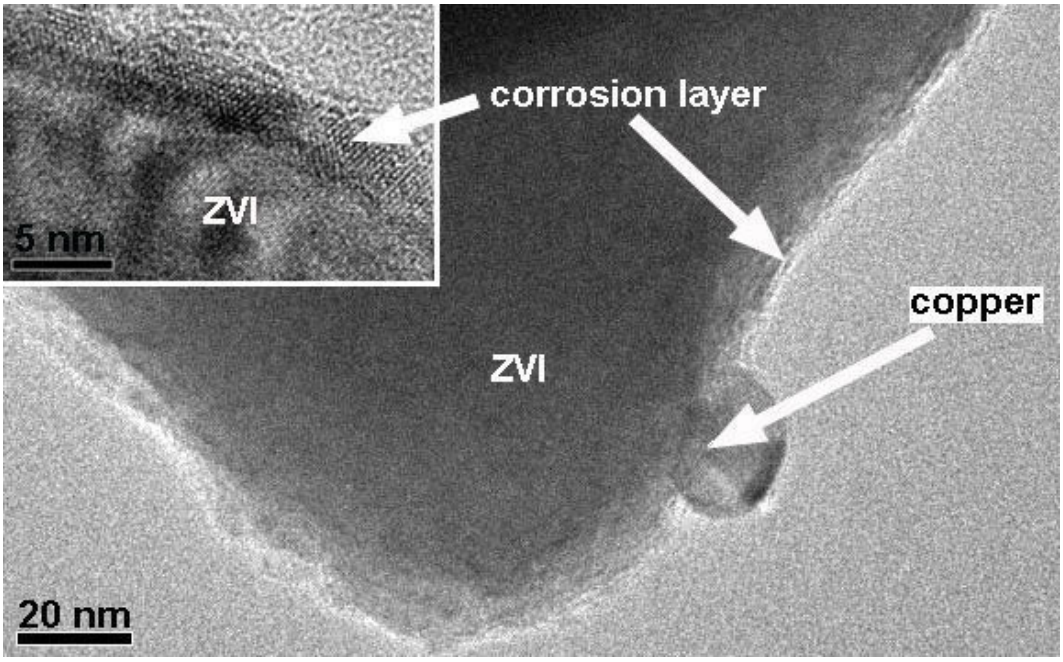

Figure 5.2 TEM micrograph of representative ZVI materials prepared with copper. The high-resolution image (inset) includes lattice fringes of Fe and a thin corrosion layer 3-5 nm thick.

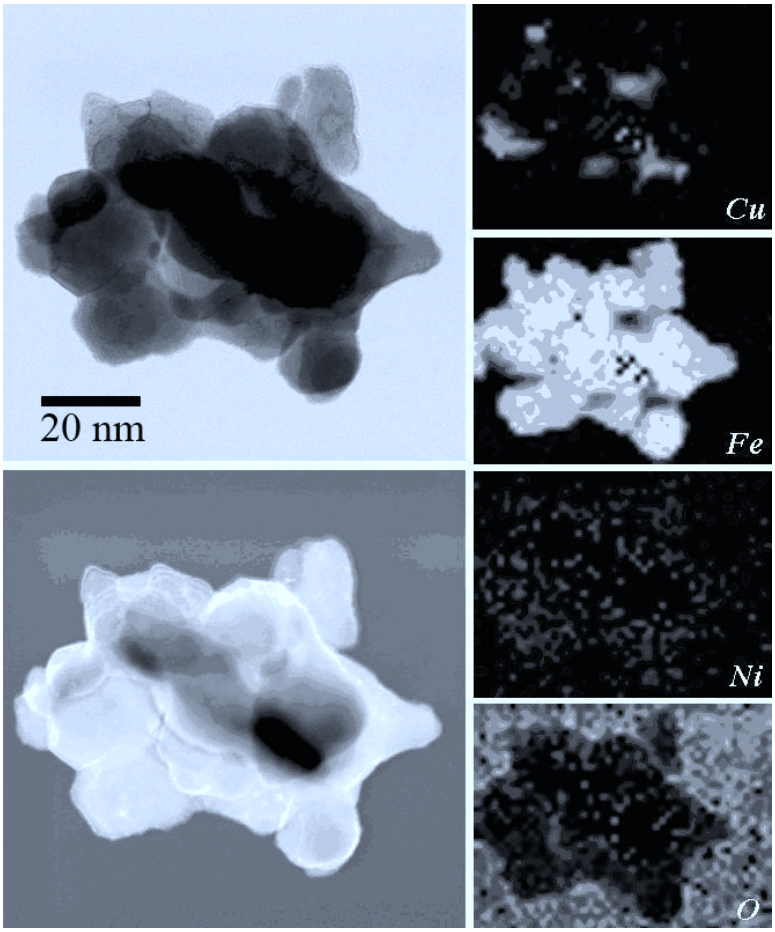

Figure 5.3 HAADF brightfield (top left) and darkfield (bottom left) images and STEM-EDS elemental analysis of Cu, Fe, Ni, and O of 20% Cu ZVI_{2LF}.

5.4.2 *Kinetic Reactions*

The products of CT degradation include CF ($CHCl_3$), dichloromethane (CH_2Cl_2), methane, formate, and carbon dioxide.[7] However, as mentioned earlier, only CT and CF were quantified in this study. A pseudo-first-order model was used to describe the kinetics of CT reduction by zero-valent iron. The reactions considered include the parallel reactions of CT and the reaction of CF to produce dichloromethane:

$$CCl_4 \xrightarrow{k_1} CHCl_3 \xrightarrow{k_2} CH_2Cl_2 \qquad (5)$$

$$CCl_4 \xrightarrow{k_3} \text{unknown products} \quad (6)$$

The term "unknown products" simply denotes the production of molecules like methane, formate, and carbon monoxide, which were not quantified experimentally. The CF yield was calculated for each experiment using the following equation:

$$Y_{CF} = \frac{k_1}{k_1 + k_3} \quad (7)$$

The rate constants determined from fitting the experimental data with Scientist® and chloroform yields for the average of two or three trials for each sample are presented in Table 5.2.

Table 5.2 Rate constants of CT reactions as determined by fitting data with the Scientist® program.

Sample	**k_1 (h^{-1})**	**k_2 (h^{-1})**	**k_3 (h^{-1})**	**Y_{CF}**
0% Cu ZVI_{6LF}	0.042 ± 0.015	0.011 ± 0.057	1.7 ± 0.1	0.024 ± 0.354
0.08% Cu ZVI_{6LF}	0.12 ± 0.03	0*	1.2 ± 0.1	0.094 ± 0.265
0% Cu ZVI_{2LF}	0.093 ± 0.035	0.013 ± 0.092	2.7 ± 0.1	0.033 ± 0.373
0.5% Cu ZVI_{2LF}	1.9 ± 0.1	0.018 ± 0.007	6.3 ± 0.2	0.23 ± 0.05
3% Cu ZVI_{2LF}	0.98 ± 0.07	0.032 ± 0.014	4.5 ± 0.2	0.18 ± 0.08
10% Cu ZVI_{2LF}	2.1 ± 0.1	0.011 ± 0.006	7.1 ± 0.4	0.23 ± 0.05
20% Cu ZVI_{2LF}	0.82 ± 0.035	0.0076 ± 0.0042	2.3 ± 0.1	0.27 ± 0.06

* For the reaction of 0.08% Cu ZVI_{6LF}, the Scientist program was unable to fit the [CF] data with positive calculated concentrations and rate constants. The rate constants had negative values (with an average of -0.01 ± 0.06) and, thus, were considered to be zero.

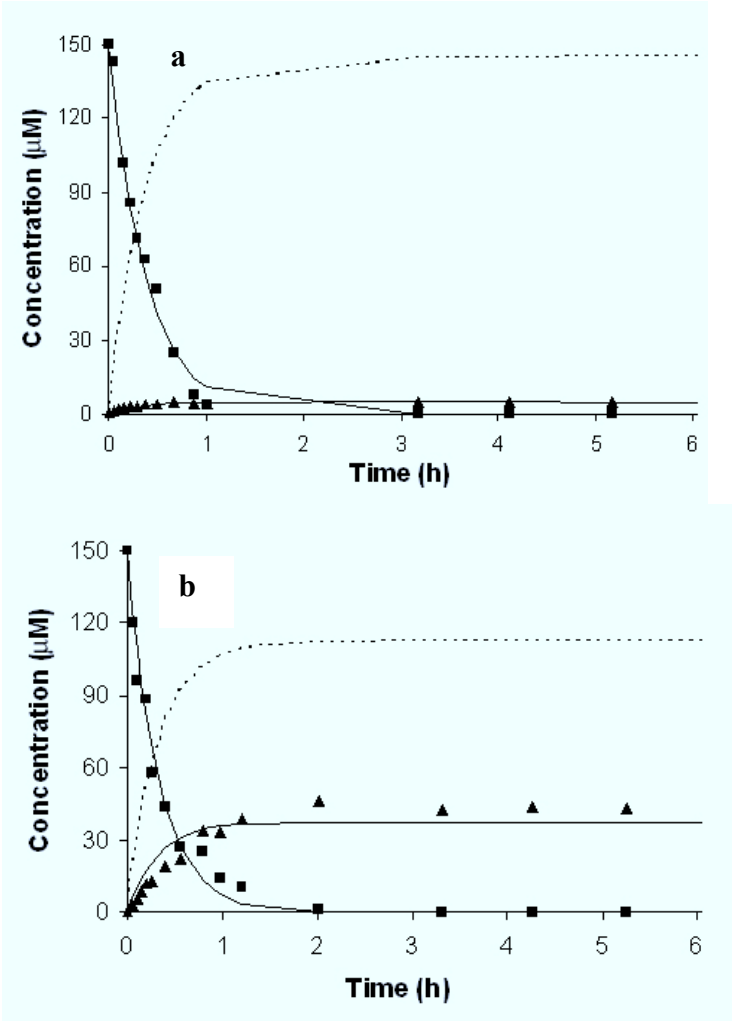

Figure 5.4 CT degradation for the reactions of (a) 0% Cu ZVI_{2LF} and (b) 20% Cu ZVI_{2LF}. (■) carbon tetrachloride; (▲) chloroform; solid lines are fit to carbon tetrachloride and chloroform data; the dashed line is fit to "unknown products."

Figure 5.4 shows the kinetic data and fits for trials using 0% Cu ZVI_{2LF} and 20% Cu ZVI_{2LF}. It is apparent from these plots that CF was produced during reactions of both the Fe and Cu/Fe ZVI samples but the CF concentrations were higher in reactions of Cu/Fe ZVI. Samples with copper had larger k_1, which increased with increasing Cu content up to 0.5 mol%, and samples with Cu content ≥3 mol% had k_1 of ca. 1 h^{-1}. The presence of copper also caused an increase in k_3 for the production of the unknown

products. The k_2 rate constants for all seven samples were similar, indicating that the presence of copper did not have a significant effect on the degradation of CF into dichloromethane. The increase in k_1 outpaced the increase of k_3, generally leading to poorer chloroform yield values (Y_{CF}, eq 7) for the zero-valent Cu/Fe materials as compared to the both 0% Cu ZVI samples and the 0.08% Cu ZVI_{6LF} sample.

5.4.3 *Solid-State Products*

Powder XRD patterns of the recovered solids after reaction with CT and after simple exposure to buffer solutions (without CT) were collected. The Rietveld refinement method was employed to quantify the mass percent of the solid phases. The XRD pattern of the post-reaction, 3% Cu ZVI_{2LF} solids is presented with the refinement results in Figure 5.5. The fraction of iron in each iron-containing phase was calculated from the refinement results (Table 5.3).

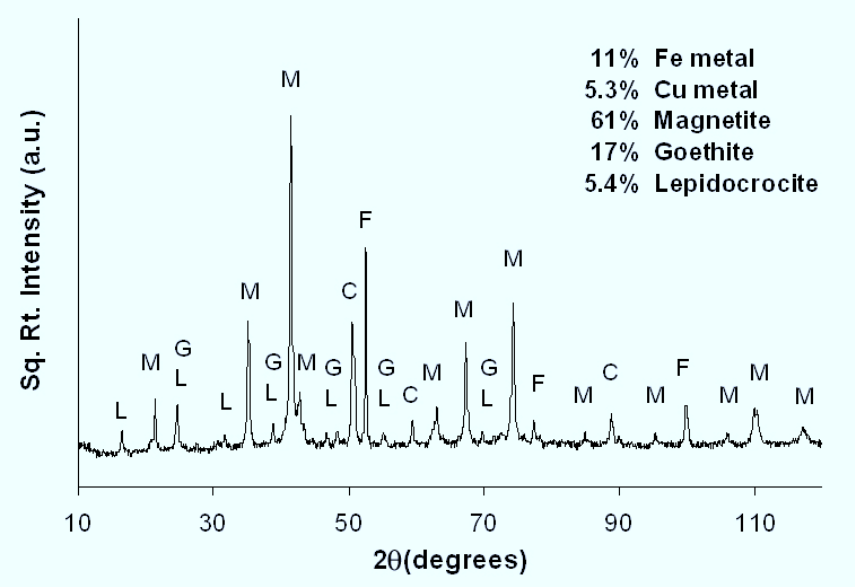

Figure 5.5 Sample XRD pattern of 3% Cu ZVI_{2LF} post-reaction solids and Rietveld refinement composition results. Peaks were matched to the reference PDF patterns of iron metal (F), copper metal (C), magnetite (M), goethite (G), and lepidocrocite (L).

Table 5.3 Percentage of total iron within each of the solid phases as calculated from the mass percent determined by Rietveld refinement of the powder XRD patterns. The top half of the table is results from blank reactions in buffer solution only, and the bottom half of the table is results from reactions with CT.

Sample Post-Blank	**%Fe as iron metal**	**%Fe as magnetite**	**%Fe as lepidocrocite**	**%Fe as goethite**
0% Cu ZVI_{6LF}	67	33	0	0
0.08% Cu ZVI_{6LF}	27	73	0	0
0% Cu ZVI_{2LF}	21	79	0	0
0.5% Cu ZVI_{2LF}	57	42	1	0
3% Cu ZVI_{2LF}	49	49	2	0
10% Cu ZVI_{2LF}	83	15	2	0
20% Cu ZVI_{2LF}	86	14	0	0
Sample Post-Reaction				
0% Cu ZVI_{6LF}	24	61	0	15
0.08% Cu ZVI_{6LF}	40	58	0	1
0% Cu ZVI_{2LF}	23	77	0	0
0.5% Cu ZVI_{2LF}	20	60	4	15
3% Cu ZVI_{2LF}	15	64	5	17
10% Cu ZVI_{2LF}	26	42	19	13
20% Cu ZVI_{2LF}	58	10	12	19

Some of the iron metal remained intact for each of the post-blank or post-reaction solids (Table 5.3). In most cases, the amount of iron metal reacted was higher in the post-reaction solids compared to the post-blank solids, with the exception of 0.08% Cu ZVI_{6LF}. In the post-blank materials, the refinement results demonstrate that corrosion by water occurs with all of the samples, producing magnetite in every case. A

small amount of lepidocrocite in the cases of 0.5%, 3%, and 10% Cu ZVI_{2LF}. The samples with the highest Cu content (10% and 20% Cu) had the smallest amount of corrosion by water. The XRD refinement results of the solids after reaction with CT demonstrate that the presence of copper resulted in significant differences in the distribution of the solid-phase products (bottom of Table 5.3). For the samples with the highest Cu content, a greater fraction of iron metal remained after reaction with CT. Magnetite was the major product, with the exception of 20% Cu ZVI_{2LF}. Goethite was identified in the post-reaction materials from all copper-containing starting materials, and lepidocrocite was identified in all samples except 0.08% Cu ZVI_{6LF}. The presence of goethite and/or lepidocrocite was also indicated by the color of the suspension during and after reaction. It is apparent in Figure 5.6 that the yellowish-orange materials (appearing lighter in the grayscale image) seen in the 0.5%, 3%, and 10% Cu ZVI_{2LF} samples were not produced in the 0% Cu ZVI_{2LF} sample. The XRD patterns showed no evidence for the formation of copper oxide phases in the blank or CT reaction solids.

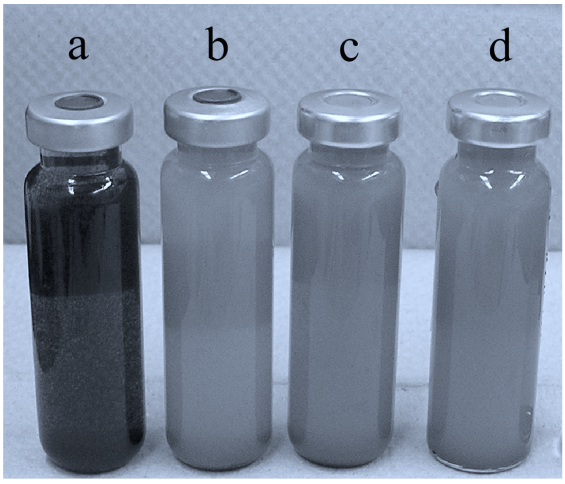

Figure 5.6 Image of post-reaction suspensions of (a) 0% Cu ZVI_{2LF}, (b) 0.5% Cu ZVI_{2LF}, (c) 3% Cu ZVI_{2LF}, and (d) 10% Cu ZVI_{2LF} samples that shows the formation of black products in (a) or light, yellowish-orange solid-state products in (b), (c), and (d).

Copper has a low aqueous solubility as a metal, but if the metal oxidized, Cu^{2+} may be released into solution during the blank and CT reactions. ICP-AES analysis of the filtered and acidified 10% Cu ZVI_{2LF} post-blank suspension revealed that a very small amount of copper was dissolved (4 μg/L dissolved Cu^{2+}, 3×10^{-3} % of initial Cu present) and a considerable amount of iron, 50 mg/L (5% of the initial Fe present), was dissolved. Although the solution had only a low concentration of dissolved Cu, it may affect the products precipitated from solution in the presence of copper ions. ICP-AES analysis of filtered and acidified solutions from the 3% Cu and 10% Cu suspensions from reaction with CT showed 30-40 mg/L of dissolved iron and less than 12 μg/L of dissolved copper (3-4% of initial Fe present, 7×10^{-3}% of initial Cu present). The somewhat higher concentrations of dissolved copper in solution and the adsorption of copper onto oxide surfaces may affect the reactions controlling the formation of solid-state products. Releasing high concentrations of copper into surrounding groundwater would also be a concern in natural systems, but the concentrations in these experiments are quite low.

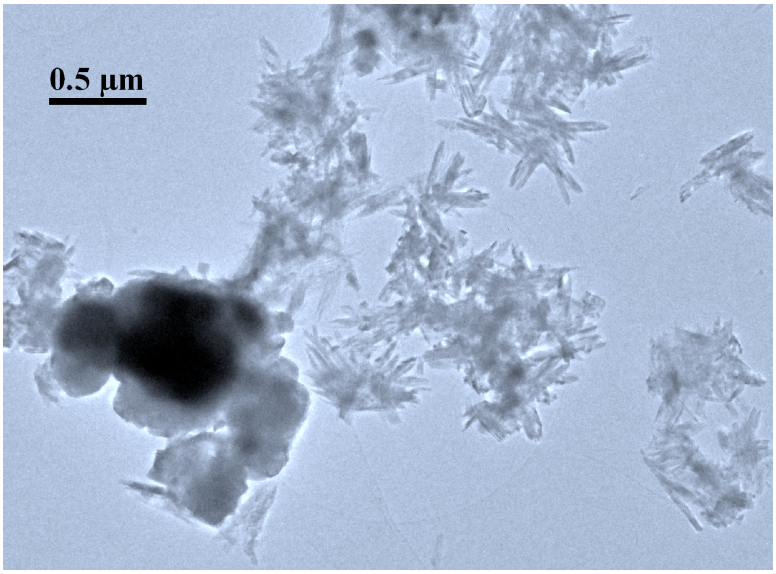

Figure 5.7 TEM image of the post-reaction solids from the reaction of carbon tetrachloride and 0.5% Cu ZVI_{2LF}.

After reaction of the ZVI samples with CT, the solid-state products were also examined with TEM. The presence of acicular crystals, typical of goethite and lepidocrocite, and large globular aggregates were apparent. The TEM image in Figure 5.7 was collected from the post-reaction materials of 20% Cu ZVI_{2LF}. Particle sizes ranged from 20-50 nanometers for smaller crystallites and up to 400 nm for large crystallites. Each iron oxide phase was identified by measuring the lattice fringes and matching with the corresponding crystal structures.

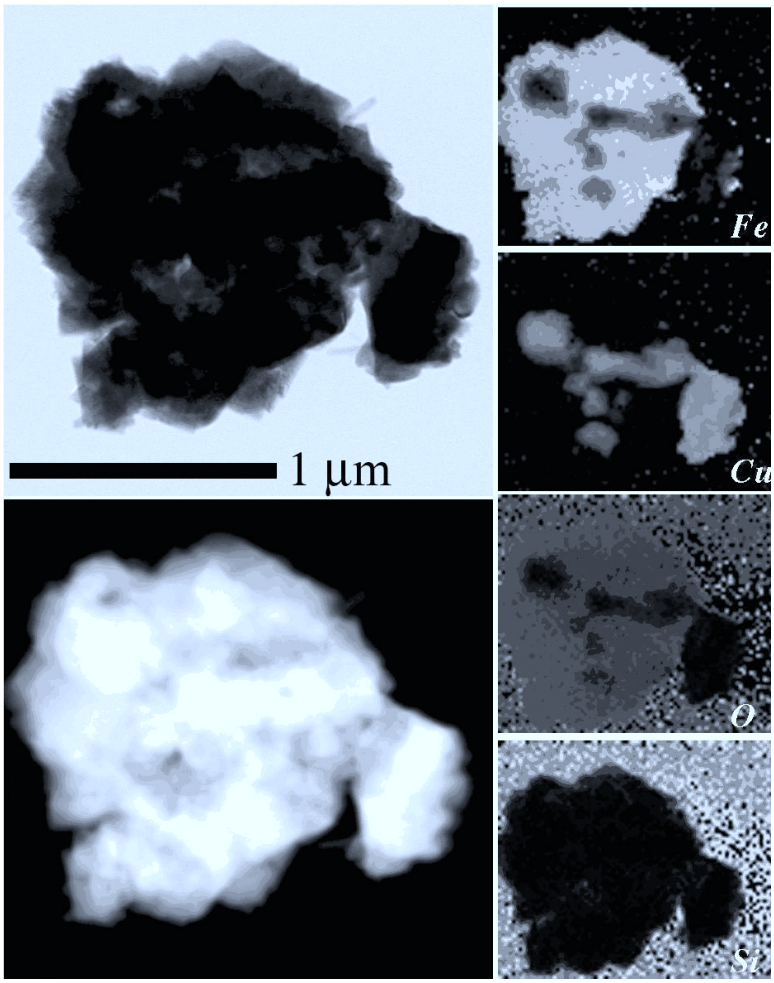

Figure 5.8 HAADF brightfield (top left) and darkfield (bottom left) images and the STEM-EDS elemental analysis of Fe, Cu, O, and Si of post-reaction materials of 20% Cu ZVI_{2LF}.

As seen in the high angle annular dark field (HAADF) images in Figure 5.8, STEM-EDS enabled the characterization of Cu, Fe, and O within post-reaction materials. Similar to the starting ZVI materials, copper appears to be in small and large masses, rather than evenly distributed within or on the surface of iron, which are often attached to large globular aggregates. Within these aggregates, areas that contain iron have significant amounts of oxygen, indicative of iron oxide minerals. The morphology

of the globular iron oxide minerals is typical of magnetite. The areas with high copper content generally do not have significant oxygen content, which means that the copper does not become oxidized but remains copper metal throughout the reaction. This supports the XRD results, in which copper oxide phases were not detected in the post-reaction solids; however, copper metal was present and measured with similar content as compared to the ZVI starting materials. EDS analysis of the needle-like crystals of goethite and lepidocrocite demonstrates that copper is not incorporated into these mineral products at detectable levels. However, small (5-10 nm), spherical particles that were rich in copper (as determined by EDS analysis) were sometimes associated with or near the crystal aggregates. Figure 5.9 shows three small particles in close proximity to a few iron oxide crystals. Using a very small beam size and including only one small particle at a time, such as particle "copper 7c," EDS analysis showed that these areas had a much higher copper content than the needle-like crystals.

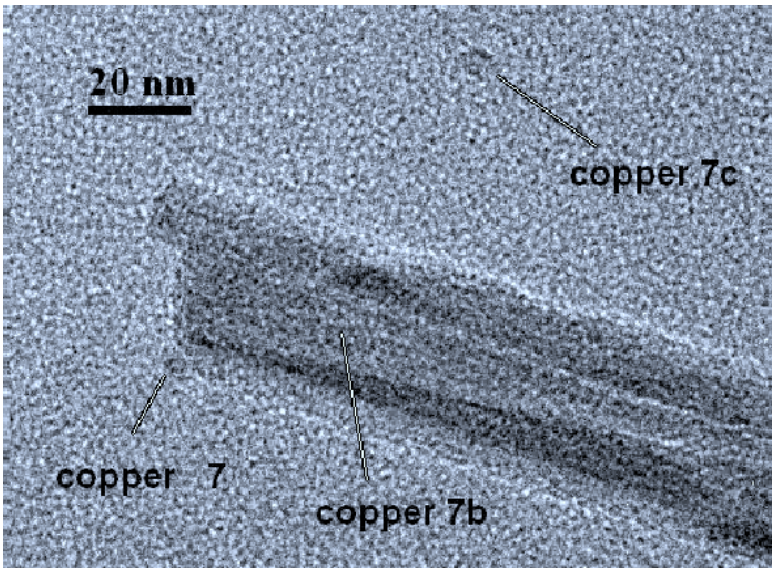

Figure 5.9 Small copper particles associated with needle-like iron oxide products from the reaction of 20% Cu ZVI_{2LF} particles.

In summary, copper was successfully incorporated into ZVI materials by the reduction of copper-doped ferrihydrite materials. The 6LF synthesis method was not effective for incorporating copper, but the 2LF synthesis method was very efficient and gave predictable results for doping. ICP-AES provided Cu composition data for all samples. The primary crystalline phase of ZVI samples was iron metal, and of bimetallic samples, iron and copper metals. Copper enhanced the rates of carbon tetrachloride degradation, including the rate of transformation to chloroform. However, subsequent breakdown of chloroform was unaffected. Therefore, the chloroform yield of Cu/Fe ZVI samples seems to be higher. No evidence for the production of copper (II) phases was observed, although some Cu^{2+} in solution suggests some redox of Cu during reaction with blank and CT solutions.

5.5 Conclusions

Reductive degradation of CT by bimetallic Cu/Fe particles is much faster than by iron metal particles. However, the addition of copper did not increase the rate of chloroform reduction nor reduce the chloroform yield. In fact the chloroform yield was higher for Cu/Fe materials than for Fe materials. The solid-state products of the reaction with CT were affected by the presence and content of copper within ZVI samples.

5.6 Acknowledgements

This work was supported by the IGERT Program of the National Science Foundation under award Number DGE-0114372 (fellowship to J.J.E.); the U.S. Department of Energy (DOE) Environmental Management Sciences Program and the

Office of Energy Research, Office of Basic Energy Sciences, Chemical Sciences Division; Undergraduate Research Opportunities Program (UROP), administered by the Vice-Provost for Undergraduate Education at the University of Minnesota; and the Department of Chemistry at the University of Minnesota. TEM characterization was carried out at the Characterization Facility, University of Minnesota, which receives support from NSF through the National Nanotechnology Infrastructure Network. We thank Matt Hofer for the preparation of the 6LF powders for the 0% and 0.08% Cu ZVI_{6LF}.

5.7 References

1. Li, X.-q.; Elliot, D. W.; Zhang, W.-x. Zero-valent iron nanoparticles for abatement of environmental pollutants: materials and engineering aspects. *Critical Reviews in Solid State and Materials Sciences* **2006** 31, 111.

2. Li, L.; Fan, M.; Brown, R. C.; Van Leeuwen, J.; Wang, J.; Wang, W.; Song, Y.; Zhang, P. Synthesis, properties, and environmental applications of nanoscale iron-based materials: A review. *Critical Reviews in Environmental Science and Technology* **2006** 36, 405.

3. Zhang, W.-x. Nanoscale iron particles for environmental remediation: An overview. *Journal of Nanoparticle Research* **2003** 5, 323.

4. Lien, H.-L.; Zhang, W.-x. Transformation of chlorinated methanes by nanoscale iron particles. *Journal of Environmental Engineering* **1999** 125 (11), 1042.

5. Matheson, L. J.; Tratnyek, P. G. Reductive dehalogenation of chlorinated methanes by iron metal. *Environmental Science and Technology* **1994** 28, 2045.

6. Maithreepala, R. A.; Doong, R.-a. Synergistic effect of copper ion on the reductive dechlorination of carbon tetrachloride by surface-bound Fe(II) associated with goethite. *Environmental Science and Technology* **2004** 38, 260.

7. Tamara, M. L.; Butler, E. C. Effects of iron purity and groundwater characteristics on rates and products in the degradation of carbon tetrachloride by iron metal. *Environmental Science and Technology* **2004** 38, 1866.

8. Bransfield, S. J.; Cwiertny, D. M.; Roberts, A. L.; Fairbrother, D. H. Influence of copper loading and surface coverage on the reactivity of granular iron toward 1,1,1-trichloroethane. *Environmental Science and Technology* **2006** 40, 1485.

9. Cwiertny, D. M.; Bransfield, S. J.; Livi, K. J. T.; Fairbrother, D. H.; Roberts, A. L. Exploring the influence of granular iron additives on 1,1,1-trichloroethane reduction. *Environmental Science and Technology* **2006** 40, 6837.

10. Kim, Y.-H.; Carraway, E. R. Reductive dechlorination of TCE by zero valent bimetals. *Environmental Technology* **2003** 24 (1), 69.

11. Cwiertny, D. M.; Bransfield, S. J.; Roberts, A. L. Influence of the oxidizing species on the reactivity of iron-based bimetallic reductants. *Environmental Science and Technology* **2007** 41, 3734.

12. Xu, Y.; Zhang, W.-x. Subcolloidal Fe/Ag particles for reduction of chlorinated benzenes. *Industrial & Engineering Chemistry Research* **2000** 39 (7), 2238.

13. Lien, H.-L.; Zhang, W.-x. Hydrodechlorination of chlorinated ethanes by nanoscale Pd/Fe bimetallic particles. *Journal of Environmental Engineering* **2005** 131 (1), 4.

14. Zhang, W.-x.; Wang, C.-B.; Lien, H.-L. Treatment of chlorinated organic contaminants with nanoscale bimetallic particles. *Catalysis Today* **1998** 40, 387.

15. Elsner, M.; Cwiertny, D. M.; Roberts, A. L.; Sherwood Lollar, B. 1,1,2,2-Tetrachloroethane reactions with OH-, Cr(II), granular iron, and copper-iron bimetal: Insights from product formation and associated carbon isotope fractionation. *Environmental Science and Technology* **2007** 41, 4111.

16. Fennelly, J. P.; Roberts, A. L. Reaction of 1,1,1-trichloroethane with zero-valent metals and bimetallic reductants. *Environmental Science and Technology* **1998** 32 (13), 1980.

17. Lien, H.-L.; Zhang, W.-x. Enhanced dehalogenation of halogenated methanes by bimetallic Cu/Al. *Chemosphere* **2002** 49, 371.

18. Maithreepala, R. A.; Doong, R.-a. Enhanced remediation of carbon tetrachloride by Fe(II)-Fe(III) systems in the presence of copper ions. *Water Science and Technology* **2004** 50 (8), 161.

19. Yang, M. X.; Sarkar, S.; Bent, B. E. Degradation of multiply-chlorinated hydrocarbons on Cu(100). *Langmuir* **1997** 13, 229.

20. Liou, Y. H.; Lo, S. L.; Lin, C. J. Size effect in reactivity of copper nanoparticles to carbon tetrachloride degradation. *Water Research* **2007** 41, 1705.

21. Schwertmann, U.; Cornell, R. M., *Iron Oxides in the Laboratory*. 2nd ed.; Wiley-VCH: Weinheim, 2000.

22. Rietveld, H. M. A profile refinement method for nuclear and magnetic structures. *Journal of Applied Crystallography* **1969** 2, 65.

23. Wilburn, D. R.; Bassett, W. A. Hydrostatic compression of iron and related compounds: an overview. *American Mineralogist* **1978** 63, 591.

24. Wyckoff, R. W. G., *Crystal Structures 1*. 2nd ed.; Interscience Publishers: New York, NY, 1963.

25. Okudera, H.; Kihara, K.; Matsumoto, T. Temperature dependence of structure parameters in natural magnetite: single crystal X-ray studies from 126 to 773 K. *Acta Crystallographica* **1996** B 52, 450.

26. Waychunas, G. A. Crystal chemistry of oxides and hydroxides. *Reviews in Mineralogy* **1991** 25, 11.

Chapter 6

Conclusions

Iron oxide materials occur naturally in many soils and sediments and undergo biotic and abiotic redox reactions in the environment, so it is important to understand their fundamental chemical properties. Zero-valent iron materials are used to remediate chlorinated halogens and other species in subsurface environments, leading to the formation of iron oxide minerals. Specifically, the kinetics of reductive dissolution and the growth kinetics by oriented aggregation of ferrihydrite, the kinetics of reductive dissolution of As-bearing ferrihydrites, and the kinetics of carbon tetrachloride degradation with Cu-ZVI materials were investigated. Inductively coupled plasma-mass spectrometry or -atomic emission spectrometry, powder X-ray diffraction, transmission electron microscopy, electron dispersive X-ray analysis, X-ray absorption spectroscopy, extended X-ray absorption fine structure analysis, small angle X-ray scattering, Mössbauer spectroscopy, low temperature magnetic methods, and potentiometric titrations were used to relate the nanoparticle size, incorporation of As into materials, or incorporation of Cu into materials to the results of kinetic experiments.

Ferrihydrite ranges in size from 3-10 nm, and the increase in reactive surface area with decreasing nanoparticle size influences its reactivity. The reductive dissolution kinetics of ferrihydrite were investigated using hydroquinone and rates were determined by the formation of benzoquinone. Ferrihydrite size effects were also studied during aging of ferrihydrite nanodots into goethite nanorods by oriented aggregation and phase transformation. Ferrihydrite nanoparticle size was found to have little or no effect on the kinetics of reductive dissolution by hydroquinone. In contrast, ferrihydrite nanoparticle size has a significant affect on the kinetics of growth by oriented aggregation to produce goethite nanorods, with rates increasing significantly with decreasing precursor size. It was demonstrated that ferrihydrite nanoparticle size can be controlled by the hydrolysis temperature during nucleation from a homogeneous solution. Furthermore, we show that the size goethite nanocrystals formed by aging depends directly on the size of precursor ferrihydrite nanoparticles.

Arsenic has a high affinity for iron oxides and may be incorporated into the mineral structure or adsorbed onto the mineral surface. The reductive dissolution kinetics of ferrihydrite prepared by coprecipitation with or adsorption of up to 10 wt% arsenate (AsO_4^{3-}) were quantified. Arsenic adsorbed preferentially onto the most reactive surface sites, thereby substantially lowering the reaction rate, while coprecipitation led to structural defects within the particles but its initial rate was similar to pure ferrihydrite. Results presented here provide insight in regards to predictions of arsenic release from arsenic-bearing iron oxides in natural systems. Specifically, it is the nature of the arsenic loading, either predominantly at the surface or

incorporated into the bulk of the particles, that is expected to be the best predictor of large scale release of arsenic from natural iron oxide particles.

The remediation of chlorinated hydrocarbons and other species with zero-valent iron (ZVI) materials (e.g., in permeable reactive barriers) leads to the formation and deposition of iron oxide minerals upon reaction. The incorporation of metal additives (e.g., Pd, Ni, Cu) enhances the reactivity of ZVI materials and can influence the contaminant degradation products and solid-state oxidation products. It has been demonstrated in this dissertation that the incorporation of copper in ZVI materials increased the rate of carbon tetrachloride reductive dechlorination, led to higher concentrations of chloroform during reaction, and influenced the solid-state mineral products of ZVI oxidation. Although copper did increase the rates of carbon tetrachloride degradation, it had no effect on the rate of chloroform degradation. Therefore, copper is not a preferred additive for ZVI materials in remediation applications at this time, but ZVI modified with other metal (e.g. Pd, Ni), or possibly even nonmetal (e.g. P, N, C), additives may serve as better materials for remediation applications.

This dissertation demonstrates the importance of studying the chemistry of natural systems through controlled, modeled systems within the laboratory. The systematic reductive dissolution kinetic studies of ferrihydrite materials permitted the investigation of initial reaction rates, empirical rate laws, activation energies, and Arrhenius pre-exponential factors among the size-varied and arsenic-bearing sample series. Experimental variables such as synthesis temperature, the drying of ferrihydrite suspensions to produce powders, and the method of arsenic incorporation affect the

reactivity of samples. As demonstrated in each ferrihydrite reductive dissolution study, it is essential to adequately characterize the reaction materials to provide insight on the similarities and differences among samples and interpret the kinetic results. The importance of experimental design and interpretation are highlighted in Chapter 3 with the kinetic study of goethite nanocrystal growth from ferrihydrite precursor particles by oriented aggregation. The controlled synthesis, growth, sampling methods, characterization, analysis, and interpretation of the growth study results were essential to the success of the research project. Due to ferrihydrite's natural abundance and importance as a reactive material in natural systems, the continued study of ferrihydrite reactivity is critical. Future work may include the influence of other trace species on reductive dissolution, the kinetic investigation of natural and anthropogenic redox-active organic species, and the influence of trace species on the growth and transformation of ferrihydrite into goethite.

Bibliography

Anschutz, A. J. Reactivity of iron oxyhydroxide nanoparticles: Effects of physical variables. Doctor of Philosophy, University of Minnesota, Minneapolis, MN, 2006.

Anschutz, A. J.; Penn, R. L. Reduction of crystalline iron(III) oxyhydroxides using hydroquinone: Influence of phase and particle size. *Geochemical Transactions* **2005** 6 (3), 60.

Appello, C. A. J.; van der Weiden, M. J. J.; Tournassat, C.; Charlet, L. Surface complexation of ferrous iron and carbonate on ferrihydrite and the mobilization of arsenic. *Environmental Science and Technology* **2002** 36, 3096.

Banfield, J. F.; Welch, S. A.; Zhang, H.; Ebert, T. T.; Penn, R. L. Aggregation-based crystal growth and microstructure development in natural iron oxyhydroxide biomineralization products. *Science* **2000** 289, 751.

Banfield, J. F.; Zhang, H., Nanoparticles in the Environment. In *Nanoparticles and the Environment*, 1st ed.; Banfield, J. F.; Navrotsky, A., The Mineralogical Society of America: Washington, DC, 2001; 44.

Bennett, B.; Dudas, M. J. Release of Arsenic and Molybdenum by Reductive Dissolution of Iron Oxides in a Soil with Enriched Levels of Native Arsenic. *Journal of Environmental Engineering and Science* **2003** 2, 265.

Berquó, T. S.; Banerjee, S. K.; Ford, R.; Penn, R. L.; Pichler, T. High crystallinity Si-ferrihydrite: An insight into its Néel temperature and size dependence of magnetic properties. *Journal of Geophysical Research B: Solid Earth* **2007** 112, B02102.

Berquó, T. S.; Erbs, J. J.; Lindquist, A.; Penn, R. L.; Banerjee, S. K. Effects of magnetic interactions in antiferromagnetic ferrihydrite particles. *Journal of Physics: Condensed Matter* **2009** 21, 176005.

Biber, M. V.; dos Santos Afonso, M.; Stumm, W. The coordination chemistry of weathering: IV. Inhibition of the dissolution of oxide minerals. *Geochimica et Cosmochimica Acta* **1994** 58 (9), 1999.

Boily, J.-F.; Persson, P.; Sjoberg, S. Benzenecarboxylate surface complexation at the goethite (α-FeOOH)/water interface. *Journal of Colloid and Interface Science* **2000** 227, 132.

Bransfield, S. J.; Cwiertny, D. M.; Roberts, A. L.; Fairbrother, D. H. Influence of copper loading and surface coverage on the reactivity of granular iron toward 1,1,1-trichloroethane. *Environmental Science and Technology* **2006** 40, 1485..

Brown, G. E.; Calas, G.; Waychunas, G. A.; Petiau, J. X-ray absorption spectroscopy and its applications in mineralogy and geochemistry. *Reviews in Mineralogy* **1988** 18, 431.

Burleson, D. J.; Penn, R. L. Two-step growth of goethite from ferrihydrite. *Langmuir* **2006** 22, 402.

Chun, C. L.; Penn, R. L.; Arnold, W. A. Kinetic and microscopic studies of reductive transformations of organic contaminants on goethite. *Environmental Science and Technology* **2006** 40, 3299.

Cornell, R. M.; Schwertmann, U., *The Iron Oxides: Structure, Properties, Reactions, Occurrences and Uses*. 2nd ed.; Wiley-VCH: Weinheim, 2003.

Cwiertny, D. M.; Bransfield, S. J.; Livi, K. J. T.; Fairbrother, D. H.; Roberts, A. L. Exploring the influence of granular iron additives on 1,1,1-trichloroethane reduction. *Environmental Science and Technology* **2006** 40, 6837.

Cwiertny, D. M.; Bransfield, S. J.; Roberts, A. L. Influence of the oxidizing species on the reactivity of iron-based bimetallic reductants. *Environmental Science and Technology* **2007** 41, 3734.

Davis, T. M.; Drews, T. O.; Ramanan, H.; He, C.; Dong, J.; Schnablegger, H.; Katsoulakis, M. A.; Kokkoli, E.; McCormick, A. V.; Penn, R. L.; Tsapatsis, M. Mechanistic principles of nanoparticle evolution to zeolite crystals. *Nature Materials* **2006** 5, 400.

Derjaguin, B. V.; Landau, L. Theory of the stability of strongly charged lyophobic solds and the adhesion of strongly charged particles in solution of electrolytes. *Acta Physicochimica URSS* **1941** 14, 633.

Dormann, J. L.; Fiorani, D.; Tronc, E., Magnetic Relaxation in fine-particle systems. In *Advances in Chemical Physics*, 1st ed.; Prigogine, I.; Rice, S. A., John Wiley & Sons, Inc.: 1997; 98.

Drews, T. O.; Tsapatsis, M. Model of the evolution of nanoparticles to crystals via an aggregative growth mechanism. *Microporous and Mesoporous Materials* **2007** 101 (1-2), 97.

Duarte, E. L.; Itri, R.; Lima, E.; Baptista, M. S.; Berquó, T. S.; Goya, G. F. Large magnetic anisotropy in ferrihydrite nanoparticles synthesized from reverse micelles. *Nanotechnology* **2006** 17, 5549.

Dzombak, D. A.; Morel, F. M. M., *Surface Complexation Modeling: Hydrous Ferric Oxide*. 1st ed.; Wiley-Interscience: New York, 1990.

Elsner, M.; Cwiertny, D. M.; Roberts, A. L.; Sherwood Lollar, B. 1,1,2,2-Tetrachloroethane reactions with OH-, Cr(II), granular iron, and copper-iron bimetal: Insights from product formation and associated carbon isotope fractionation. *Environmental Science and Technology* **2007** 41, 4111.

Espenson, J. H., *Chemical Kinetics and Reaction Mechanisms*. 2nd ed.; McGraw-Hill: New York, 2002.

Fennelly, J. P.; Roberts, A. L. Reaction of 1,1,1-trichloroethane with zero-valent metals and bimetallic reductants. *Environmental Science and Technology* **1998** 32 (13), 1980.

Ford, R. G.; Bertsch, P. M.; Farley, K. J. Changes in transition and heavy metal partitioning during hydrous iron oxide aging. *Environmental Science and Technology* **1997** 31, 2028.

Frandsen, C.; Bahl, C. R. H.; Lebech, B.; Lefmann, K.; Theil Kuhn, L.; Keller, L.; Andersen, N. H.; Zimmermann, M. v.; Johnson, E.; Klausen, S. N.; Mørup, S. Oriented attachment and exchange coupling of α-Fe_2O_3 nanoparticles. *Physical Review B* **2005** 72, 214406.

Frandsen, C.; Mørup, S. Inter-particle interactions in composites of antiferromagnetic nanoparticles. *Journal of Magnetism and Magnetic Materials* **2003** 266, 36.

Fuller, C. C.; Davis, J. A.; Waychunas, G. A. Surface chemistry of ferrihydrite: Part 2. Kinetics of arsenate adsorption and coprecipitation. *Geochimica et Cosmochimica Acta* **1993** 57, 2271.

Gilbert, B.; Lu, G.; Kim, C. S. Stable cluster formation in aqueous suspensions of iron oxyhydroxide nanoparticles. *Journal of Colloid and Interface Science* **2007** 313 (1), 152.

Gilbert, B.; Zhang, H.; Huang, F.; Finnegan, M. P.; Waychunas, G. A.; Banfield, J. F. Special phase transformation and crystal growth pathways observed in nanoparticles. *Geochemical Transactions* **2003** 4, 20.

Gilles, C.; Bonville, P.; Wong, K. K. W.; Mann, S. Non-Langevin behaviour of the uncompensated magnetization in nanoparticles of artificial ferritin. *European Physical Journal B* **2000** 17, 417.

Guyodo, Y.; Banerjee, S. K.; Penn, R. L.; Burleson, D.; Berquó, T. S.; Seda, T.; Solheid, P. Magnetic properties of synthetic six-line ferrihydrite nanoparticles. *Physics of the Earth and Planetary Interior* **2006** 154, 222.

Guyodo, Y.; Mostrom, A.; Penn, R. L.; Banerjee, S. K. From nanodots to nanorods: Oriented aggregation and magnetic evolution of nanocrystalline goethite. *Geophysical Research Letters* **2003** 30 (10), 1512.

Hochella, M. F., Jr. Nanoscience and technology: The next revolution in the Earth sciences. *Earth and Planetary Science Letters* **2002** 203, 593.

Hofmann, A.; Pelletier, M.; Michot, L.; Stradner, A.; Schurtenberger, P.; Kretzschmar, R. Characterization of the pores in hydrous ferric oxide aggregates formed by freezing and thawing. *Journal of Colloid and Interface Science* **2004** 271, 163.

Huang, F.; Zhang, H.; Banfield, J. F. The role of oriented attachment crystal growth in hydrothermal coarsening of nanocrystalline ZnS. *J. Phys. Chem. B* **2003** 107, 10470.

Huang, F.; Zhang, H.; Banfield, J. F. Two-stage crystal-growth kinetics observed during hydrothermal coarsening of nanocrystalline ZnS. *Nano Letters* **2003** 3 (3), 373.

Hyning, D. L. V.; Klemperer, W. G.; Zukoski, C. F. Silver nanoparticle formation: Predictions and verification of the aggregative growth model. *Langmuir* **2001** 17 (11), 3128.

Jambor, J. L.; Dutrizac, J. E. Occurrence and constitution of natural and synthetic ferrihydrite, a widespread iron oxyhydroxide. *Chemical Reviews* **1998** 98, 2549.

Jentzsch, T. L.; Penn, R. L. Influence of aluminum doping on ferrihydrite nanoparticle reactivity. *Journal of Physical Chemistry B* **2006** 110, 11746.

Jia, C.; Cheng, Y.; Bao, F.; Chen, D.; Wang, Y. pH value-dependant growth of α-Fe_2O_3 hierarchical nanostructures. *Journal of Crystal Growth* **2006** 294, 353.

Johnson, T. L.; Scherer, M. M.; Tratnyek, P. G. Kinetics of halogenated organic compound degradation by iron metal. *Environmental Science and Technology* **1996** 30, 2634.

Kerisit, S.; Cooke, D. J.; Spagnoli, D.; Parker, S. C. Molecular dynamics simulations of the interactions between water and inorganic solids. *Journal of Materials Chemistry* **2005** 15, 1454.

Kim, B. J.; Lee, H. I.; Cho, S.-B.; Yoon, S.; Suh, B. J.; Jang, Z. H.; St. Pierre, T. G.; Kim, S.-W. Magnetic properties of artificially synthesized ferritins. *Journal of Applied Physics* **2005** 97, 10M524.

Kim, C. S.; Lentini, C. J.; Waychunas, G. A., Synchrotron-based studies of metal adsorption and structural incorporation with iron oxyhydroxide nanoparticles. In *Adsorption of Metals by Geomedia II: Variables, Mechanisms, and Model Applications*, 1st ed.; Barnett, M., Elsevier Academic Press: 2008.

Kim, C. S.; Rytuba, J. J.; Brown, G. E. EXAFS study of mercury(II) sorption to Fe- and Al-(hydr)oxides: I. Effects of pH. *Journal of Colloid and Interface Science* **2004** 271, 1.

Kim, Y.-H.; Carraway, E. R. Reductive dechlorination of TCE by zero valent bimetals. *Environmental Technology* **2003** 24 (1), 69.

Kumar, S.; Davis, T. M.; Ramanan, H.; Penn, R. L.; Tsapatsis, M. Aggregative growth of silicalite-1. *Journal of Physical Chemistry B* **2007** 111 (13), 3398.

Kung, K.-H.; McBride, M. B. Electron transfer processes between hydroquinone and iron oxides. *Clays and Clay Minerals* **1988** 36 (4), 303.

Kurokawa, H.; Senna, M. Property control of acicular γ-Fe_2O_3 particles by synthesis conditions of starting goethite. *Funtai Kogaku Kaishi* **2000** 37, 788.

LaKind, J. S.; Stone, A. T. Reductive dissolution of goethite by phenolic reductants. *Geochimica et Cosmochimica Acta* **1989** 53 (5), 961.

Lenoble, V.; Deluchat, V.; Serpaud, B.; Bollinger, J.-C. Arsenite oxidation and arsenate determination by the molybdene blue method. *Talanta* **2003** 61, 267.

Li, L.; Fan, M.; Brown, R. C.; Van Leeuwen, J.; Wang, J.; Wang, W.; Song, Y.; Zhang, P. Synthesis, properties, and environmental applications of nanoscale iron-based materials: A review. *Critical Reviews in Environmental Science and Technology* **2006** 36, 405.

Li, X.-q.; Elliot, D. W.; Zhang, W.-x. Zero-valent iron nanoparticles for abatement of environmental pollutants: materials and engineering aspects. *Critical Reviews in Solid State and Materials Sciences* **2006** 31, 111.

Liang, X.; Wang, X.; Zhuang, J.; Chen, Y.; Wang, D.; Li, Y. Synthesis of nearly monodisperse iron oxide and oxyhydroxide nanocrystals. *Advanced Functional Materials* **2006** 16 (14), 1805.

Lien, H.-L.; Zhang, W.-x. Enhanced dehalogenation of halogenated methanes by bimetallic Cu/Al. *Chemosphere* **2002** 49, 371.

Lien, H.-L.; Zhang, W.-x. Hydrodechlorination of chlorinated ethanes by nanoscale Pd/Fe bimetallic particles. *Journal of Environmental Engineering* **2005** 131 (1), 4.

Lien, H.-L.; Zhang, W.-x. Transformation of chlorinated methanes by nanoscale iron particles. *Journal of Environmental Engineering* **1999** 125 (11), 1042.

Liou, Y. H.; Lo, S. L.; Lin, C. J. Size effect in reactivity of copper nanoparticles to carbon tetrachloride degradation. *Water Research* **2007** 41, 1705.

Madden, A. S.; Hochella, M. F., Jr. A test of geochemical reactivity as a function of mineral size: Manganese oxidation promoted by hematite nanoparticles. *Geochimica et Cosmochimica Acta* **2005** 69 (2), 389.

Madden, A. S.; Hochella, M. F., Jr.; Luxton, T. P. Insights for size-dependent reactivity of hematite nanomineral surfaces through Cu^{2+} sorption. *Geochimica et Cosmochimica Acta* **2006** 70, 4095.

Manceau, A. The mechanism of anion adsorption on iron oxides: Evidence for the bonding of arsenate tetrahedra on free Fe(O,OH)6 edges. *Geochimica et Cosmochimica Acta* **1995** 59, 3647.

Maithreepala, R. A.; Doong, R.-a. Enhanced remediation of carbon tetrachloride by Fe(II)-Fe(III) systems in the presence of copper ions. *Water Science and Technology* **2004** 50 (8), 161.

Maithreepala, R. A.; Doong, R.-a. Synergistic effect of copper ion on the reductive dechlorination of carbon tetrachloride by surface-bound Fe(II) associated with goethite. *Environmental Science and Technology* **2004** 38, 260.

Matheson, L. J.; Tratnyek, P. G. Reductive dehalogenation of chlorinated methanes by iron metal. *Environmental Science and Technology* **1994** 28, 2045.

Michel, F. M.; Ehm, L.; Antao, S. M.; Lee, P. L.; Chupas, P. J.; Liu, G.; Strongin, D. R.; Schoonen, M. A. A.; Phillips, B. L.; Parise, J. B. The structure of ferrihydrite, a nanocrystalline material. *Science* **2007** 316, 1726.

Mikutta, C.; Mikutta, R.; Bonneville, S.; Wagner, F.; Voegelin, A.; Christl, I.; Kretzschmar, R. Synthetic coprecipitates of exopolysaccharides and ferrihydrite. Part I: Characterization. *Geochimica et Cosmochimica Acta* **2008** 72, 1111.

Murad, E.; Cashion, J., *Mössbauer spectroscopy of environmental materials and their industrial utilization*. 1st ed.; Kluwer Academic Publishers: Boston, 2004.

Nesterova, M.; Moreau, J.; Banfield, J. F. Model biomimetic studies of templated growth and assembly of nanocrystalline FeOOH. *Geochimica et Cosmochimica Acta* **2003** 67 (6), 1185.

Niederberger, M.; Cölfen, H. Oriented attachment of mesocrystals: Non-classical crystallization mechanisms based on nanoparticle assembly. *Physical Chemistry Chemical Physics* **2006** 8, 3271.

Okudera, H.; Kihara, K.; Matsumoto, T. Temperature dependence of structure parameters in natural magnetite: single crystal X-ray studies from 126 to 773 K. *Acta Crystallographica* **1996** B 52, 450.

O'Reilly, W., *Rock and Mineral Magnetism*. 1st ed.; Blackie: Glasgow, 1984.

Paige, C. R.; Snodgrass, W. J.; Nicholson, R. V.; Sharer, J. M. An arsenate effect on ferrihydrite dissolution kinetics under acidic oxic conditions. *Water Research* **1997** 31 (9), 2370.

Pederson, H. D.; Postma, D.; Jakobsen, R. Release of arsenic associated with the reduction and transformation of iron oxides. *Geochimica et Cosmochimica Acta* **2006** 70, 4116.

Penn, R. L. Kinetics of oriented aggregation. *J. Phys. Chem. B* **2004** 108 (34), 12707.

Penn, R. L.; Banfield, J. F. Formation of rutile nuclei at anatase {112} twin interfaces and the phase transformation mechanism in nanocrystalline titania. *American Mineralogist* **1999** 84 (5-6), 871.

Penn, R. L.; Banfield, J. F. Imperfect oriented attachment: Dislocation generation in defect-free nanocrystals. *Science* **1998** 281 (5379), 969.

Penn, R. L.; Banfield, J. F. Morphology development and crystal growth in nanocrystalline aggregates under hydrothermal conditions: insights from titania. *Geochimica et Cosmochimica Acta* **1999** 63 (10), 1549.

Penn, R. L.; Banfield, J. F. Oriented attachment and growth, twinning, polytypism, and formation of metastable phases: Insights from nanocrystalline TiO_2. *American Mineralogist* **1998** 83 (9-10), 1077.

Penn, R. L.; Erbs, J. J.; Gulliver, D. M. Controlled growth of alpha-FeOOH nanorods by exploiting-oriented aggregation. *Journal of Crystal Growth* **2006** 293, 1.

Penn, R. L.; Oskam, G.; Strathmann, T. J.; Searson, P. C.; Stone, A. T.; Veblen, D. R. Epitaxial assemby in aged colloids. *J. Phys. Chem. B* **2001** 105, 2177.

Penn, R. L.; Tanaka, K.; Erbs, J. J. Size dependent kinetics of oriented aggregation. *Journal of Crystal Growth* **2007** 309, 91.

Penn, R. L.; Zhu, C.; Xu, H.; Veblen, D. R. "Iron oxide" coatings on sand grains from the Atlantic coastal plain: HRTEM characterization. *Geology* **2001** 29, 843.

Pichler, T.; Veizer, J.; Hall, G. E. M. Natural input of arsenic into a coral-reef ecosystem by hydrothermal fluids and its removal by Fe(II) Oxyhydroxides. *Environmental Science and Technology* **1999** 33, 1373.

Punnoose, A.; Phanthavady, T.; Seehra, M. S.; Shah, N.; Huffman, G. P. Magnetic properties of ferrihydrite nanoparticles doped with Ni, Mo, and Ir. *Physical Review B* **2004** 69, 054425.

Rancourt, D. G.; Fortin, D.; Pichler, T.; Thibault, P.-J.; Lamarche, G.; Morris, R. V.; Mercier, P. H. J. Mineralogy of a natural As-rich hydrous ferric oxide coprecipitate formed by mixing of hydrothermal fluid and seawater: Implications regarding surface complexation and color banding in ferrihydrite deposits. *American Mineralogist* **2001** 86, 834.

Rea, B. A.; Davis, J. A.; Waychunas, G. A. Studies of the reactivity of the ferrihydrite surface by iron isotopic exchange and Mössbauer spectroscopy. *Clays and Clay Minerals* **1994** 42 (1), 23.

Rietveld, H. M. A profile refinement method for nuclear and magnetic structures. *Journal of Applied Crystallography* **1969** 2, 65.

Rustad, J. R.; Felmy, A. R. The influence of edge sites on the development of surface charge on goethite nanoparticles: A molecular dynamics investigation. *Geochimica et Cosmochimica Acta* **2005** 69 (6), 1405.

Schwertmann, U.; Murad, E. Effect of pH on the formation of goethite and hematite from ferrihydrite. *Clays and Clay Minerals* **1983** 31 (4), 277.

Scott, D. T.; McKnight, D. M.; Blunt-Harris, E. L.; Kolesar, S. E.; Lovley, D. R. Quinone moieties act as electron acceptors in the reduction of humic substances by humics-reducing microorganisms. *Environmental Science and Technology* **1998** 32, 2984.

Shen, P.; Lee, W. H. (111)-Specific coalescence twinning and martensitic transformation of tetragonal ZrO_2 condensates. *Nano Letters* **2001** 1, 707.

Sherman, D. M. Electronic structures of iron (III) and manganese(IV) (hyro)oxide minerals: Thermodynamics of photochemical reductive dissolution in aquatic environments. *Geochimica et Cosmochimica Acta* **2005** 69 (13), 3249.

Sherman, D. M.; Randall, S. R. Surface complexation of arsenic(V) to iron(III) (hydro)oxides: Structural mechanism from ab initio molecular geometries and EXAFS spectroscopy. *Geochimica et Cosmochimica Acta* **2003** 67 (22), 4223.

Smedley, P. L.; Kinniburgh, D. G. A review of the source, behavior and distribution of arsenic in natural waters. *Applied Geochemistry* **2002** 17, 517.

Sparks, D. L., *Environmental Soil Chemistry*. 2nd ed.; Academic Press: Amsterdam, 2003.

Stack, A. G.; Eggleston, C. M.; Engelhard, M. H. Reaction of hydroquinone with hematite I. Study of adsorption by electrochemical-scanning tunneling microscopy and X-ray photoelectron spectroscopy. *Journal of Colloid and Interface Science* **2004** 274, 433.

Stevens, J. G.; Khasanov, A. M.; White, M. S. G. Ferrihydrite Modification by Boron Doping. *Hyperfine Interactions* **2003** 151/152, 283.

Stipp, S. L. S.; Hansen, M.; Kiristensen, R.; Hochella, M. F., Jr.; Bennedsen, L.; Dideriksen, K.; Balic-Zunic, T.; Leonard, D.; Mathieu, H.-J. Behaviour of Fe-oxides relevant to contaminant uptake in the environment. *Chemical Geology* **2002** 190, 321.

Stokes, R. J.; Evans, D. F., *Fundamentals of Interfacial Engineering*. 1st ed.; CH Publishers: New York, NY, 1997.

Stookey, L. L. Ferrozine-A New Spectrophotometric Reagent for Iron. *Analytical Chemistry* **1970** 42 (7), 779.

Straub, K. L.; Benz, M.; Schink, B. Iron metabolsim in anoxic environments at near neutral pH. *FEMS Microbiology Ecology* **2001** 34, 181.

Stumm, W.; Morgan, J. J., *Aquatic Chemistry, Chemical Equilibria and Rates in Natural Waters*. 3rd ed.; John Wiley & Sons, Inc.: New York, 1996.

Tamara, M. L.; Butler, E. C. Effects of iron purity and groundwater characteristics on rates and products in the degradation of carbon tetrachloride by iron metal. *Environmental Science and Technology* **2004** 38, 1866.

Tang, Z.; Kotov, N. A.; Giersig, M. Spontaneous organization of single CdTe nanoparticles into luminescent nanowires. *Science* **2002** 297 (5579), 237.

Varanda, L. C.; Morales, M. P.; M. Jafelicci, J.; Serna, C. J. Monodispersed spindle-type goethite nanoparticles from Fe^{III} solutions. *Journal of Materials Chemistry* **2002** 12 (12), 3649.

Verwey, E. J.; Overbeek, J. T. G., *Theory of the stability of lyophobic colloids*. ed.; Elsevier: Amsterdam, 1948.

Villalobos, M.; Trotz, M. A.; Leckie, J. O. Variability in goethite surface site density: evidence from proton and carbonate sorption. *Journal of Colloid and Interface Science* **2003** 268, 273.

Waychunas, G. A. Crystal chemistry of oxides and hydroxides. *Reviews in Mineralogy* **1991** 25, 11.

Waychunas, G. A.; Brown, G. E.; Apted, M. J. X-ray K-edge absorption-spectra of Fe minerals and model compounds. 2. EXAFS. *Physics and Chemistry of Minerals* **1986** 13 (1), 31.

Waychunas, G. A.; Davis, J. A.; Fuller, C. C. Geometry of sorbed arsenate on ferrihydrite and crystalline FeOOH: Revaluation of EXAFS results and topological factors in prediction sorbate geometry and evidence for monodentate complexes. *Geochimica et Cosmochimica Acta* **1995** 59, 3655.

Waychunas, G. A.; Fuller, C. C.; Rea, B. A.; Davis, J. A. Wide angle X-ray scattering (WAXS) study of "two-line" ferrihydrite structure: Effect of arsenate sorption and counterion variation and comparison with EXAFS results. *Geochimica et Cosmochimica Acta* **1996** 60 (10), 1765.

Waychunas, G. A.; Kim, C. S.; Banfield, J. F. Nanoparticulate iron oxide minerals in soils and sediments: unique properties and contaminant scavenging mechanisms. *Journal of Nanoparticle Research* **2005** 7, 409.

Waychunas, G. A.; Rea, B. A.; Fuller, C. C.; Davis, J. A. Surface chemistry of ferrihydrite: Part 1. EXAFS studies of the geometry of coprecipitated and adsorbed arsenate. *Geochimica et Cosmochimica Acta* **1993** 57, 2251.

Webb, S. M. *Sam's Interface for XAS Analysis Package* 0.60.

Wieland, E.; Wehrli, B.; Stumm, W. The coordination chemistry of weathering: III. A generalization on the dissolution rates of minerals. *Geochimica et Cosmochimica Acta* **1988** 52, 1969.

Wilburn, D. R.; Bassett, W. A. Hydrostatic compression of iron and related compounds: an overview. *American Mineralogist* **1978** 63, 591.

Wyckoff, R. W. G., *Crystal Structures 1*. 2nd ed.; Interscience Publishers: New York, NY, 1963.

Xu, Y.; Zhang, W.-x. Subcolloidal Fe/Ag particles for reduction of chlorinated benzenes. *Industrial & Engineering Chemistry Research* **2000** 39 (7), 2238.

Yang, M. X.; Sarkar, S.; Bent, B. E. Degradation of multiply-chlorinated hydrocarbons on Cu(100). *Langmuir* **1997** 13, 229.

Zhang, H.; Banfield, J. F. Size dependence of the kinetic rate constant for phase transformation in TiO_2 nanoparticles. *Chemistry of Materials* **2005** 17 (13), 3421.

Zabinsky, S. I.; Rehr, J. J.; Ankudinov, A.; Albers, R. C.; Eller, M. J. Multiple-scattering calculations of X-ray-absoprtion spectra. *Physical Review B* **1995** 52 (4), 2995.

Zhang, W.-x. Nanoscale iron particles for environmental remediation: An overview. *Journal of Nanoparticle Research* **2003** 5, 323.

Zhang, Z.; Fenter, P.; Cheng, L.; Sturchio, N. C.; Bedzyk, M. J.; Predota, M.; Bandura, A.; Kubicki, J. D.; Lvov, S. N.; Cummings, P. T.; Chialvo, A. A.; Ridley, M. K.; Benezeth, P.; Anovitz, L.; Palmer, D. A.; Machesky, M. L.; Wesolowski, D. J. Ion adsorption at the rutile--water interface: Linking molecular and macroscopic properties. *Langmuir* **2004** 20, 4954.

Zhang, W.-x.; Wang, C.-B.; Lien, H.-L. Treatment of chlorinated organic contaminants with nanoscale bimetallic particles. *Catalysis Today* **1998** 40, 387.

Zhong, L.-S.; Hu, J.-S.; Liang, H.-P.; Cao, A.-M.; Song, W.-G.; Wan, L.-J. Self-assembled 3D flowerlike iron oxide nanostructures and their application in water treatment. *Advanced Materials* **2006** 18 (18), 2426.

Zinder, B.; Furrer, G.; Stumm, W. The coordination chemistry of weathering: II. Dissollution of Fe(III) oxides. *Geochimica et Cosmochimica Acta* **1986** 50, 1861.